Title

Smart Polymers Towards Next-Generation Water-Energy Nexus Technologies

Author

Alsaid, Yousif

Publication Date

2023

Peer reviewed|Thesis/dissertation

UNIVERSITY OF CALIFORNIA

Los Angeles

Smart Polymers Towards Next-Generation Water-Energy Nexus Technologies

A dissertation submitted in partial satisfaction of the requirements for the degree of Doctor of Philosophy in Materials Science and Engineering

by

Yousif Jafar Sadik Alsaid

2023

ABSTRACT OF THE DISSERTATION

Smart Polymers Towards Next-Generation
Water-Energy Nexus Technologies

by

Yousif Alsaid
Doctor of Philosophy in Materials Science and Engineering
University of California, Los Angeles, 2023
Professor Ximin He, Chair

With the rising demands in energy and water, it becomes especially important to investigate alternate paths to source these valuable resources which sustain modern human life. The current water and energy production ecosystems are coupled via the water-energy nexus, operated by a robust system of electric steam turbines and reverse osmosis seawater desalination plants. Unfortunately, the interconversion process between these resources is plagued by low efficiencies, necessitating the desire to decouple the two resource streams. Advanced tailorable porous polymers present a possible technological platform to source more reliable and energy-efficient supplies of electricity and water. Unfortunately, they are currently limited by the intrinsic material challenges of mechanical-diffusive property trade-offs and reduced optical energy harvesting efficiency at oblique illumination. To combat these material challenges, cononsolvency and artificial phototropism are investigated and leveraged to create devices that break conventional property limits.

In Chapter 1, the fundamentals of pore structure engineering are discussed, alongside the limits present in current material systems. In Chapter 2, cononsolvency is investigated as a method to control polymer morphology and decouple the diffusive properties from the mechanical strength of materials. In Chapter 3, insights from fundamental cononsolvency studies are applied to generate tough chemistry-impartial gel polymer electrolytes that can outperform commercial battery separators. In Chapter 4, the same pore structure engineering techniques are implemented towards building soft robots with complex spatiotemporal programmable motion. In Chapter 5, utilizing a temperature-responsive polymer hydrogel, a system is designed exhibiting artificial phototropism for maximizing the harvesting of incoming optical energy.

The dissertation of Yousif Alsaid is approved.

Yu Huang

Yuzhang Li

Carlos Morales-Guio

Laurent Pilon

Aaswath P. Raman

Ximin He, Committee Chair

University of California, Los Angeles

2023

To my beloved family, friends, and mentors

Thank you for your unconditional love, support, and guidance

"I learned very early the difference between knowing the name of something and knowing something."

- Richard Feynman

Table of Contents

List of Figures

Acknowledgements

I embarked on my graduate school journey in 2017 with a vague list of goals and ambitions; with a combination of luck, effort, and serendipity, I leave with more than I bargained for. In addition to leading several projects towards a new frontier to solve some of the world's most pressing energy and water problems, I had the privilege of honing my communications skills by teaching and mentoring hundreds of undergraduates who are today in my shoes several years ago. None of this would be possible without the support and mentorship of my family, colleagues, and friends.

I want to acknowledge my advisor Prof. Ximin He who took me into her laboratory and offered me the opportunity to challenge myself in various projects, with flexibility and patience. Being among the first cohort to join the lab and contribute to its growth provided an unmatched learning experience. I am also grateful to Professors Yu Huang, Yuzhang Li, Carlos Morales-Guio, Laurent Pilon, and Aaswath P. Raman for serving on my committee and providing invaluable feedback to guide my research. I would also like to extend my thanks to my mentors and collaborators Dr. Xiaoshi Qian, Dr. Shuwang Wu, Dr. Roozbeh Khodambashi, Yunkai Luo, Dr. Jin-Koo Kim, Dr. Grace Whang, Dr. Christopher Choi, Dr. Bowen Yao, and Dr. Cheolgyu Kim, without whom this dissertation would not have been possible.

I would also like to thank my fellow group members and dear friends for their academic and personal support throughout this journey including, but not limited to, Dr. Yusen Zhao, Dr. Dong Wu, Imri Frenkel, Yichen Yan, Sidi Duan, Yingjie Du, Abdullatif Jazzar, Dr. Mutia n Hua, Pengju Shi, Zixiao Liu, Wen Hong, Chi Chen, Sidi Duan, Ta-Wei Wang, Ping He, Chuanwei Zhang, Zishang Lin, Heng-Jui Chu, Yucheng Zhang, Dr. Chiao-Yueh Lo, Bozhen Zhang, Kareem

Youssef, and Em. I will deeply miss the time we spent working together and hope we can stay in touch in the years to come and maintain life-long connections.

Lastly, I would like to thank my family and loved ones for their unwavering support and patience throughout this tortuous journey. I would like to thank my parents Jafar Alsaid and Hilda Khairallah for their guidance and support. I would like to thank my sisters Hala and Mariam for our chats and helping me enjoy my time away from work. I also send my sincere thanks to my extended family and grandparents for laying the foundations for tomorrow's accomplishments and celebrations.

Chapter 2 is a modified version of the published work:

Alsaid, Y., Wu, S., Wu, D., Du, Y., Shi, L., Khodambashi, R., Rico, R., Hua, M., Yan, Y., Zhao, Y., Aukes, D., & He, X. (2021). Tunable Sponge-Like Hierarchically Porous Hydrogels with Simultaneously Enhanced Diffusivity and Mechanical Properties. *Advanced Materials*, *33*(20), 2008235.

Chapter 3 is a modified version of the in-preparation work:

Alsaid, Y., Luo, Y., Yan, Y., Lee, A., Jazzar, A., Kim, J-K., Duan, S., Whang, G., Choi, C., Li, Y., & He, X. Amphiphilic Porous Polymers Towards Tough, Highly Conductive, Chemistry-Impartial, Gel polymer Electrolytes for Multi-Chemistry Rechargeable Batteries.

Chapter 4 is a modified version of the published work:

Khodambashi, R., Alsaid, Y., Rico, R., Marvi, H., Peet, M. M., Fisher, R. E., Berman, S., He, X., & Aukes, D. M. (2021). Heterogeneous Hydrogel Structures with Spatiotemporal Reconfigurability using Addressable and Tunable Voxels. *Advanced Materials*, *33*(10), 2005906.

Chapter 5 is a modified version of the published work:

Qian, X., Zhao, Y., Alsaid, Y., Wang, X., Hua, M., Galy, T., Gopalakrishna, H., Yang, Y., Cui, J., Liu, N., Marszewski, M., Pilon, L., Jiang, H., & He, X. (2019). Artificial phototropism for omnidirectional tracking and harvesting of light. *Nature Nanotechnology 2019 14:11*, *14*(11), 1048–1055.

Vita

2015 B.S. in Chemical Engineering and Materials Science
University of California, Berkeley
High Honors

2017 – 2023 Graduate Student Researcher
Department of Materials Science and Engineering
University of California, Los Angeles

Publications

Journals

26. Yan, Y., Duan, S., Liu, B., Wu, S., **Alsaid, Y.**, Yao, B., Nandi, S., Du, Y., Wang, T. W., Li, Y., & He, X. (2023). Tough Hydrogel Electrolytes for Anti-Freezing Zinc-Ion Batteries. *Advanced Materials*, *35*(18), 2211673.
25. Zhao, Y., Li, Q., Liu, Z., **Alsaid, Y.**, Shi, P., Jawed, M. K., & He, X. (2023). Sunlight-powered self-excited oscillators for sustainable autonomous soft robotics. *Science Robotics*, *8*(77).
24. Schulze, J. A., Kowalik, M., Hua, M., Wu, S., **Alsaid, Y.**, He, X., & van Duin, A. C. T. (2022). Investigation of Mechanical Properties in PVA Hydrogels Due to Cation Interactions Described by Reactive Forcefield Based Molecular Dynamics Simulations. *JOM*, *74*(12), 4632–4639.
23. Wu, S., Wang, T. W., Du, Y., Yao, B., Duan, S., Yan, Y., Hua, M., **Alsaid, Y.**, Zhu, X., & He, X. (2022). Tough, anti-freezing and conductive ionic hydrogels. *NPG Asia Materials 2022 14:1*, *14*(1), 1–8.
22. Yao, B., Wu, S., Wang, R., Yan, Y., Cardenas, A., Wu, D., **Alsaid, Y.**, Wu, W., Zhu, X., He, X., Yao, B., Wu, S., Wang, R., Yan, Y., Cardenas, A., Wu, D., Alsaid, Y., He, X., Zhu, X., & Wu, W. (2022). Hydrogel Ionotronics with Ultra-Low Impedance and High Signal Fidelity across Broad Frequency and Temperature Ranges. *Advanced Functional Materials*, *32*(10), 2109506.
21. Zhao, K., Cao, X., **Alsaid, Y.**, Cheng, J., Wang, Y., Zhao, Y., He, X., Zhang, S., & Niu, W. (2021). Interactively mechanochromic electronic textile sensor with rapid and durable electrical/optical response for visualized stretchable electronics. *Chemical Engineering Journal*, *426*, 130870.
20. Liu, H., Zhang, Y., Ma, S., **Alsaid, Y.**, Pei, X., Cai, M., He, X., & Zhou, F. (2021). Esophagus-Inspired Actuator for Solid Transportation via the Synergy of Lubrication and Contractile Deformation. *Advanced Science*, *8*(24), 2102800.
19. Lo, C. Y., Zhao, Y., Kim, C., **Alsaid, Y.**, Khodambashi, R., Peet, M., Fisher, R., Marvi, H., Berman, S., Aukes, D., & He, X. (2021). Highly stretchable self-sensing actuator based on conductive photothermally-responsive hydrogel. *Materials Today*, *50*, 35–43.
18. Yan, Y., Zhao, Y., **Alsaid, Y.**, Yao, B., Zhang, Y., Wu, S., & He, X. (2021). Artificial Phototropic Systems for Enhanced Light Harvesting Based on a Liquid Crystal Elastomer. *Advanced Intelligent Systems*, *3*(10), 2000234.
17. Zhang, Y., Zhao, Y., Peng, Z., Yao, B., **Alsaid, Y.**, Hua, M., Wu, D., Qiu, Y., Pei, Q., Zhu, X., He, Z., & He, X. (2021). Ultrastretchable Polyaniline-Based Conductive Organogel with High Strain Sensitivity. *ACS Materials Letters*, *3*(10), 1477–1483.
16. Frenkel, I., Hua, M., **Alsaid, Y.**, & He, X. (2021). Self-Reporting Hydrogel Sensors Based on Surface Instability-Induced Optical Scattering. *Advanced Photonics Research*, *2*(8), 2100058.
15. Zhang, H., Zhao, G., Wu, S., **Alsaid, Y.**, Zhao, W., Yan, X., Liu, L., Zou, G., Lv, J., He, X., He, Z., & Wang, J. (2021). Solar anti-icing surface with enhanced condensate self-removing at extreme environmental conditions. *Proceedings of the National Academy of Sciences of the United States of America*, *118*(18), e2100978118.
14. **Alsaid, Y.**, Wu, S., Wu, D., Du, Y., Shi, L., Khodambashi, R., Rico, R., Hua, M., Yan, Y., Zhao, Y., Aukes, D., & He, X. (2021). Tunable Sponge-Like Hierarchically Porous Hydrogels with

Simultaneously Enhanced Diffusivity and Mechanical Properties. *Advanced Materials*, *33*(20), 2008235.

13. Xue, Y., Xia, Y., Yang, S., **Alsaid, Y.**, Fong, K. Y., Wang, Y., & Zhang, X. (2021). Atomic-scale ion transistor with ultrahigh diffusivity. *Science*, *372*(6541), 501–503.
12. Zhao, Y., Lo, C. Y., Ruan, L., Pi, C. H., Kim, C., **Alsaid, Y.**, Frenkel, I., Rico, R., Tsao, T. C., & He, X. (2021). Somatosensory actuator based on stretchable conductive photothermally responsive hydrogel. *Science Robotics*, *6*(53), 5483.
11. Wu, S., **Alsaid, Y.**, Yao, B., Yan, Y., Zhao, Y., Hua, M., Wu, D., Zhu, X., & He, X. (2021). Rapid and scalable fabrication of ultra-stretchable, anti-freezing conductive gels by cononsolvency effect. *EcoMat*, *3*(2), e12085.
10. Wu, S., Hua, M., **Alsaid, Y.**, Du, Y., Ma, Y., Zhao, Y., Lo, C.-Y., Wang, C., Wu, D., Yao, B., Strzalka, J., Zhou, H., Zhu, X., He, X., Wu, S., Hua, M., Alsaid, Y., Du, Y., Ma, Y., … Zhou, H. (2021). Poly(vinyl alcohol) Hydrogels with Broad-Range Tunable Mechanical Properties via the Hofmeister Effect. *Advanced Materials*, *33*(11), 2007829.
9. Khodambashi, R. *, **Alsaid, Y.** *, Rico, R., Marvi, H., Peet, M. M., Fisher, R. E., Berman, S., He, X., & Aukes, D. M. (2021). Heterogeneous Hydrogel Structures with Spatiotemporal Reconfigurability using Addressable and Tunable Voxels. *Advanced Materials*, *33*(10), 2005906.
8. Lo, C. Y., Zhao, Y., Ma, Y., Wu, S., **Alsaid, Y.**, Peet, M. M., Fisher, R. E., Marvi, H., Aukes, D. M., Berman, S., & He, X. (2020). Bioinspired sensors and actuators based on stimuli-responsive hydrogels for underwater soft robotics. *Bioinspired Sensing, Actuation, and Control in Underwater Soft Robotic Systems*, 99–115.
7. Hua, M., Wu, D., Wu, S., Ma, Y., **Alsaid, Y.**, & He, X. (2021). 4D Printable Tough and Thermoresponsive Hydrogels. *ACS Applied Materials and Interfaces*, *13*(11), 12689–12697.
6. Zhao, Y., Zhang, B., Yao, B., Qiu, Y., Peng, Z., Zhang, Y., **Alsaid, Y.**, Frenkel, I., Youssef, K., Pei, Q., & He, X. (2020). Hierarchically Structured Stretchable Conductive Hydrogels for High-Performance Wearable Strain Sensors and Supercapacitors. *Matter*, *3*(4), 1196–1210.
5. Wu, S., Du, Y., **Alsaid, Y.**, Wu, D., Hua, M., Yan, Y., Yao, B., Ma, Y., Zhu, X., & He, X. (2020). Superhydrophobic photothermal icephobic surfaces based on candle soot. *Proceedings of the National Academy of Sciences of the United States of America*, *117*(21), 11240–11246.
4. Zhao, Y., **Alsaid, Y.**, Yao, B., Zhang, Y., Zhang, B., Bhuskute, N., Wu, S., He, X., Zhao, Y., Alsaid, Y., Yao, B., Zhang, Y., Zhang, B., Bhuskute, N., Wu, S., & He, X. (2020). Wood-Inspired Morphologically Tunable Aligned Hydrogel for High-Performance Flexible All-Solid-State Supercapacitors. *Advanced Functional Materials*, *30*(10), 1909133.
3. Qian, X. *, Zhao, Y. *, **Alsaid, Y.** *, Wang, X., Hua, M., Galy, T., Gopalakrishna, H., Yang, Y., Cui, J., Liu, N., Marszewski, M., Pilon, L., Jiang, H., & He, X. (2019). Artificial phototropism for omnidirectional tracking and harvesting of light. *Nature Nanotechnology 2019 14:11*, *14*(11), 1048–1055.
2. Zhao, Y., Xuan, C., Qian, X., **Alsaid, Y.**, Hua, M., Jin, L., & He, X. (2019). Soft phototactic swimmer based on self-sustained hydrogel oscillator. *Science Robotics*, *4*(33).
1. Wang, Y., Xiao, J., Zhu, H., Li, Y., **Alsaid, Y.**, Fong, K. Y., Zhou, Y., Wang, S., Shi, W., Wang, Y., Zettl, A., Reed, E. J., & Zhang, X. (2017). Structural phase transition in monolayer MoTe2 driven by electrostatic doping. *Nature 2017*, *550*(7677), 487–491.

* co-first author

Reviews

Zhao, Y., Hua, M., Yan, Y., Wu, S., **Alsaid, Y.**, & He, X. (2021). Stimuli-Responsive Polymers for Soft Robotics. Annual Review of Control, Robotics, and Autonomous Systems, 5.

Book Chapters

Lo, C., Zhao, Y., Ma, Y., Wu, S., **Alsaid, Y.**, Peet, M., Fisher, R., Marvi, H., Aukes, D., Berman, S., He, X., Bioinspired sensors and actuators based on stimuli-responsive hydrogels for underwater soft robotics. Chapter 5 in Bioinspired Sensing, Actuation, and Control in Underwater Soft Robotic Systems, D. A. Paley, N. M. Wereley (eds.), Springer Nature, 2020

Chapter 1: Introduction and Objectives

1.1 Water-Energy Nexus

As global energy demands continue to increase and the harmful effects of atmospheric carbon continue to be investigated, there presents an urgent need for accelerating the advancement of sustainable energy. Clean and sustainable sources such as solar and wind are limited by their intermittency, requiring an energy storage mechanism to utilize them during off-peak hours. Great efforts continue to be invested into new battery technologies to enable the supplementation, and hopefully the eventual replacement, of our current fossil fuels-dominated energy economy. Such energy storage solutions can play a key role in advancing electric vehicles, grid-scale energy storage, medical devices, wearable electronics, and soft robotics.

These rising energy demands are also coupled with increasing water demands. It is estimated that about 4 billion people, composing 66% of today's global population, live in severe water scarcity for at least one month per year, and this number is expected to rise in coming years.[1] With regards to modern day energy and water production, they are interrelated in what is known as the water-energy nexus (Figure 1.1); the processes for which they are generated at an industrial level for human consumption are interrelated. For the production of grid-scale electricity, electric steam turbines are used which source input water, vaporize it, and mechanical rotate turbine blades to generate an electric current; this process at an industrial scale is roughly 45% energy efficient.[2] In parallel, as the demand for potable drinking water rises, many areas with access to the ocean have adopted reverse osmosis desalination technologies using nearby seawater; this process is

roughly 59% energy efficient, as an energy input is required to force the seawater against its preferred salt concentration gradient, through large scale sieves.[3]

Figure 1.1 Schematic diagram of how modern-day water and energy production streams are interrelated, and the corresponding energy efficiencies of each inter-conversion.

1.2 Porous Polymers

With the onset of exponentially rising energy and water demands, there presents an urgent need to turn to new technological advances to generate novel materials towards decoupling these water and energy production ecosystems, and source a more reliable and energy-efficient supply with fewer water-energy interconversion. Among the various classes of materials posed to address these critical energy and water challenges, porous polymers offer a promising outlook.

Porous polymers have gained immense attention due to their light weight, diversity of synthetic routes, and ease of functionalization and processability into monolithic and thin-film structures. Tuning the structure and properties of porous polymers have yielded significant

contributions in gas storage,[4] separations,[5] drug release,[6] catalysis,[7] sensing,[8] carbon templating,[9] cell scaffolds,[10] and energy storage materials.[11,12]

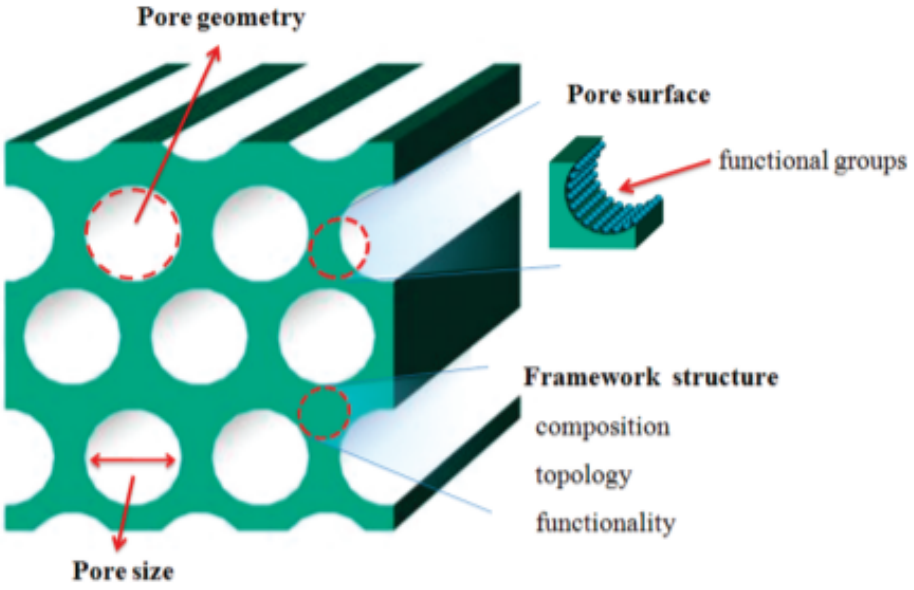

Figure 1.2 Schematic representing the versatile tunability of porous polymers.[13]

Owing to their ease of processability and inexpensive raw materials, polymer structures can be tailorable to a diverse range of target applications. The porosity and pore structure of these materials determine many of the macroscopic properties of the system such as strength, fracture resistance, surface area, and diffusion rates. Porosity is defined as the volume fraction of voids in the porous system. For certain classes of porous polymers, like aerogels that have their voids filled with air, porosity can be measured via gas pycnometry or mercury intrusion porosimetry. Hydrogels, a class of porous polymers where the voids are filled with water instead of air, offer a more convenient way to measure porosity, by directly measuring the wet and dry hydrogel masses, as shown in Equation 1. Regardless of how it is measured or calculated, the porosity offers a valuable metric for predicting, assessing, and tuning various macroscopic properties.

$$\phi = \frac{V_{void}}{V_{Total}} = \frac{\rho_{water} m_{water}}{\rho_{hydrogel} m_{hydrogel}} \approx 1 - \frac{m_{polymer}}{m_{hydrogel}}$$

Equation 1

In addition to the porosity, which captures the volume fraction of voids in the system, the geometry and distribution of those voids also bears significant impact on the macroscopic properties of these porous networks. The property of tortuosity aims to describe this pore geometry information that cannot be fully captured by porosity alone. Tortuosity is a quantitative measurement for how difficult or "tortuous" it is for a diffuse molecule to travel through the porous structure from one point to another. It is mathematically described as the ratio of the actual path length traveled over the shortest pathlength between two points, squared, illustrated in Figure 1.3 and Equation 2, where L is the distance traveled and L_0 is the shortest straight line path length.

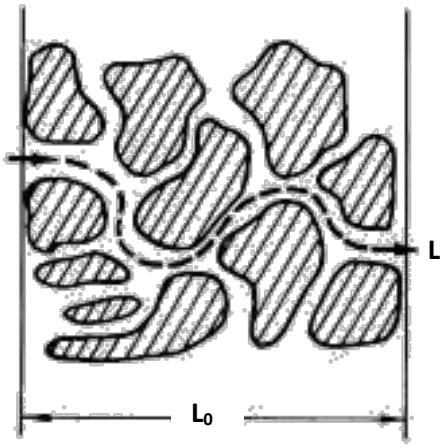

Figure 1.3 Schematic depicting the concept of tortuosity visually; path length through porous materials is usually longer than a direct straight line through the material. Mathematically, the tortuosity is defined to be the actual path length of a diffuse molecule divided by the shortest straight line path length, squared.

$$\boldsymbol{\tau = \left(\frac{L}{L_0}\right)^2 = \frac{< x_0^2 >}{< x^2 >}}$$

Equation 2

This squared ratio is equivalent to the ratio between $<x_0^2>$ and $<x^2>$, the mean-square displacement of a diffusive particle in nonporous and porous media, respectively. Einstein's Equation for the mean-square displacement via Brownian motion is described by Equation 3, where D is the diffusion coefficient and t is the elapsed time.

$$< \mathbf{x^2} > = \mathbf{2Dt}$$

Equation 3

Combining Equation 2 and Equation 3 yields Equation 4, which expresses tortuosity in terms of D_0 and D_{eff}, the small molecule diffusion coefficient in nonporous and porous media, respectively.

$$\boldsymbol{\tau} = \frac{\mathbf{D_0}}{\mathbf{D_{eff}}}$$

Equation 4

Tortuosity-porosity empirical relationships exist for a variety of porous systems; Equation 5 has been shown by Koponen et al. to be valid for porosities above 0.5.[14]

$$\boldsymbol{\tau = 1 + p(1 - \phi)}$$

Equation 5

Combining Equation 4 and Equation 5 yields Equation 6, which relates the effective diffusion coefficient of small molecules in porous structures to the nonporous self-diffusion coefficient D_0, porosity φ, and a pore structure factor p.

$$\mathbf{D_{eff}} = \frac{\mathbf{D_0}}{\mathbf{1 + p(1 - \phi)}}$$

Equation 6

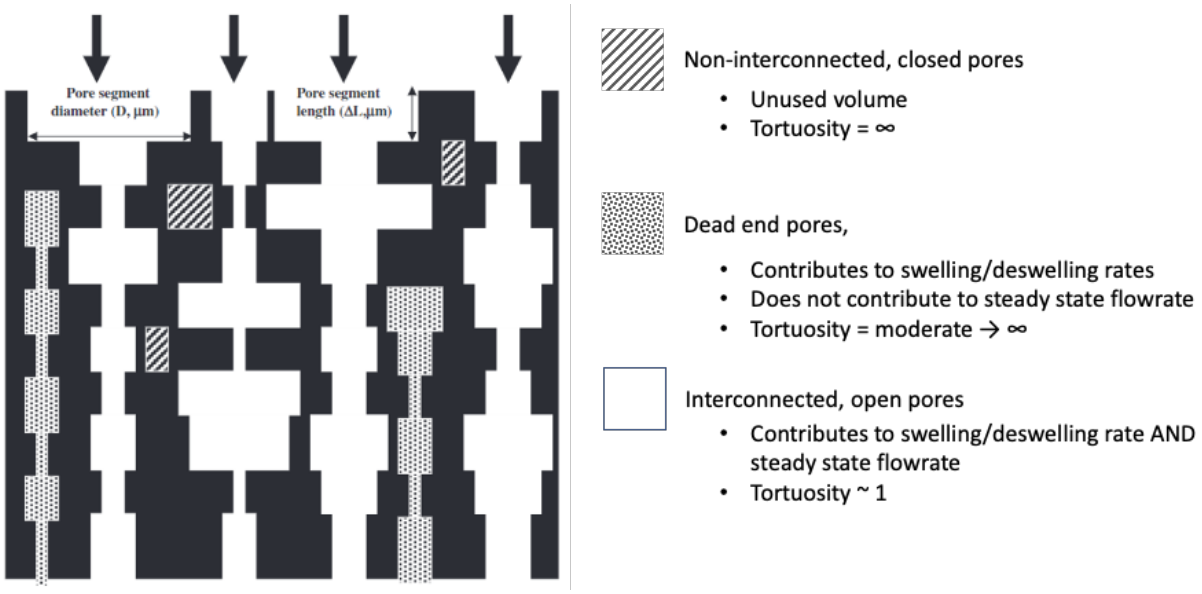

Figure 1.4 Schematic representing different types of pores and their individual descriptions.

Fickian self-diffusion of small molecules, typically described by Equation 7, gets modified to Equation 8 for in porous media. It is usually challenging to measure D_{eff} directly, and there may be deviations from the modeled behavior in Equation 6: pores in real materials can be divided into non-interconnected closed pores, dead end pores, and interconnected open pores (Figure 1.4) which can further complicate diffusion modeling. These equations provide a variety of ways to inter-convert between tortuosity, porosity, and diffusion coefficient allowing for a broad implementation of pore structure characterization techniques. In my experience, I have found that the easiest method to approximate Deff involves utilizing a technique like mercury intrusion

porosimetry and then converting the pore distribution data to a tortuosity from semi-empirical relations. With the tortuosity and the small molecule self-diffusion coefficient D_0, obtained either through diffusion NMR or through literature, an approximation can be calculated for D_{eff} by using Equation 4.

$$\mathbf{J_z = -D_0 \frac{dC}{dz}}$$

Equation 7

$$\mathbf{J_z = -D_{eff} \frac{dC}{dz}}$$

Equation 8

1.3 Hydrogels and Stimuli-Responsive Materials

A hydrogel is a three-dimensional cross-linked polymer network composed of one or more different monomer species along the backbone. Hydrogels get their name from their typically hydrophilic functional groups along their backbone, which allow the cross-linked polymer matrix to swell with water. Due to the 3D cross-linked network and hydrophilicity, a hydrogel is typically over 90% water by volume, and can be tuned by controlling the cross-linking density.[15]

This class of materials has gained significant attention in recent years due to its mechanical properties and chemical composition that resembles biological tissues. Many engineered hydrogels have been demonstrated to have Young's moduli comparable to that of skin and muscle tissue[16,17],

and the biologically similar high water content make them excellent candidates for biological integration. Figure 9 depicts the molecular structure of 3D cross-linked hydrogel demonstrating the high porosity which results in water swelling. In recent literature, the chemical and physical structure of these hydrogels have been tuned to achieve varying responsiveness to different environmental stimuli. Because of their biological compatibility and stimuli-responsive behavior, hydrogels carry immense potential to revolutionize the fields of soft robotics and targeted drug delivery.

Stimuli-responsive hydrogels are part of a larger class of materials called "smart materials", which are defined by their ability to respond and react autonomously to various external environmental stimuli. Examples of such stimuli are temperature, solvent, pH, ion concentration, light, electric field, and magnetic field among many others. The typical response of the material is in the form of volume change via swelling and de-swelling of the hydrogel matrix with water. The interactions between the molecular structure of the polymer matrix, as well as the chemical interactions of the backbone functional groups, are what govern the water-hydrogel interactions and the swelling-shrinking behavior. Measurement of Young's Modulus, swelling ratio, response rate, and critical input signal are all ways of characterizing the behavior of stimuli-responsive hydrogels.[18]

Crosslinked poly(n-isopropylacrylamide) (PNIPAM) demonstrates temperature-responsive behavior. This specific cross-linked hydrogel exhibits lower critical solution temperature (LCST) behavior; in other words, the polymer network is hydrophilic and swollen

below the LCST temperature, and hydrophobic and shrunken above it. Figure 1.5 depicts the LCST behavior of cross-linked PNIPAM. The LCST phenomenon is explained by an argument of free energy minimization: both enthalpy and entropy are temperature-dependent, however entropy scales faster with temperature. The entropy of the shrunken hydrophobic matrix has a larger temperature dependence than the swollen hydrophilic matrix due to the increased number of possible molecular configurations in the shrunken state. This means that ΔS for the shrunken state increases faster with temperature than ΔS for the swollen state. Hence, at higher temperatures, the shrunken conformation has lower free energy ΔG and is most thermodynamically favorable.

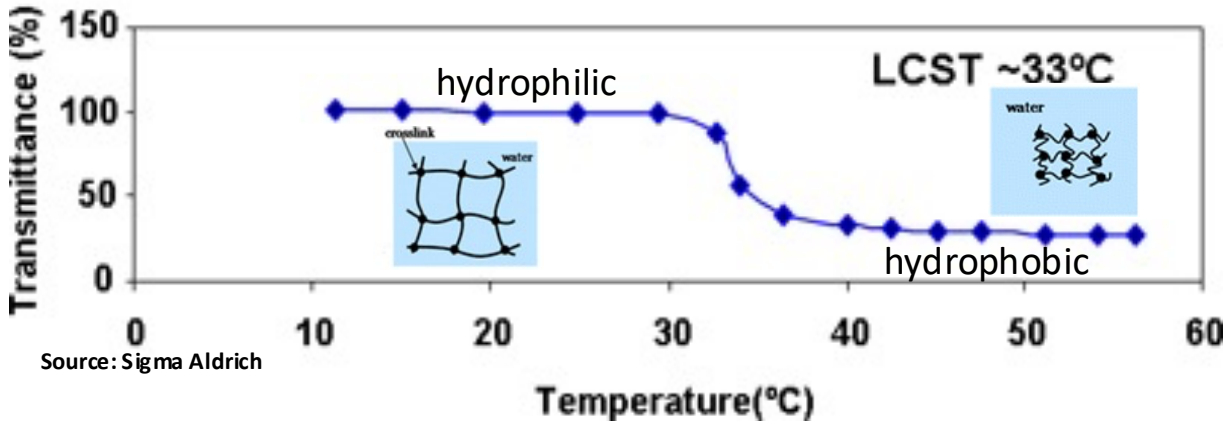

Figure 1.5 Temperature-responsive behavior of PNIPAM hydrogels, which experience a hydrophilic to hydrophobic phase transition above the lower critical solution temperature (LCST). Below the LCST, the polymer network swells completely with water, while above the LCST, it ejects most of the water from its pores and collapses.

1.4 Fundamental Materials Challenges

1.4.1 Mechanical-diffusive property trade-off

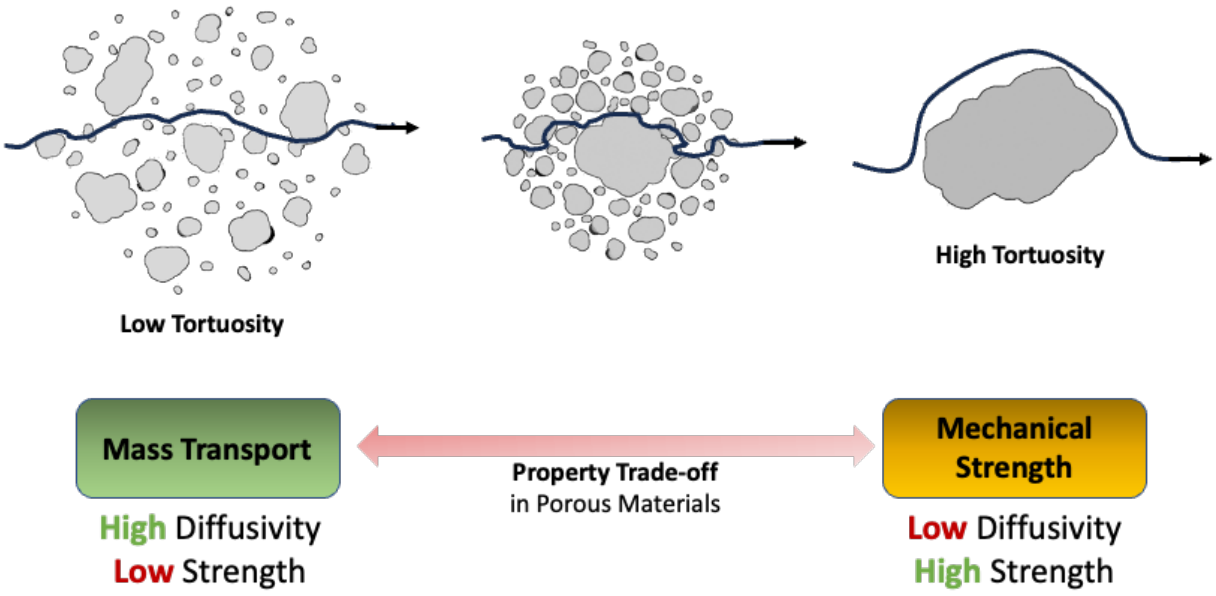

Figure 1.6 Schematic demonstrating the intrinsic trade-off between mass transport and mechanical strength in porous materials.

Most practical mass-transport applications involving porous materials are constrained by the notably slow diffusion through their pore structure. The mass transfer in porous materials is inversely proportional to the square of the material's smallest dimension, requiring device miniaturization.[19–21] To date, most works improving diffusion by increasing porosity.[22–31] This effectively reduces the tortuosity of the hydrogel and facilitates faster and greater transport through the polymer matrix. However, increasing porosity to increase effective diffusion coefficient typically results in a compromise in mechanical properties such as Young's modulus and toughness.[32–37]

Many state-of-the-art technologies rely on mass transfer at the liquid-solid interface (e.g., energy storage and catalysis) or solvent transport through pores (e.g., soft robotics and solar vapor generators). These *diffusion-limited* applications typically require decent *mechanical robustness* for long-term and large-scale viability.

To date, most works improve diffusivity in these porous materials by increasing *porosity*, which reduces the tortuosity and facilitates faster and greater transport, but unavoidably results in *compromised mechanical properties* (Young's modulus and toughness) (Figure 1.6).[22,23] Superporous hydrogels, which boast the highest porosities and swelling rates among hydrogels, have been fabricated using porosigen,[24–26] phase separation,[27,28] particle crosslinking,[29] and gas-blowing[30,31] techniques. The larger pore sizes effectively reduce the tortuosity of the hydrogel and facilitate faster and greater water transport through the polymer matrix. However, increasing φ to increase effective diffusion coefficient typically results in a compromise in mechanical properties such as Young's modulus and toughness.[32] Hydrogels with overly high porosities usually lack the necessary rigidity for practical applications**.**

Reconfiguring the overall pore structure, which tunes structure factor p, presents an alternative approach for increasing the effective diffusion coefficient in hydrogels. To date, this has been achieved via directionally aligned pore channels with built-in structural anisotropy.[33–36] Although limiting diffusion to fewer dimensions reduces the tortuosity, it also reduces the total volumetric flux through the hydrogel due to the confinement of transport: even with maximum diffusion coefficient, *i.e.*, $D_{eff} \sim D_0$, the overall swelling properties of the hydrogel are limited by the total flux of water in x, y, and z directions.[37] Larger volumetric flowrates are especially needed

for large-scale materials in industrial applications, rendering one- and two-dimensionally confined flux suboptimal.

Simultaneously improving the swelling and mechanical properties of porous materials has proven to be a daunting challenge. According to a review by Liu *et al.* to widen the application range of nanocomposite smart hydrogels, further improvement should be sought in terms of responsiveness, including responsive rate and degree, as well as mechanical properties, including Young's modulus, toughness, breaking strength, breaking strain, and so on".[19] Gemeinhart *et al.* reports "*methods for improving [mechanical properties] of porous hydrogels is of particular interest, but must be balanced with the ability to swell significantly and rapidly".*[38] In a systematic study, Bryant *et al.* report that increasing pore size and pore density decreases Young's modulus by half in polyhydroxyethylmethacrylate (pHEMA) hydrogels[39]. Predictive models from first principles also give the same expected result of porosity and modulus conflicting.[40] Despite tremendous efforts,[41–43] producing **gels with high mass transfer rates and high mechanical toughness** remains a long-standing fundamental bottleneck, calling for a *facile, scalable, and universal polymer preparation method* to address these property needs.

The ideal polymer structure that simultaneously maximizes diffusion and mechanical properties requires *dense pore walls* and *highly interconnected open-celled pores*. As shown in our previous works,[44,45] **cononsolvency provides one possible approach for generating such porous polymers with highly densified pore walls and highly interconnected pores to overcome the long-standing diffusion-mechanical property trade-off. However, establishing a technological platform for making and understanding the generality of such structures**

requires significant experimental effort to maximize the polymer aggregation behavior in mixed solvent systems. In contrast to single-solvent polymerization-induced phase-separation, which may also generate interconnected pores, mixed solvent phase separation grants additional tunability via variation of solvent ratios to better optimize the final morphology.

1.4.2 Oblique-incidence energy loss

One of the main limitations of solar energy harvesting is the oblique-incidence energy loss, or power density reduction at non-normal light incidence; in other words, for a horizontally oriented solar harvester the power density in the early sunrise and late sunset is drastically reduced, with the surface harvesting the most power at high noon when the sun is directly above the horizontal surface. Figure 6 demonstrates a physical schematic of angle-induced power density reduction. The sun has a spectral power density of 1000 W/m^2. This power density decreases when the light reaches surface of the Earth at non-normal incidence since that beam gets projected by an angle onto the surface. **Due to OEL, the solar power density impinging on a planar surface can drop by more than 50% at illumination angles above 60 degrees from the normal plane.**

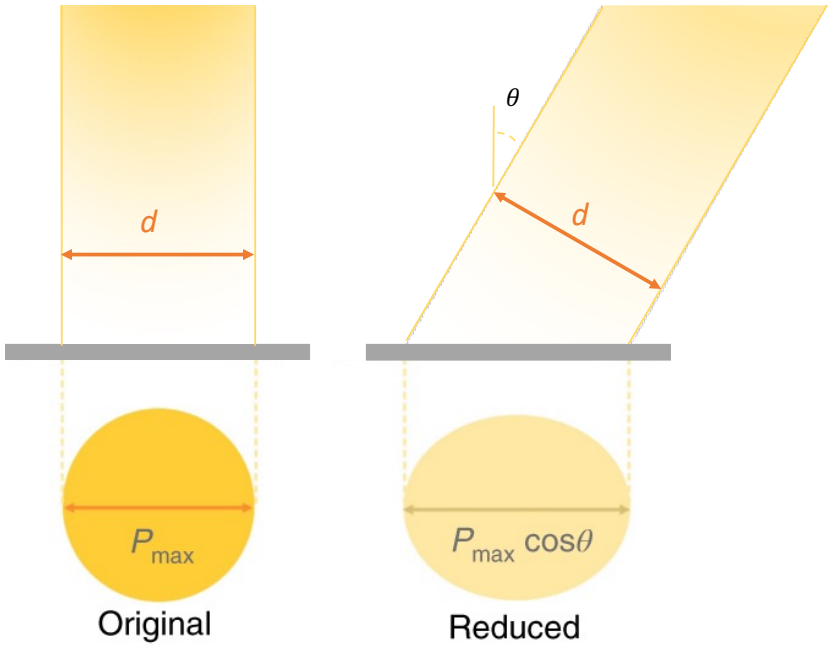

Figure 1.7 Schematic depicting the reduction in illumination power density reduction at oblique incident angles.

Chapter 2: Cononsolvency Towards Decoupling Diffusivity and Strength of Porous Materials

2.1 Background

2.1.1 Description of Cononsolvency and mechanism

Mixed solvent systems are ubiquitous in the field of chemistry and can be found across several applications: synthesis with phase separation,[46] chemical extraction of hydrophilic or hydrophobic compounds,[47] high performance liquid chromatography (HPLC),[48] recrystallization for purification,[49] drug biocompatibility,[50] and conductive polymer synthesis[51] all require the use of mixed solvents. Hence, a full understanding of solvent-cosolvent and polymer-solvent interactions is essential for many fundamental chemical processes. It is generally accepted that a mixture of two good solvents yields the same or improved solubility, ***cosolvency***. Despite this being the case in most systems, the scientific consensus is challenged by several anomalous cases where the opposite is observed: a mixture of two good solvents resulting in *decreased* solubility, ***cononsolvency*.**

Nearly a century ago, cellulose acetate was discovered to become less soluble in a mixture of aniline and acetic acid, which separately behave as high-solubility solvents for cellulose acetate; this phenomenon was observed in other systems later.[52–55] When a polymer can easily dissolve in solvent A and B separately, can it also dissolve in a mixture of the two? Not always. The literature refers to this anomalous phenomenon of reduced solute solubility in certain mixtures of two good solvents as 'cononsolvency' (Figure 2.1). Ample theoretical efforts have been invested towards

elucidating the mechanism, aiming to establish the general principle and solvent-cosolvent-polymer selection criteria (Figure 2.2).

Simulations have attempted to understand the interactions governing the behavior.[56–61] The literature roughly categorizes cononsolvency into two main physical descriptions: '*preferential adsorption'*, whereby one solvent interacts more strongly with the polymer chains than the other, resulting in the ejection of the weak solvent from the polymer matrix and in the collapse of the polymer chains,[60,62,63] and '*solvent complexation*', whereby the two solvents interact more strongly with each other than with the polymer chains, resulting in a solvent-cosolvent complex that behaves as a weak solvent for the polymer chains, thereby driving polymer chain collapse.[64] Most recently, Zhang *et al.* have claimed that *preferential adsorption* and *solvent complexation* dominate under different conditions (Figure 2.3).[65] Evidently, which of these two mechanisms is operative depends on the relative interactions of the solvents with the polymer and with each other.

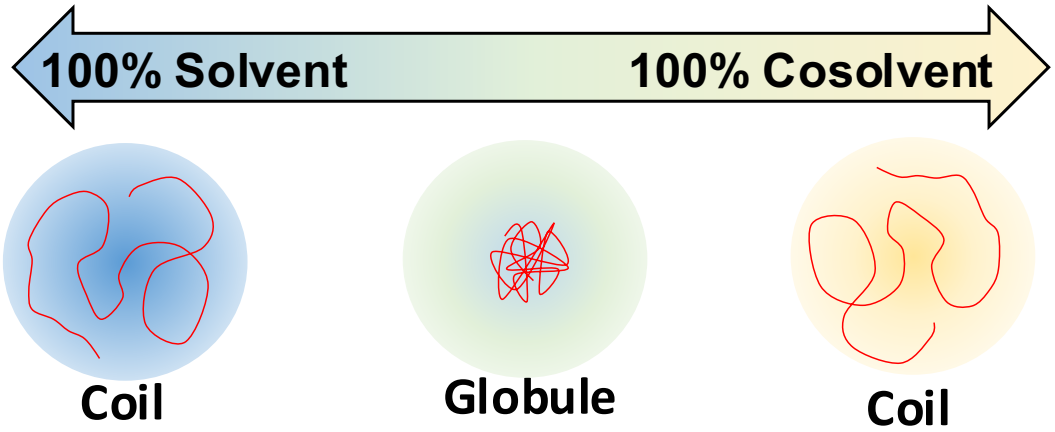

Figure 2.1 General concept of cononsolvency, the anomalous phenomenon of reduced solubility in mixtures of two good solvents.

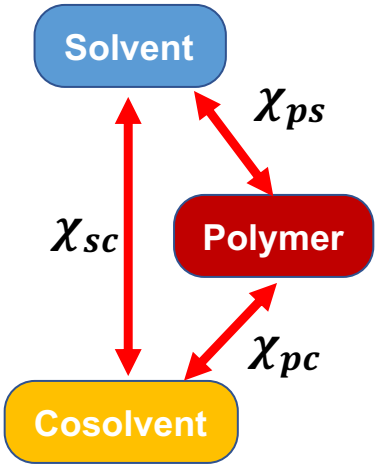

Figure 2.2 Schematic representing the three various Flory interaction parameters in a ternary system of a solvent, cosolvent, and polymer.

To grasp the mechanism that Zhang *et al.* propose, it is necessary to turn to the thermodynamic definition of interactions, specifically the Flory interaction parameters. In a binary mixture of components A and B, one can describe the Gibbs free energy of mixing to be the sum of the enthalpic and entropic mixing components; the free energy of mixing can also be expressed in terms of component mole fractions (x_i), volume fractions (φ_i), an interaction parameter (χ) which describes the interactions between A and B molecules (Equation 9). It can be noted that the volume fractions can be approximated to be equivalent to mole fractions if the molecules are of sufficiently similar sizes. This equation can be re-written in a clearer way to illustrate the enthalpic and entropic components (Equation 10) where it can be more clearly seen that the Flory interaction parameter between components A and B, χ_{AB}, lies within the enthalpic term, while the entropic

term exclusively encapsulates the free energy mixing of an ideal solution where A and B molecules are identical and do not experience any attractive or repulsive interactions.

An interaction parameter that is positive, zero, or negative corresponds to repulsive, ideal, and attractive interactions between A and B molecules, respectively. On a macroscopic solution level, positive and negative interaction parameters also correspond to endo thermic and exothermic processes, respectively, based on how they govern the enthalpic term in the free energy of mixing equation. It should be noted that while the fundamental framework provided by defining interaction parameters is useful for conceptually understanding the cononsolvency mechanism, the direct measurement of interaction parameter remains a non-trivial process. These parameters are known to exhibit concentration and temperature dependencies and it remains uncertain whether their measurement at specific conditions can be extrapolated to others.

$$\Delta G_{mix} = \Delta H_{mix} - T\Delta S_{mix} = RT[x_A \ln(\phi_A) + x_B \ln(\phi_B) + x_A \phi_B \boldsymbol{\chi_{AB}}]$$

Equation 9

$$\Delta G_{mix} = RT x_A \phi_B \boldsymbol{\chi_{AB}} - T\big[-R[x_A \ln(\phi_A) + x_B \ln(\phi_B)]\big]$$

Equation 10

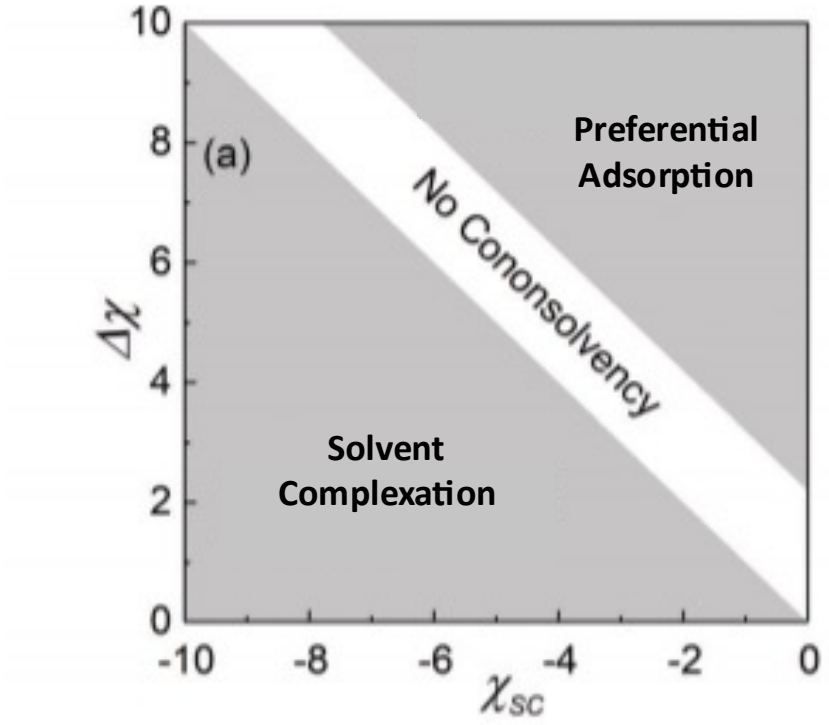

Figure 2.3 Diagram representing how the relative magnitudes of the various interaction parameters determine the type of cononsolvency, or lack thereof, which occurs. The $\Delta\chi$ term corresponds to the difference between the polymer-cosolvent and the polymer-solvent interaction parameters. The χ_{SC} term corresponds to the solvent-cosolvent interaction parameter.[65]

Obtaining a modern understanding of solute-solvent behaviors can help discover a new design principle for controlling polymer conformation, thus achieving desirable material microstructures and properties by simply selecting appropriate solvents and polymers. Such knowledge and abilities would benefit countless fields and applications.

2.1.2 Previous Approaches and Limitations

Experimentally, cononsolvency has been utilized to study the fundamental coil-globule-coil transition in PNIPAM linear chains[66,67] and microgels.[63,68] Studies involving cononsolvency in centimeter-scale bulk gels remain limited; they primarily focus on polymers synthesized in pure solvents with subsequent immersion in mixed solvents, rather than in-situ polymerization of the crosslinked network from monomer or polymer in the mixed solvent. Importantly, the latter would allow for more broadly tunable pore structures.[69] Moreover, current works experimentally investigating cononsolvency typically keep the binary solvent composition and polymer fixed. Tokuyama et al. showed that a 24-hr thermal-initiated polymerization of PNIPAM in DMF-water mixed solvent could produce structures with enhanced thermal-responsive deswelling rate;[70] however, the swelling rate, an equally important property, and mechanical characterizations were neglected. Most experimental works do not systematically study the effect of solvent composition and reaction temperature on cononsolvency-induced polymer aggregation.[68,71,72] Additionally, all these works employ 12-24 hr thermal-initiated reactions, incompatible with rapid manufacturing.

Most recently, Mukherji *et al.* attempted the commendable task of combining molecular simulations with complementary polymer synthesis, leveraging cononsolvency to create a design principle for multi-responsive copolymer architectures with flexible conformational tuning.[73,74] However, despite this milestone work with deep insights from simulation studies and evidence that cononsolvency may be a generic phenomenon,[60,65], experimental demonstration has remained limited to solutions of linear block copolymers rather than larger scale macrogels with clearly defined structure-property correlation.

Further advancements in porous polymer engineering may be facilitated via the following: i) *an experimentally-driven mechanistic understanding of the cononsolvency phenomenon for a broad range of polymers and solvents* to explain the anomalous behaviors of reduced solute solubility of polymers in specific mixtures of good solvents. This may provide a mechanistic foundation for ii) *a novel, general scalable and inexpensive method* to produce porous polymers with mutually enhanced mechanical and diffusive properties, the highly desired but often contradictory properties in porous materials. Such a mutual enhancement would be achieved by utilizing cononsolvency to simultaneously densify the polymer pore walls, via tuning the conformation of the individual polymer chains, while also reducing pore tortuosity, by creating interconnected channels via the phase separation. This will provide a potentially transformative new solution to the 'mechanical-diffusive trade-off' of broad porous materials.

2.2 Fundamental Mechanism Study

2.2.1 Hofmeister Series Analogy

The Hofmeister series represents a sequence of cations and ions that are ordered by their ability to induce kosmotropic (order-making, salting out) or chaotropic (disorder-making, salting in) phase change (Figure 2.4). This Hofmeister effect has been studied extensively in its ability to modulate and amplify the mechanical properties of polymeric systems via promotion of additional hydrogen bonding between the polymer chains in the saltin-out process (Figure 2.5, Figure 2.6, and Figure 2.7). Despite both the Hofmeister effect and cononsolvency being discovered nearly a century ago, no efforts have gone towards finding a solvent analog to the Hofmeister series: analogous to the Hofmeister series, there may exist a ranked series of mixed solvent aqueous solutions ordered by their ability to induce phase separation in polymer systems. Herein, we aim

to establish such a mixed solvent series, ordered by their propensity to induce polymer phase separation, by systematically collecting a library of polymer solution data. PNIPAM is primarily investigated owing to its well documented cononsolvency properties and widespread use as a stimuli-responsive material. With a lower critical solution temperature (LCST) of 31-34°C, closely matching the human body temperature, PNIPAM is a highly promising candidate hydrogel for biomedical applications.

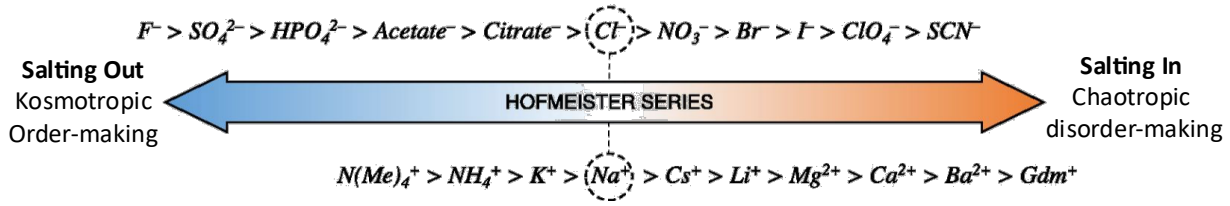

Figure 2.4 Hofmeister series of kosmotropic and chaotropic ions, which can induce polymer salting out or salting in, respectively.[75]

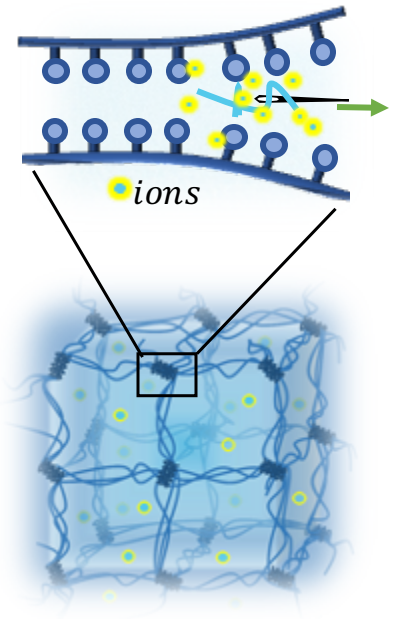

Figure 2.5 Kosmotropic ions inducing salting-out of a polymer network.

From investigating the role of the mixed solvent composition during synthesis on the final polymer conformation, we propose a ranked series of mixed solvents ordered by their strength in promoting poly(N-isopropylacrylamide) (PNIPAM) phase separation, analogous to the Hofmeister series of chaotropic (disorder-making) and kosmotropic (order-making) ions triggering salting-in and salting-out behaviors in surrounding polymers. To our knowledge this is the first report documenting that such a kosmotropic/chaotropic mixed solvent series exists; prior works utilizing mixed solvents to augment polymer structure either forego justifying their selection of cosolvent or neglect to elaborate on their selection of a specific composition.

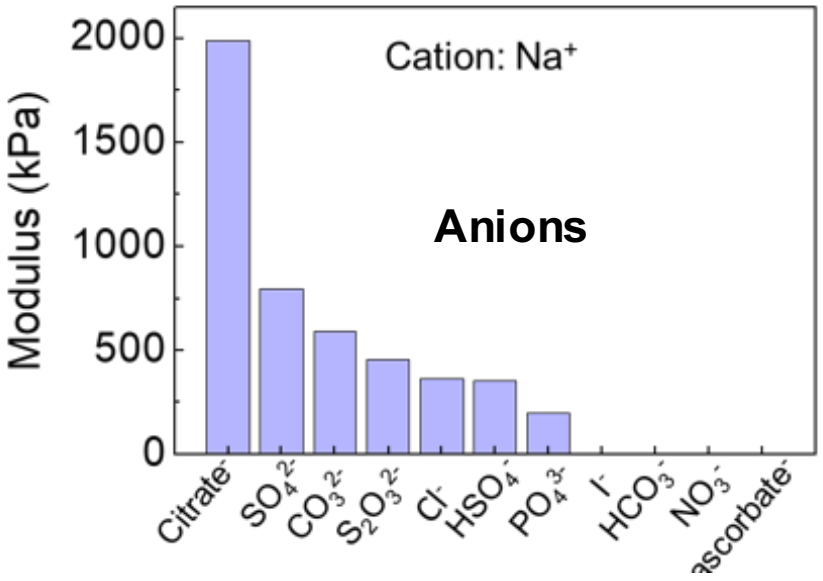

Figure 2.6 Ranking of various anions for the salting-out of PVA hydrogels, inducing mechanical improvement of the Young's modulus.

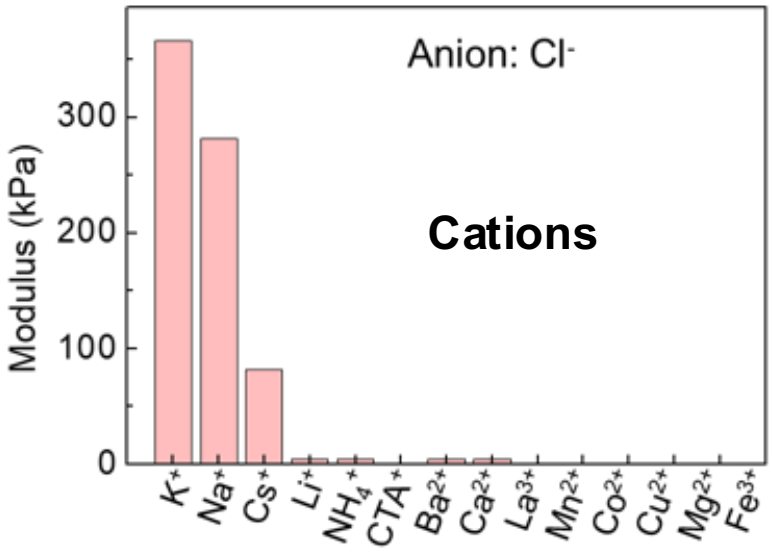

Figure 2.7 Ranking of the various cations for the salting-out of PVA hydrogels, inducing mechanical improvement of the Young's modulus.

2.2.2 Solvent Series Elucidation from Polymer Solutions

To build a platform for generating 3D crosslinked polymers with interconnected open porous structures exhibiting mutually enhanced diffusion and mechanical properties, we systematically studied the multi-scale factors governing the structure-property relations. On the molecular level, cononsolvency is governed by the interactions between the polymer, solvent, and cosolvent, which ultimately dictate the nanometer-scale linear polymer conformation and micron-scale polymer chain aggregation (Figure 2.8). By first building a fundamental understanding of the phase separation behavior in dilute systems with *linear* polymer chains, we could then extend this information to 3D *crosslinked* dense polymer networks, specifically tailoring synthesis conditions to achieve optimal cononsolvency-driven polymer densification and enhanced pore interconnectivity.

With a near-infinite selection of polymer systems, we choose PNIPAM as the exemplary polymer because of the widespread literature reporting its cononsolvency behavior in methanol, IPA, and DMSO. The nine cosolvents we selected represent some of the most accessible water-miscible solvents; for the purpose of clarity in this work, water will be referred to as the "solvent" while the other water-miscible solvents will be referred to as the "cosolvent". When referring to cosolvent mole fraction in a solvent-cosolvent mixture, x_c will be used. In addition, when communicating a specific cosolvent mole fraction, a shorthand notation will be used where the mole fraction value is represented in subscript after the *x*; for example $x_c = 0.4$ may be represented as $x_{0.4}$.

In our previous works, we demonstrated that highly kosmotropic ions in the Hofmeister Series can strengthen physically cross-linked polyvinyl alcohol (PVA) networks to record-high levels[76] while still maintaining high ionic conductivities to be used as resilient gel electrolytes in zinc-ion batteries:[77] this work suggests a similar series may exist for mixed solvents, expanding currently established methodologies for pore structure control of chemically cross-linked polymer networks.

To investigate PNIPAM's coil-to-globule transition in various mixed solvents, we select nine different water-miscible cosolvents (dimethyl sulfoxide (DMSO), methanol (MeOH), dioxane, tetrahydrofuran (THF), acetonitrile (ACN), isopropyl alcohol (IPA), dimethyl formamide (DMF), ethanol (EtOH), and acetone) to create nine binary solvent mixtures with varying molar compositions. 1 mg/mL linear PNIPAM chains were dissolved in these nine mixed solvents at varying solvent molar compositions, and optical transmittance measurement was conducted to determine the phase boundaries for the coil-to-globule polymer conformation transition: a

transparent solution corresponds to PNIPAM taking the extended coil phase which contains few light scattering centers, while a turbid white solution corresponds to PNIPAM taking the collapsed globule phase with many light scattering centers (Figure 2.8). The range of cosolvent molar compositions, x_c, in which the PNIPAM is in the globule phase can be used as a metric for how strongly the mixed solvent system promotes phase separation into polymer-rich (globule) and polymer-poor (liquid) phases.

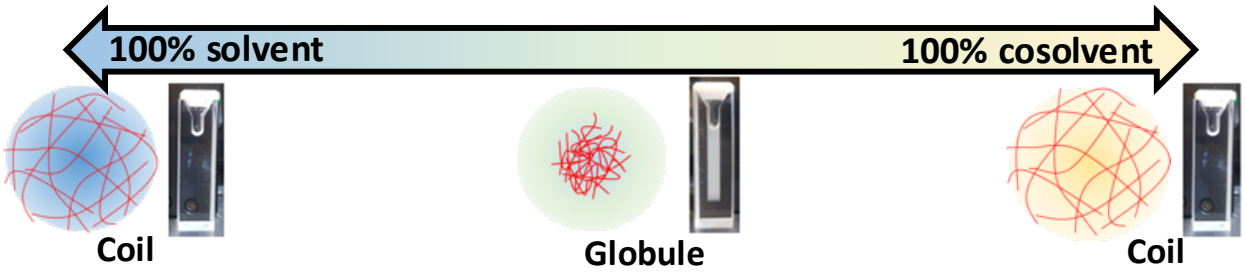

Figure 2.8 Transparency change of PNIPAM in specific solvent environments. In the presence of pure solvent or pure cosolvent, the PNIPAM chains adopt a coil conformation, resulting in transparent solutions. In the presence of a solvent-cosolvent mixture, the PNIPAM chains collapse into a globule conformation, resulting in opaque white solutions.

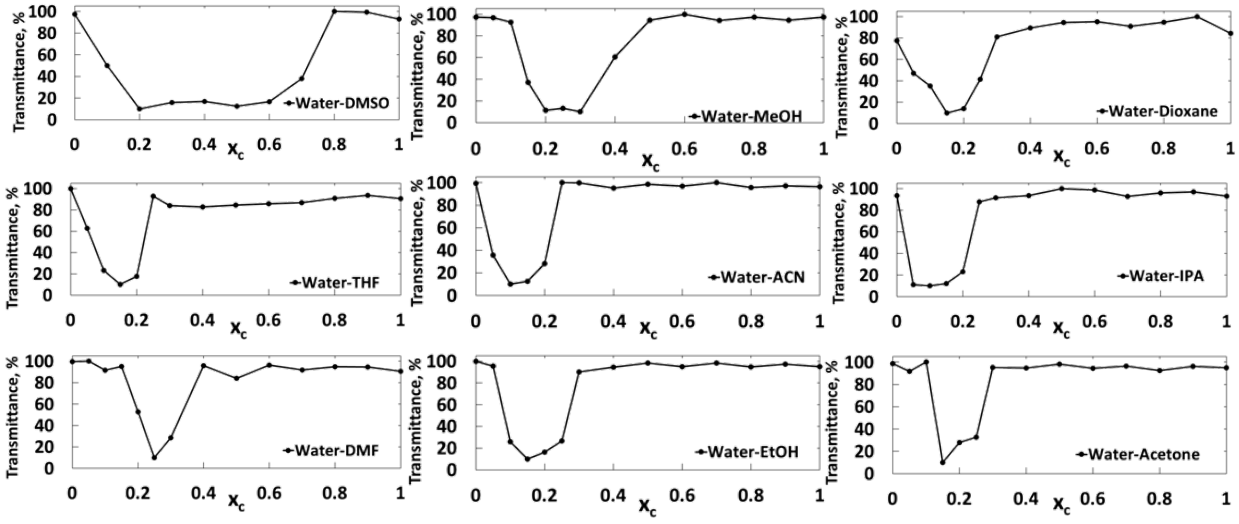

Figure 2.9 Normalized transmittance curves of 1 mg/mL 600 g/mol PNIPAM chains dissolved in various compositions of water-DMSO, water-MeOH, water-dioxane, water-THF, water-ACN, water-IPA, water-DMF, water-EtOH, water-acetone mixtures.

We observed that certain solvent mixtures promote kosmotropic polymer collapse more than others, reminiscent of the Hofmeister series where different ions can exhibit different strengths for salting-out behavior. Specifically, for dilute PNIPAM solution concentrations, DMSO-water promotes globule formation at the widest solvent compositions, followed by methanol-water (Figure 2.9). These cosolvents used alongside water can be ordered by their propensity to maintain the globule phase at wider compositions (Figure 2.10). We also observed that the cross-linked PNIPAM network morphologies exhibited a strong dependency on the solution phase behavior.

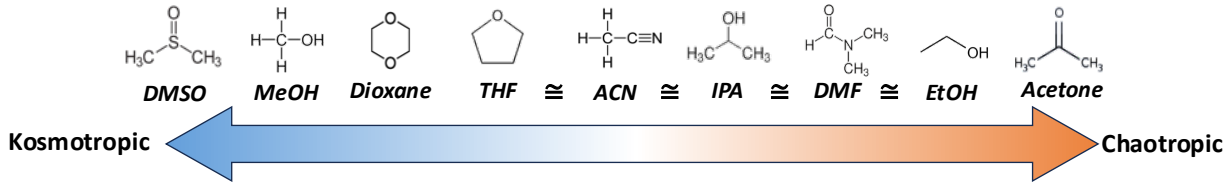

Figure 2.10 Ranked sequence of cosolvents, ordered by their ability to induce coil-globule phase change in PNIPAM aqueous solutions.

2.3 Pore Structure Control

2.3.1 Gel Network Behavior

We have developed a general, facile, and rapid cononsolvency photopolymerization technique for various materials, using PNIPAM in DMSO-water cononsolvent mixtures as an exemplary system, to synthesize hydrogels exhibiting two-fold enhancements in swelling ratio and Young's modulus, and a six-fold enhancement in deswelling rate compared to a hydrogel control synthesized with a conventional pure solvent method. This technique takes advantage of simultaneous crosslinking and cononsolvency-induced polymer collapse to generate hierarchically structured and interconnected polymer networks. We have systematically investigated the effects of solvent composition and reaction temperature on the microstructures, mechanical properties, and swelling-deswelling performance of the resulting hydrogels. By leveraging the structure-property insights, we developed 3D-printable PNIPAM hydrogels with broadly tunable swelling and mechanical properties and extended this principle to other polymer hydrogel systems.

PNIPAM hydrogels were synthesized via free-radical UV photopolymerization in different mixed solvent compositions. In pure solvent environments (Figure 2.11), the polymerization yields

regular closed-cell pores, termed closed pores, while in specific mixed solvent conditions (Figure 2.12), the pores exhibit hierarchical open-celled pores, termed open pores, with a high degree of interconnectivity caused by the simultaneous crosslinking and cononsolvency-induced collapse during photopolymerization. The pore structure and hydrogel properties can be tuned via careful selection of solvent composition and reaction temperature to achieve both enhanced swelling and mechanical performance. Figure 2.11 and Figure 2.12 depict photos and SEM micrographs of PNIPAM hydrogels photopolymerized in pure water and mixed DMSO-water solutions, respectively; it is readily observed that the hydrogels synthesized in the pure water were optically transparent, while the mixed solvent synthesized gel was white and opaque.

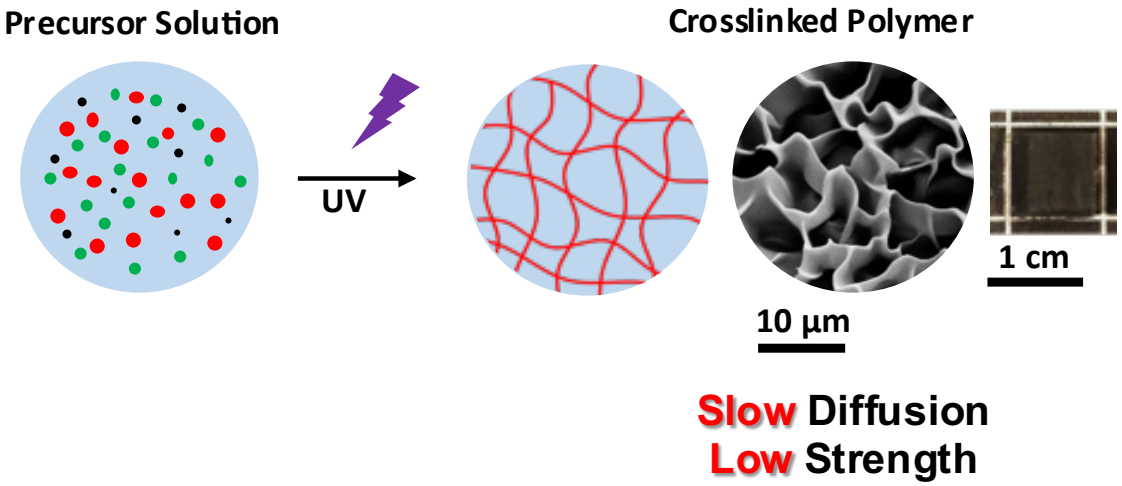

Figure 2.11 Generation of conventional closed-cell pore structure in PNIPAM hydrogel by conducting the UV photopolymerization of a precursor solution composed of a pure solvent.

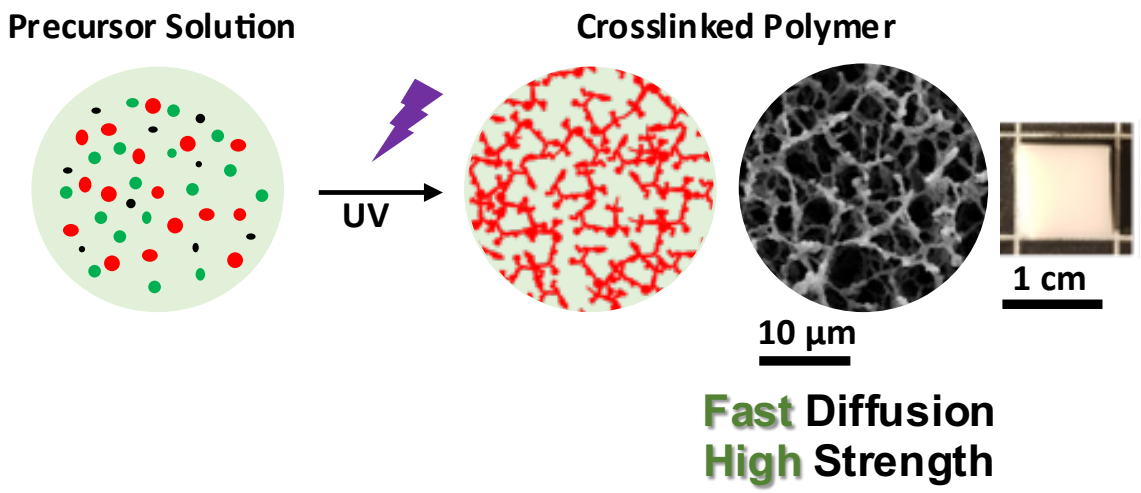

Figure 2.12 Generation of novel open-celled pore structure in PNIPAM hydrogel by conducting the UV photopolymerization of precursor solution composed of specifically tailored mixed solvent.

Building upon the results of the optical transmittance measurements, we prepared 20wt% precursor monomer solutions using all nine binary solvent mixtures by selecting the mixed solvent compositions that lie in the middle of their respective globule phase region; for example, for the DMSO-water system, we prepared monomer precursors with $x_{0.4}$ mole fraction; for methanol-water we selected $x_{0.25}$, and so forth. These mole fractions represent the solvent compositions whereby the PNIPAM preferentially adopts the globule phase, as evidenced by transmittance measurements. Upon illuminating with UV light, most of these precursor solutions were polymerized into translucent-white 3D cross-linked networks, consistent with the translucent-white appearance of their respective mixed-solvent polymer solutions (Figure 2.13 upper photographs). Despite these samples' equivalent thickness of 0.5mm, the gel polymerized in a DMSO-water mixture demonstrated the highest opacity. Upon examination of the microstructure

under SEM, post freeze-drying, it can be clearly observed that this specific recipe generated an open-cell spongey highly interconnected pore structure, whereas the others produced either the conventional closed-cell tortuous rounded pores or a variation of the closed-cell morphology with rough and textured pore walls (Figure 2.13 upper SEM images).

70wt% precursor solutions were also prepared to examine the monomer concentration dependency of the coil-globule phase behavior. At these higher precursor concentrations, only DMSO-water resulted in a turbid white gel after UV photopolymerization (Figure 2.13 lower photographs). Under SEM, only DMSO-water gel samples maintained the open-cell interconnected pore network emblematic of cononsolvency phase separation, while the remaining solvent mixtures yielded the generic closed-cell pore structure (Figure 2.13 lower SEM images). This suggests that the phase separation, or coil-to-globule phase change for PNIPAM chains, is suppressed at higher precursor concentrations. To support this claim, we created $x_{0.4}$ DMSO-water gels at even higher monomer concentrations, up to 80wt% where the generated gel reverted to the generic macroscopically-transparent closed-cell pore structure (Figure 2.14).

Macroporous morphology in hydrogels is controlled by a combination of (1) spinodal decomposition, (2) coarsening, and (3) polymerization and cross-linking. If coarsening occurs faster than polymerization and cross-linking, then the strong covalent bonds form in the coarsened state after spheroidization, resulting a closed-cell pore structure. In contrast, if polymerization and cross-linking occur faster than coarsening, it is possible to generate a bicontinuous matrix of polymer-rich and polymer-poor phases whereby coarsening is inhibited by the strong covalent bonds in the polymer-rich phase.[78] We hypothesize that cononsolvency results in accelerated

polymerization and cross-linking via agglomeration-induced local concentration fluctuations, which is what gives rise to the bicontinuous matrix macroscopically observed as an open-celled pore structure. Supporting this hypothesis, by measuring the percent reaction conversion, we experimentally observed that cononsolvent polymerization indeed results in faster reaction rates than pure solvent polymerization, despite using constant monomer concentrations, reaction temperatures, UV intensity, and curing time. The pure-solvent and cononsolvent polymerization environments hence result in cross-linked polymer structures with different optical, diffusional, and mechanical properties.

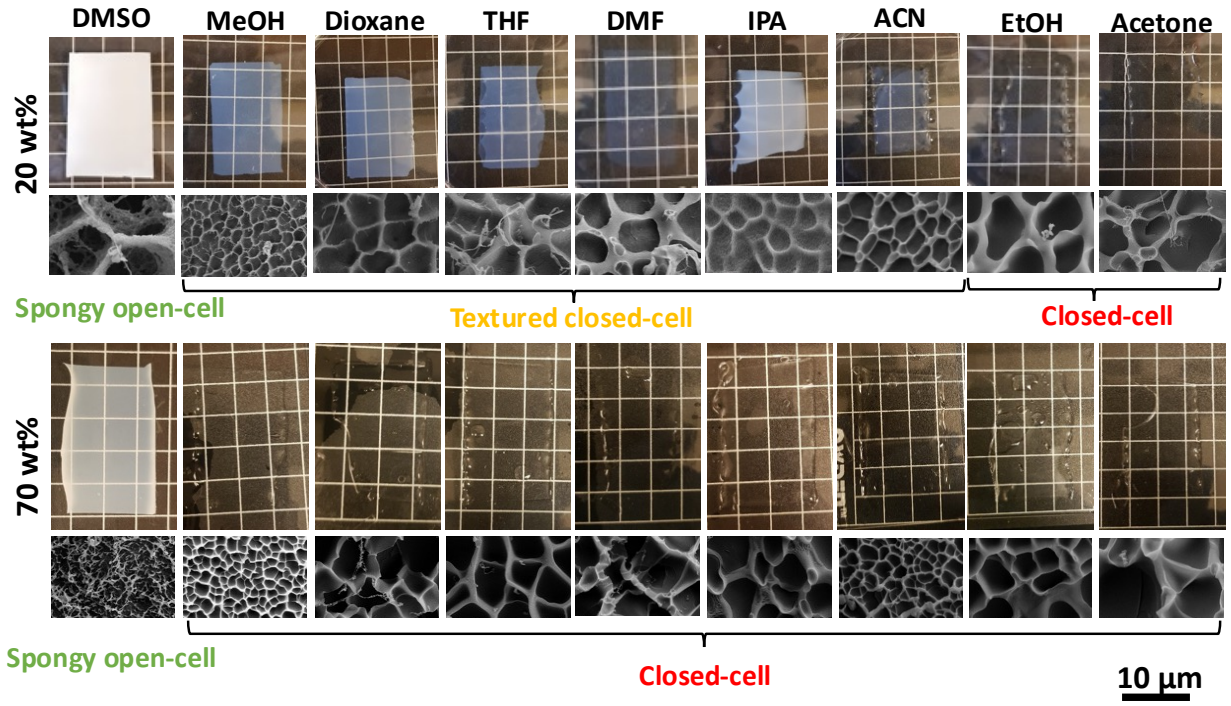

Figure 2.13 Macroscopic transparency and microscopic morphology of PNIPAM hydrogels synthesized in various mixed water-cosolvent precursor solutions with 20 wt% (top) and 70 wt% (bottom) monomer.

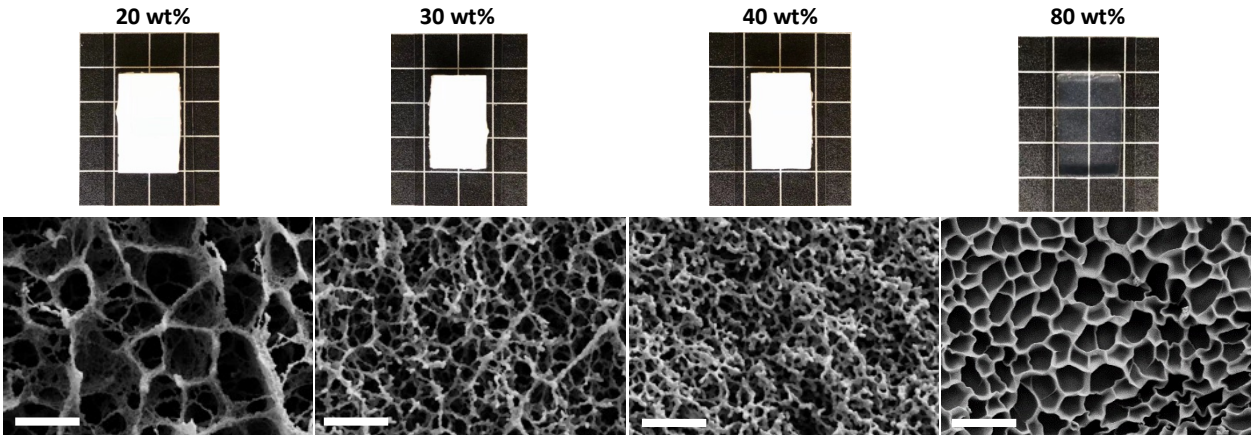

Figure 2.14 Suppression of open-celled pores, corresponding to closed-cell microstructural morphology and transparent macroscopic appearance, of PNIPAM hydrogels synthesized in a 40 mol% DMSO aqueous solution.

2.3.2 Unifying Solution and Network Behaviors

Reconciling polymer solution behavior with polymer network behavior can provide a roadmap towards custom tailoring pore morphology to specific desires applications. Polymer solutions exhibit reversible coil-to-globule transitions which can be observed in real time, unlike cross-linked polymer hydrogels where the coils or globules are fixed due to crosslinking. The polymer structures that can be generated with cononsolvency photopolymerization require specific solvent systems and reaction conditions; not all mixed solvent systems exhibit the cononsolvency phenomenon with the desired polymer backbone. In the case of linear PNIPAM chains, mixtures of water-DMSO,[79] water-methanol,[80,81] and water-ethanol[82] have been extensively studied. We focus on the water-DMSO system since we have shown it is the system with the most prominent

mixed-solvent-induced phase separation. PNIPAM chains exist in the coil state in pure water and pure DMSO solvents; they collapse into globules in DMSO-water mixtures.

The temperature-induced coil-to-globule transition can hence be tracked by observing the solution turbidity. At room temperature, the turbidities of PNIPAM solutions in 0 mol%, 40 mol%, and 100 mol% DMSO (Figure 2.15) correspond to the expected coil-globule-coil transition behavior described in Figure 2.8; namely the polymer solutions are optically transparent in pure water and DMSO solvents, where coils are expected, but not in a DMSO-water mixture, where globules are expected. In comparison, above the LCST of ~31°C, PNIPAM dissolved in 0 mol% DMSO (100 mol% water) becomes turbid due to LCST-induced globule formation.

Since globules scatter more light than polymer coils, the coil-to-globule transition can be characterized by measuring the cloud point temperature of the PNIPAM solutions at different x_{DMSO}. These cloud point temperatures of PNIPAM solutions define the boundaries of the phase diagram in Figure 2.16. It is readily observed that the PNIPAM solutions experience LCST and upper critical solution temperature (UCST) type behavior at low and high x_{DMSO} values, respectively. Overlaid on the phase diagram are photos of cross-linked PNIPAM hydrogels synthesized at 60°C (rectangle-shaped) and 10°C (circle-shaped). The optical transparencies of the hydrogel samples are consistent with the phase diagram obtained from turbidity measurements of the non-crosslinked PNIPAM solutions. Specifically, hydrogels polymerized within the globule region exhibited high levels of scattering, resulting in an opaque white appearance, while those polymerized within the coil regions appeared optically transparent. Additionally, unlike in non-crosslinked PNIPAM solutions, the globules formed in the PNIPAM hydrogels were permanent due to chemical crosslinking. Hence, hydrogels polymerized within the globule region remained

white, despite being immersed in 25°C DI water for 24 hours post-synthesis; all the hydrogel images in Figure 2.16 were taken after complete rinsing in room temperature deionized water. We confirmed that the cononsolvency-induced opacity does not significanctly affect the pore size homogeneity, nor does it significantly limit sample size from UV penetration issues, due to the fast photopolymerization reaction. SEM micrographs were taken of these crosslinked PNIPAM hydrogels synthesized with cononsolvency photopolymerization (Figure 2.17) showing closed pore and open pore structures for hydrogels synthesized within the coil and globule regions, respectively. FTIR was also performed on $x_{0.4}$ and $x_{1.0}$ hydrogels polymerized at 60°C to confirm the two are chemically identical.

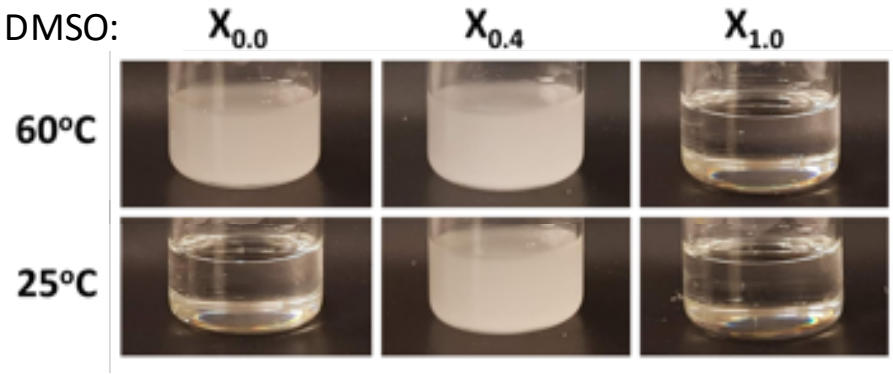

Figure 2.15 Photographs showcasing the appearance of 1 mg/mL PNIPAM solutions at various DMSO mole fractions and temperatures. In pure water (0 mol% DMSO) the PNIPAM solution is transparent at 25 °C and opaque at 60 °C, corresponding to the polymer's LCST transition.

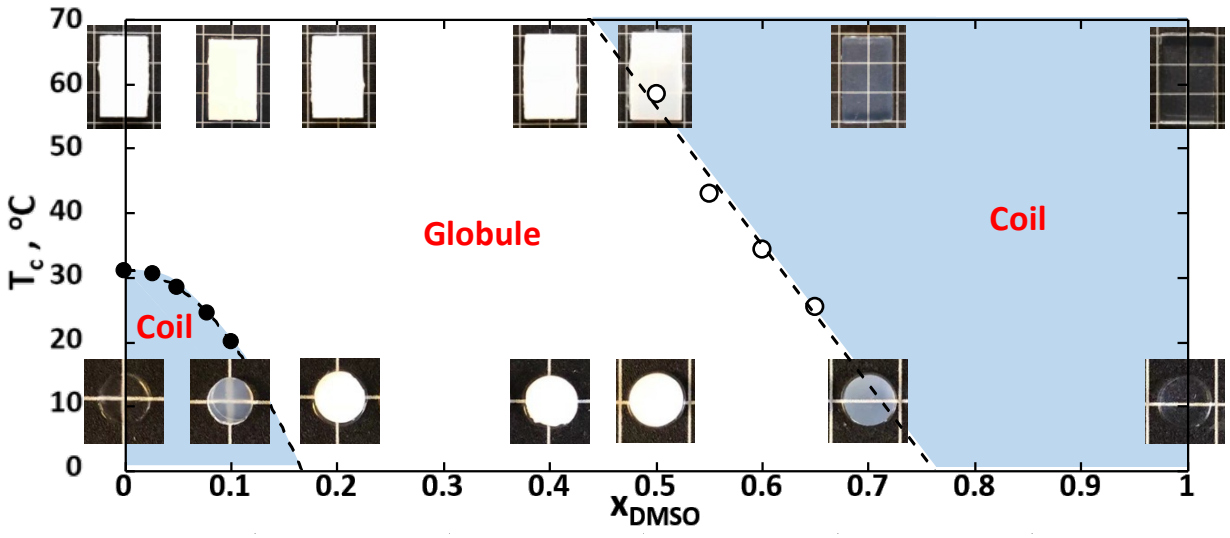

Figure 2.16 DMSO mole fraction – temperature phase diagram collected from UV-VIS transmittance experiments on PNIPAM solutions of varying DMSO compositions. The temperature at which a 50% change in transmittance is noted to be the transition temperature. Overlaid upon the phase diagram are photographs of hydrogels synthesized at the corresponding DMSO mole fractions and temperatures, demonstrating consistency between the solution phase behavior and the resulting hydrogel morphology.

2.3.3 Pore Structure Tunability

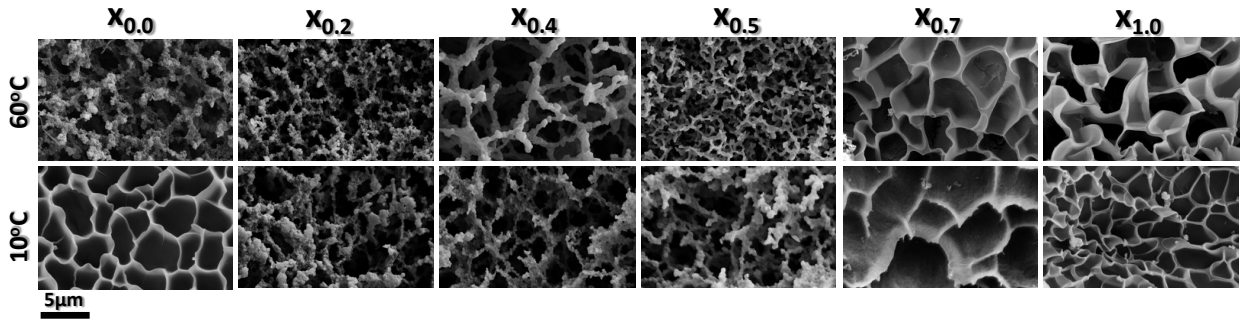

Figure 2.17 PNIPAM pore structure tunability based on DMSO-water mixed solvent composition and UV curing temperature.

Figure 2.18 depicts the time-dependent deswelling behavior of PNIPAM hydrogels synthesized at 60°C in different x_{DMSO} environments; the $x_{0.4}$ sample exhibited the highest swelling ratio and deswelling rate. This is consistent with the SEM micrograph of $x_{0.4}$ (Figure 2.17) depicting an open pore structure with large and highly interconnected pores compared to gels synthesized at other x_{DMSO} conditions. In Figure 2.19, Young's moduli were calculated from stress-strain measurements obtained with dynamic mechanical analysis (DMA) and overlaid on top of swelling ratio and deswelling rate extracted from Figure 3a. Compared to the closed pore PNIPAM synthesized at $x_{1.0}$ (the control), the open pore PNIPAM synthesized at $x_{0.4}$ resulted in a 2-fold increase in swelling ratio and Young's modulus, and a 6-fold increase in deswelling rate. A discontinous increase in swelling ratio and deswelling rate is readily observed as DMSO mole fraction reduces from $x_{0.5}$ to $x_{0.4}$, despite gravimetric measurements indicating that water content of the final prepared hydrogels decreases gradually with decreased DMSO mol fraction; this supports the idea that the diffusion enhancement comes primarily from the pore structure enabling

faster 3D transport, rather than the porosity. Toughness was evaluated by placing a 500g load on top of the $x_{1.0}$ and $x_{0.4}$ gels (Figure 2.20); the $x_{1.0}$ hydrogel, with a typical closed pore structure, was destroyed while the $x_{0.4}$ hydrogel with open pore structure remained intact.

As described by the phase diagram in Figure 2.16, the cononsolvency phenomenon is not only a function of solvent composition, but also a function of temperature. Hence, the effect of reaction temperature on hydrogel pore structure and performance was also investigated. The temperature of the $x_{0.4}$ prepolymer solutions were measured throughout the duration of the cononsolvency photopolymerization reaction under ambient conditions, active cooling, and pulsed illumination with active cooling, corresponding to reaction temperatures of 60°C, 40°C, and 10°C, respectively. The time-dependent deswelling and swelling of these $x_{0.4}$ PNIPAM hydrogels are measured upon sequential immersion into 60°C and 25°C baths, respectively. It is readily observed that gels fabricated at all three reaction temperatures exhibited the same swelling ratio and deswelling performance, while the gel synthesized at 10°C swelled the fastest. Based on the SEM micrographs of these three hydrogels, this enhanced transport can be attributed to the smaller, but still highly interconnected, pore structure of the 10 °C $x_{0.4}$ gel that results in higher capillary pressure. Normalized swelling and deswelling rates of the 10°C sample were calculated by dividing the volume change rates by the swollen hydrogel volume, then compared to those calculated from some representative literature focusing on fast stimuli-responsive PNIPAM hydrogels (Figure 2.21).[46–59] In this comparison, it is readily observed that both normalized swelling and deswelling rates in this work are about an order of magnitude higher than what has been reported. Comparing to the few works measuring both the deswelling rate and Young's

modulus of their PNIPAM hydrogels, this work demonstrates a record-breaking order of magnitude improvement in both properties without compromise (Figure 2.22).

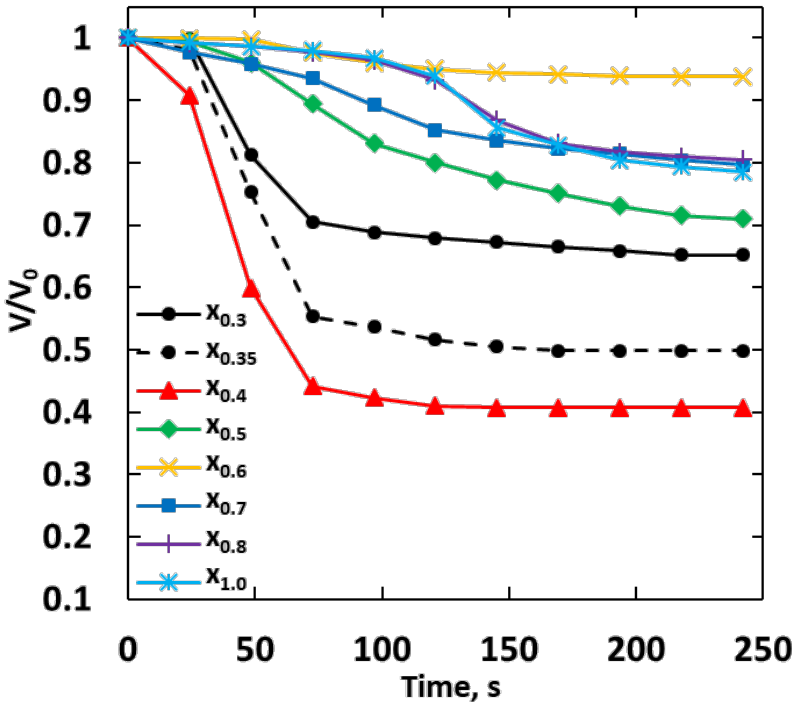

Figure 2.18 Swelling kinetics of thermo-responsive PNIPAM hydrogels synthesized in DMSO-water mixtures with various DMSO mole fractions.

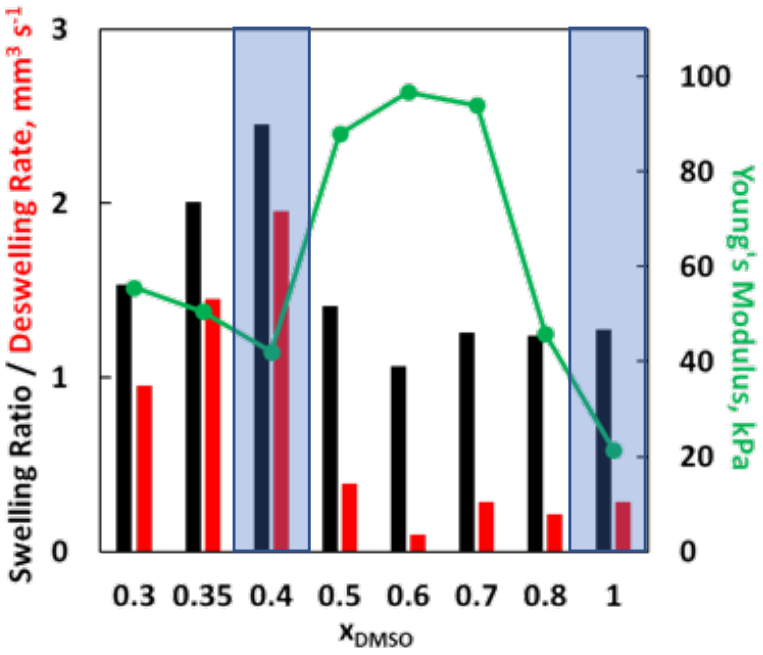

Figure 2.19 Compiled swelling and Young's modulus data for thermos-responsive PNIPAM hydrogels synthesized in DMSO-water mixtures with various DMSO mole fractions. Hydrogel samples synthesized in 40 mol% DMSO produce higher swelling ratio, de-swelling rate, and Young's modulus than those synthesized in pure 100 mol% DMSO.

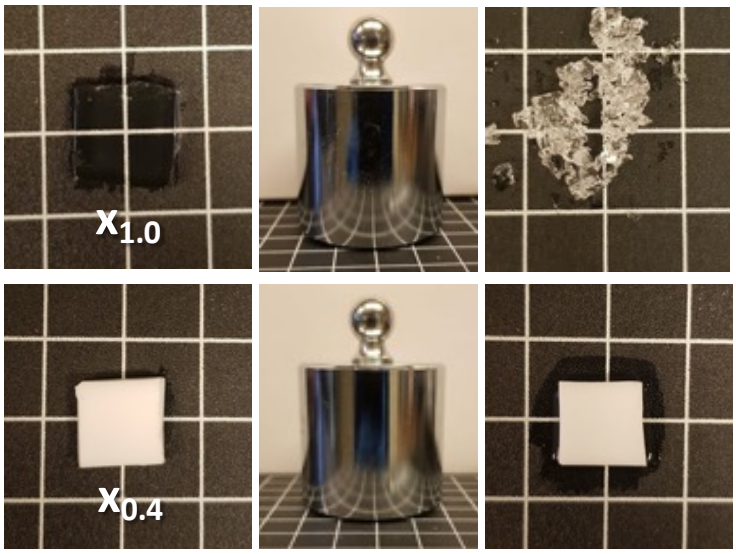

Figure 2.20 Compression resistance of open-cell PNIPAM hydrogels synthesized in mixed solvent, compared to conventional closed-cell PNIPAM hydrogels. A load of 500g was used.

.

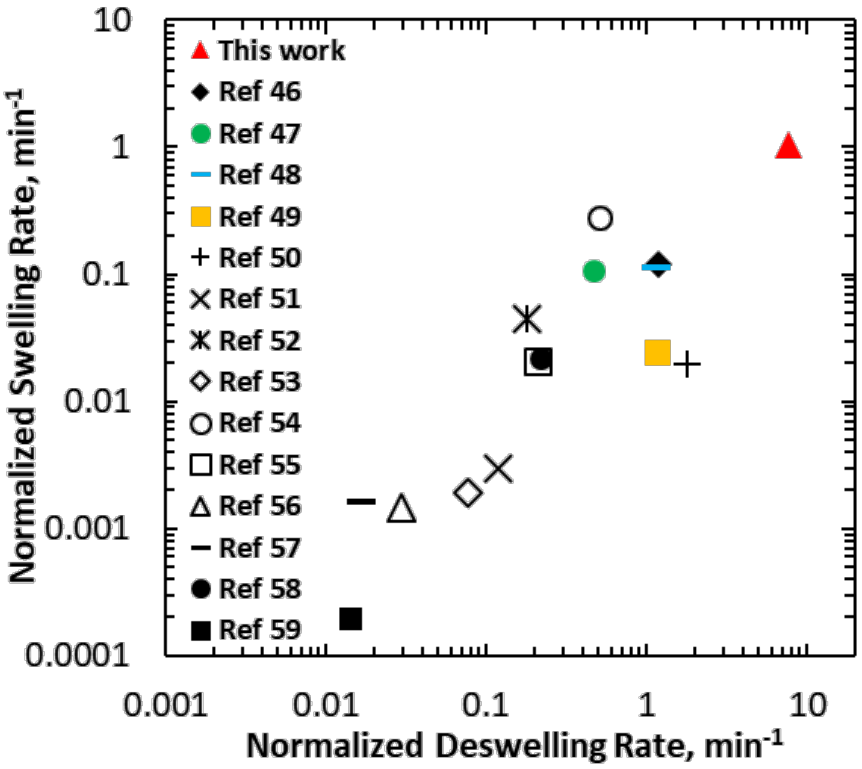

Figure 2.21 Swelling and De-swelling rates of various hydrogels, compared to our optimized thermos-responsive hydrogel synthesized through mixed solvent cononsolvency polymerization. To allow comparison across all samples, the swelling and de-swelling rates were normalized by the corresponding initial gel volumes.

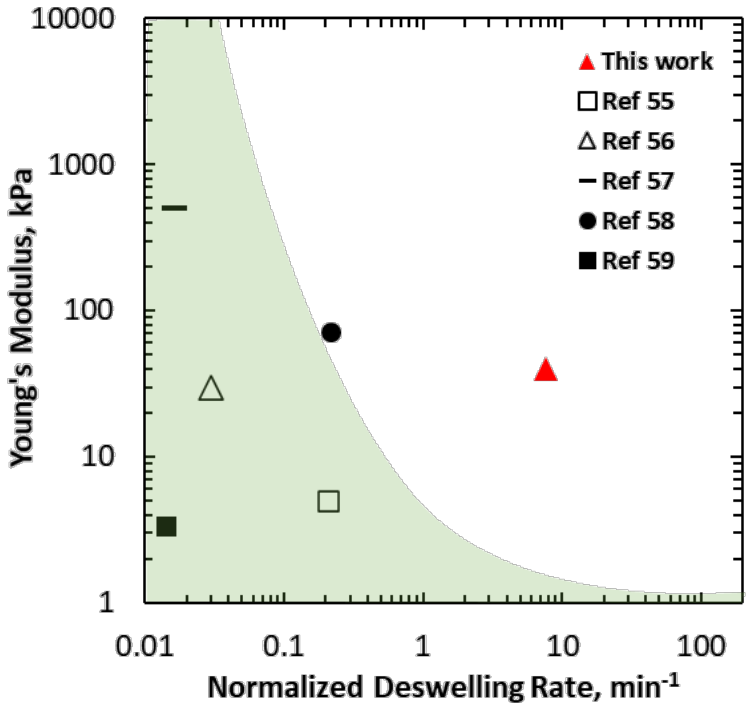

Figure 2.22 Normalized de-swelling rates and Young's moduli of various reported hydrogels works in comparison to the PNIPAM hydrogel synthesized using the cononsolvency approach with DMSO-water mixtures.

The cross-linking density can be calculated using the Flory-Rehner rubber elasticity theory, which is a simple approach that only utilizes swelling measurements. The equation is as follows:[97]

$$-[\ln(1-\nu_2)+\nu_2+\chi_1(\nu_2)^2]=V_1 n\left[(\nu_2)^{\frac{1}{3}}-\frac{\nu_2}{2}\right]$$

Equation 11

In the above, ν_2 represents the volume fraction of the polymer in the hydrogel, χ_1 represents the Flory-Huggins interaction parameter for PNIPAM-water[98] which is equal to 0.5, V_1 represents the solvent (water) molar volume (18 cm^3 mol), and n represents the density of linear polymer segments bound by cross-links on both ends. ν_2 can be expressed in terms of the polymer volume ($V_{polymer}$) and gel volume (V_{gel}), as follows:

$$\nu_2=\frac{V_{polymer}}{V_{gel}}=\frac{\left(\frac{m_{polymer}}{\rho_{polymer}}\right)}{V_{gel}}$$

Equation 12

V_{gel} can be measured directly from the dimensions of the regular-shaped hydrogel or with a pycnometer; $m_{polymer}$ is the dry mass of this hydrogel after freeze-drying. The density of the polymer ($\rho_{polymer}$) can be measured via the following volume relationship:

$$V_{gel} = \frac{m_{water}}{\rho_{water}} + \frac{m_{polymer}}{\rho_{polymer}}$$

Equation 13

This can be re-written in the following:

$$\rho_{polymer} = \frac{m_{polymer}}{V_{gel} - \frac{m_{water}}{\rho_{water}}}$$

Equation 14

Here, m_{water} represents the mass of the wet hydrogel minus $m_{polymer}$. With these relationships, ν_2 for photo- and thermo- polymerized PNIPAM can be calculated, and hence n can be obtained. Furthermore, the average molecular weight of cross-linked polymer segments (M_c) can also be calculated using the following modified equation,[99] assuming the hydrogel is composed of a completely continuous polymer network:

$$-[\ln(1-\nu_2) + \nu_2 + \chi_1(\nu_2)^2] = \left(\frac{V_1}{\bar{\nu} M_c}\right)\left[(\nu_2)^{\frac{1}{3}} - \frac{\nu_2}{2}\right]$$

Equation 15

Here, $\bar{\nu}$ represents the specific volume of the polymer in the hydrogel, represented by the following:

$$\bar{\nu} = \frac{V_{gel}}{m_{polymer}}$$

Equation 16

Table 1 lists the key values of relevant properties calculated with this method.

Table 1: Values of mass fraction of water, volume fraction of polymer, n, and Mc for photo- and thermo-polymerized hydrogels corresponding to 40 mol% DMSO-water.

	Photo	Thermo
m_{water}	0.87	0.85
$V_{polymer}$	0.26	0.27
n (mol/cm^3)	7.56 x 10^{-4}	9.37 x 10^{-4}
M_c (g/mol)	149	140

2.4 Newly Enabled Capabilities

2.4.1 In-air operation of hydrogels

One of the significant limitations of hydrogels is the requirement of submersion in water: due to severe transport limitations, hydrogels cannot be exposed to air for long durations because evaporation rates are generally higher than swelling rates, resulting in undesired de-swelling and

drying. We fabricated $x_{1.0}$ and $x_{0.4}$ PNIPAM hydrogel pillars and exposed them to air for 24 hrs to dry; remarkably, these pillars were able to support themselves upright in air due to their rigidity. Afterwards, we added DI water to the base of the pillars and observed the swelling behaviors. The $x_{0.4}$ pillar was able to rehydrate itself in air completely within 60 min, while the $x_{1.0}$ pillar could not, no matter how long we waited (Figure 2.23). This suggests that cononsolvency photopolymerization for fabricating spongy open pore hydrogels presents a promising direction for in-air hydrogel applications, as long as there is a constant water supply.

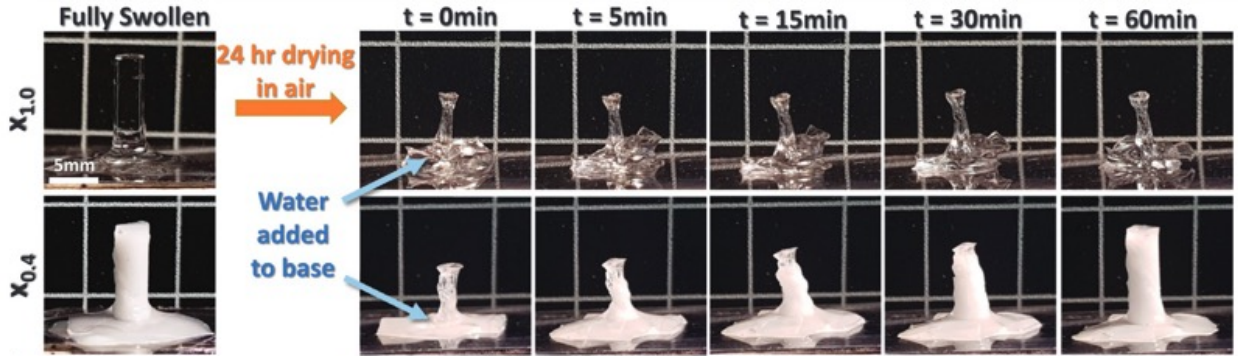

Figure 2.23 In-air swelling behaviors of $x_{1.0}$ and $x_{0.4}$ gel pillars, which were dried in air first and then supplied with water at the base.

2.4.2 3D Printability

The cononsolvency photopolymerization technique is also compatible with 3D printing, as shown in Figure 2.24 where the swelling behaviors of printed $x_{1.0}$ and $x_{0.4}$ PNIPAM flower structures were characterized; these structures were printed using modified $x_{1.0}$ and $x_{0.4}$ precursors that utilize the ideal photo-initiator for our home-built 3D printer. The flowers can be observed to bloom when immersed into a 25°C water bath from 60°C; Figure 2.24 depicts that the $x_{0.4}$ flower

was able to fully bloom six times faster than the $x_{1.0}$ flower. To further showcase the 3D printability, we printed various other structures from the modified $x_{0.4}$ precursor and confirmed open-celled pore structure with SEM (Figure 2.25).

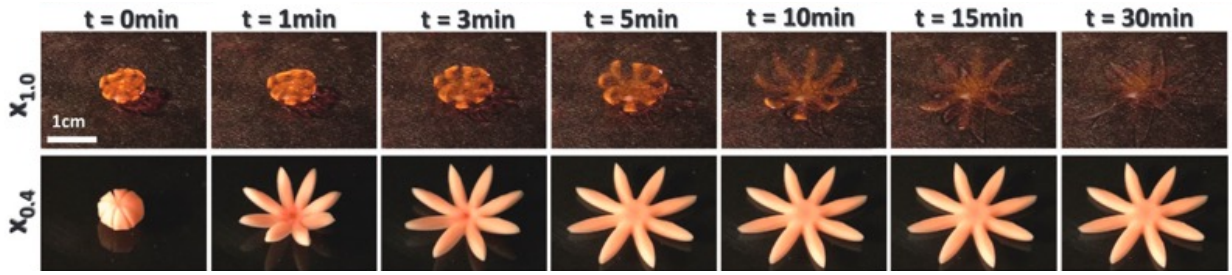

Figure 2.24 Swelling-induced blooming behaviors of 3D printed $x_{1.0}$ and $x_{0.4}$ gel flowers shrunken at 60°C then immediately immersed in 25°C water.

Figure 2.25 3D printed octet-truss, gyroid, and ovoid structures from a modified $x_{0.4}$ PNIPAM precursor solution (left) and SEM of the 3D printed PNIPAM, confirming open-celled pore structure (right).

2.4.3 Generalizability

Mukherji et al. suggested that polymer collapse in miscible good solvents is not specific to PNIPAM systems, rather it is generic.[60] The work specifies that three criteria must be met to achieve cononsolvency-induced polymer collapse: the pure solvent and pure cosolvent must both be able to fully dissolve the polymer, the solvent and cosolvent must be mutually miscible, and the cosolvent must behave as a stronger solvent for the polymer than the solvent. After exploring the role of cononsolvency in fabricating open pore gels from PNIPAM, we extended the principle of cononsolvency photopolymerization to polyacrylamide (PAM) and poly-N-tertbutylacrylamide-co-polyacrylamide (PNTBAM-co-PAM) hydrogel systems (Figure 2.26) and fabricated similar open pore structures (Figure 5b). As expected, these hierarchically structured open pores resulted in a white opaque appearance, similar to what was observed in PNIPAM. It was observed that for PAM hydrogels, the closed pore and open pore structures occurred at $x_{0.0}$ and $x_{0.6}$ rather than the expected $x_{1.0}$ and $x_{0.4}$ DMSO mole fractions, respectively; in other words, the phase behavior is inverted. This is likely due to the higher hydrophilicity of PAM, in which water acts as a stronger solvent than DMSO, in contrast to PNIPAM and PNTBAM-co-PAM systems; when the mole fraction is re-written with respect to water instead of DMSO, one obtains the expected $x_{1.0}$ and $x_{0.4}$ for closed pore and open pore structures, respectively. To confirm enhanced diffusion resulting from the open pore structure, a capillary wicking experiment was used since PAM and PNTBAM-co-PAM do not demonstrate clear thermo-responsiveness (Figure 2.27); a fresh tissue is applied to the surface of the hydrogels every minute to absorb water, and the mass loss is recorded (Figure 2.28), confirming that for all three hydrogel systems, the opaque open porous polymer structure exhibited increased water loss due to capillary wicking.

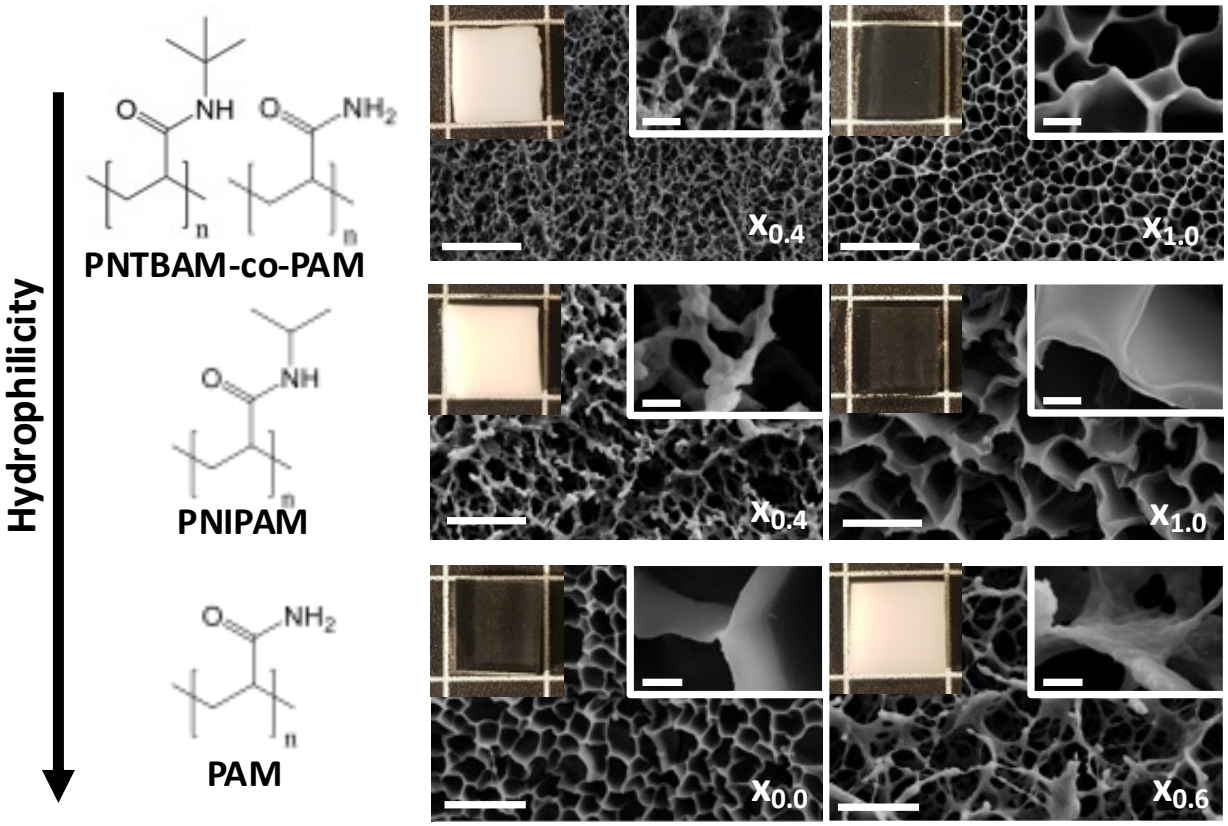

Figure 2.26 Chemical structures of PNTBAM-co-PAM, PNIPAM, and PAM in order of increasing hydrophilicity (left) and SEM micrographs of PNTBAM-co-PAM (top), PNIPAM (middle), and PAM (bottom) hydrogels synthesized at different DMSO mole fractions, demonstrating both open pore and closed pore structures. Inset images depict photographs of the corresponding hydrogels (0.95 cm × 0.95 cm × 3 mm). Scale bars: 10 μm (low mag) and 1 μm (high mag).

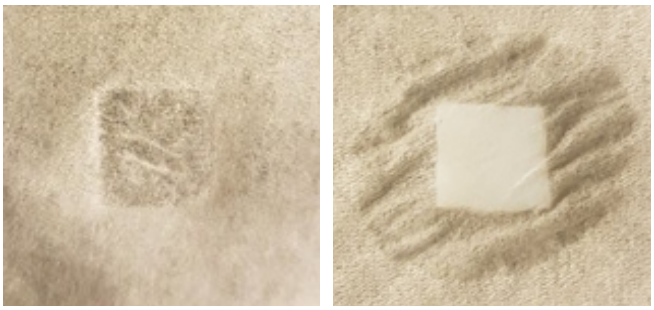

Figure 2.27 Capillary wicking of water by a tissue after 1 minute for $x_{1.0}$ PNIPAM (left) and $x_{0.4}$ PNIPAM (right) hydrogels.

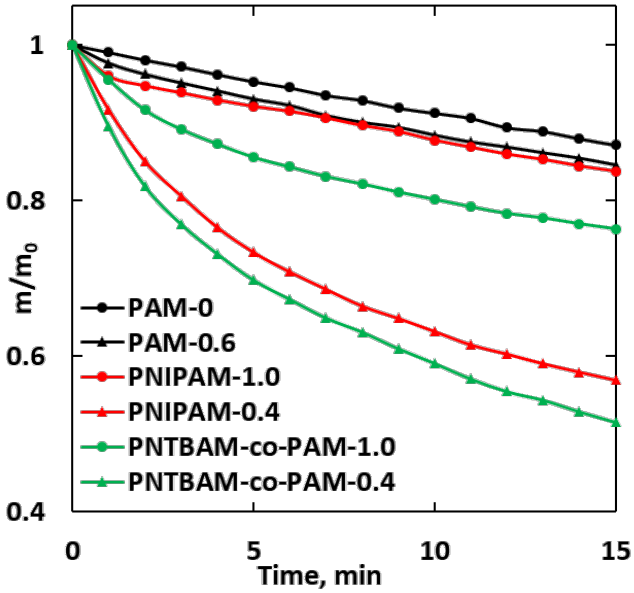

Figure 2.28 Mass change over time for closed pore and open pore PNTBAM-co-PAM, PNIPAM, and PAM hydrogels during capillary wicking of water.

Chapter 3: Chemistry-Impartial Gel Polymer Electrolytes for Batteries

3.1 Background

3.1.1 Conventional Li-Ion Battery Composition

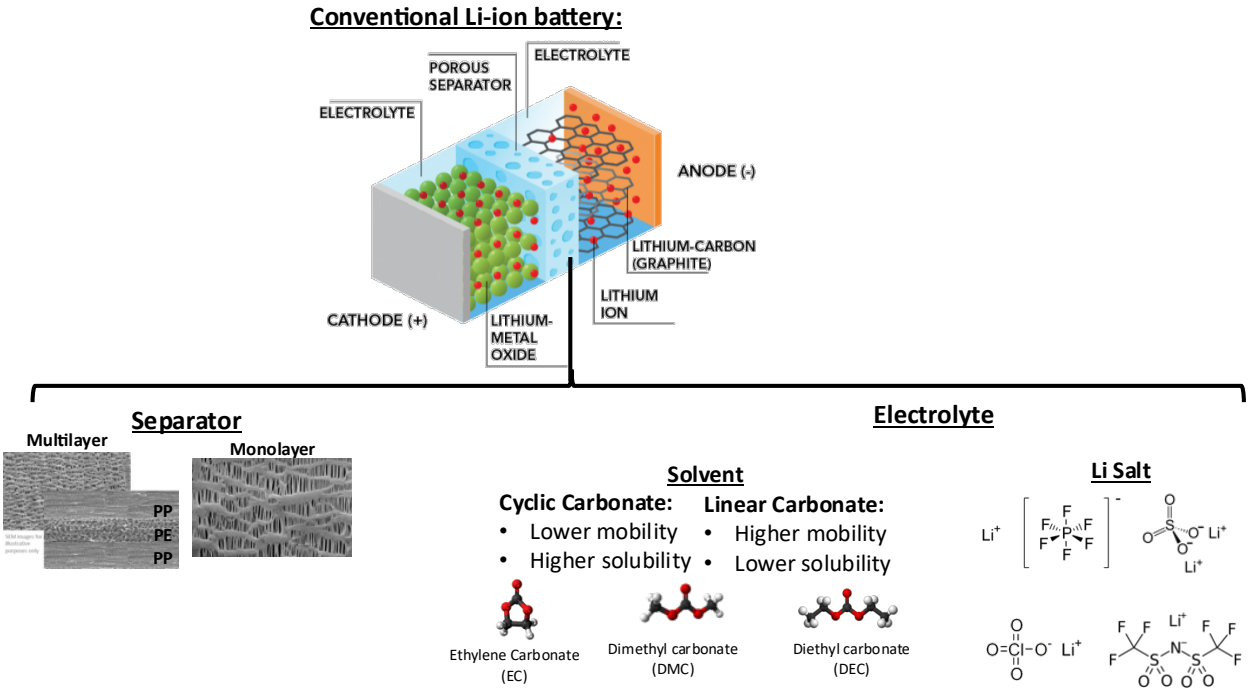

Figure 3.1 Composition of typical Li-ion batteries, with exploded view of the porous separator and electrolyte components.

3.1.2 Critical Challenges in current state-of-art technologies

As global energy demands continue to increase and the harmful effects of atmospheric carbon continue to be investigated, there presents an urgent need for accelerating the advancement of sustainable energy. Clean and sustainable sources such as solar and wind are limited by their

intermittency, requiring an energy storage mechanism to utilize them during off-peak hours. Great efforts continue to be invested into new battery technologies to enable the supplementation, and hopefully the eventual replacement, of our current fossil fuels-dominated energy economy. Such energy storage solutions can play a key role in advancing electric vehicles, grid-scale energy storage, medical devices, wearable electronics, and soft robotics.

Current battery technologies are limited by their capacity, rate capability, safety, and lifetime. Battery-technologies still lag behind chemical fuels in terms of both gravimetric and volumetric energy densities (Figure 3.2). In recent years several approaches have been taken to address these critical bottlenecks. The development of new cathode and anode materials have enabled improved electrolyte-electrode interface stability, improving cell lifetime, increasing operating voltage, and bosting cell capacity. Pseudocapacitive behavior in dense oxides has demonstrated that surface electrochemical reactions may occur faster than intercalation chemistry, resulting in improved rate capabilities. Aqueous and solid-state electrolytes aim to the eliminate the risks of flammability and explosions from shorts and thermal runaway events. Dendrite suppression via coatings, controlled ion transport, and electrolyte engineering have been developed with the aim of improving cycle life. One of the causes of accelerated dendrite growth includes the establishment of non-homogeneous ion transport from uneven charge distribution at high charging and discharging rates (Figure 3.3). In specific, during charging, if the transport of lithium ions is much slower than the rate of reaction, a low concentration region will occur at the graphite surface causing an increase in ohmic resistance and subsequent ion pile-up. In contrast, if the ion transport across the electrolyte barrier is much faster than the rate of reaction at the graphite surface, the cell can maintain homogeneous ion concentration throughout the cross-section, avoid

increase in ohmic interfacial resistance, and maintain homogeneous ion transport, thus suppressing dendrite growth. The reaction-dominated regime with accelerated dendrite growth is favored at higher C-rates. As energy demands increase, there lies a need to resolve the performance bottleneck at these high charging rates.

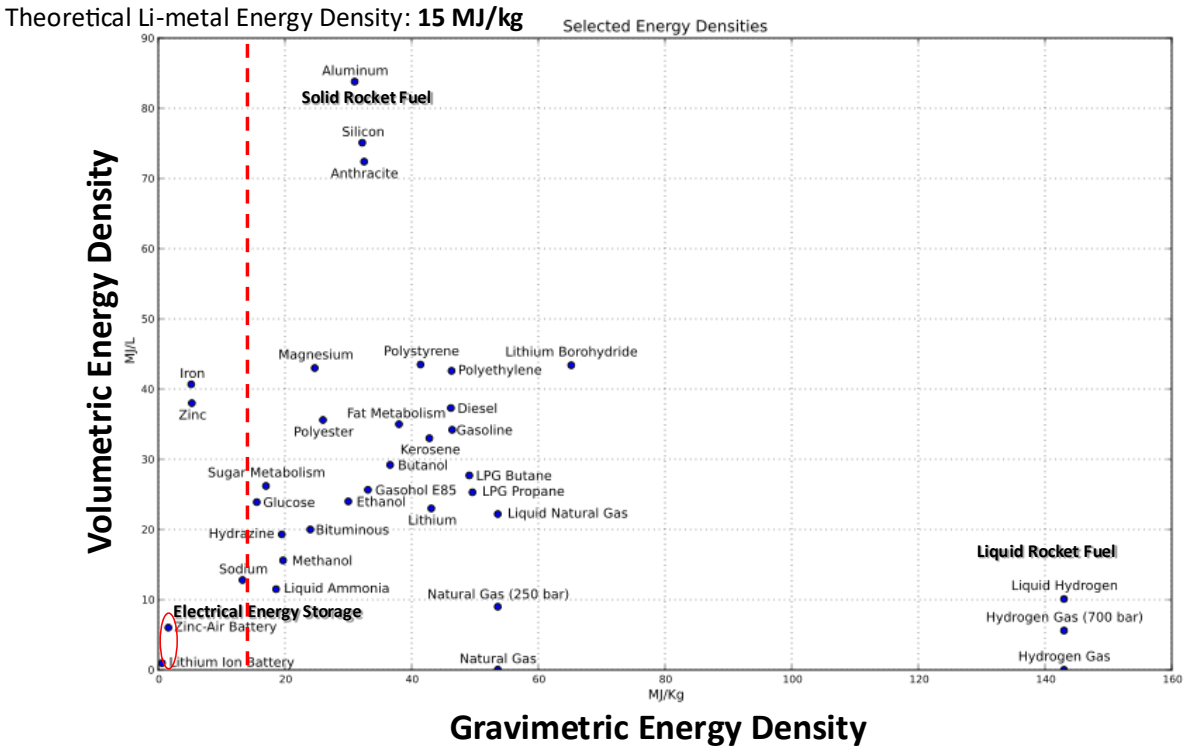

Figure 3.2 Volumetric and Gravimetric energy density landscapes, showcasing electrical energy storage technology's low placement with respect to other forms of energy. The red dotted line represents Li-metal's theoretical gravimetric energy density, compared to the circled region depicting current state of battery technologies.

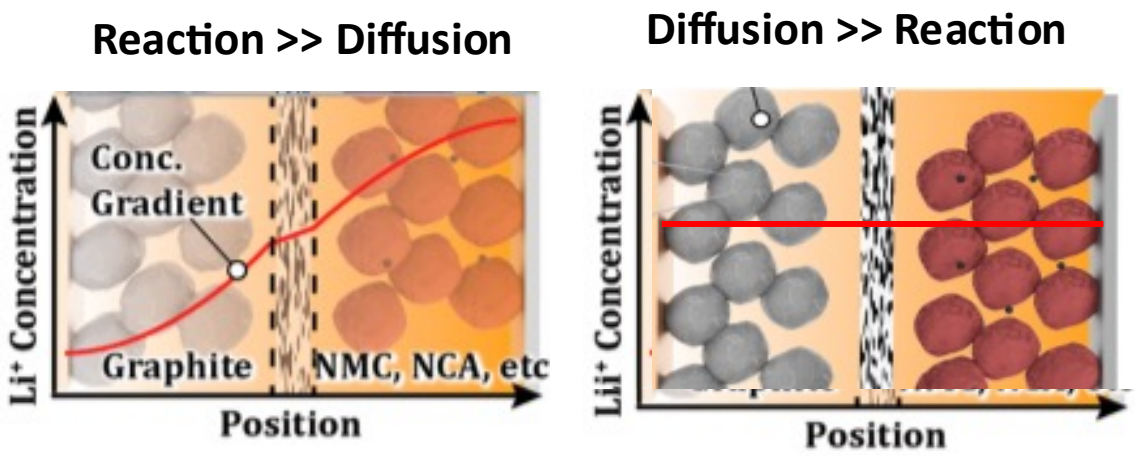

Figure 3.3 Ion concentration gradients across battery cross section for a diffusion-limited process with faster reaction kinetics (left) and reaction-limited process with slower reaction kinetics (right).

3.1.3 Chemistry-Neutral Roadmap towards accelerated battery materials discovery

Using current material platforms to address these contemporary problems in energy storage involves laborious optimizations of chemistries and formulations, in addition to time-intensive cycling tests that take weeks to months. To aid in the rapid discovery of new battery cell materials and designs, researchers have turned to powerful, high-throughput, and automated design principles utilizing Artificial Intelligence (AI) and machine learning (ML); in doing so, a limited but carefully selected sample of cell data can be analyzed to optimize cell material formulations and understand more complex interfacial phenomena. As current Li-ion batteries approach their performance limits, new methods must be devised to rapidly explore new cell designs and interpret cell data.

Battery 2030+, a European Union initiative led by 20+ research institutes, is implementing a roadmap for rapidly accelerating major breakthroughs in battery technologies, moving away

from specific chemistries and emphasizing a "chemistry-neutral approach as a generic toolbox for transforming the way we develop and design batteries" with the objective of achieving a 5-10 fold increase in the rate of discovery of novel battery materials and interfaces.[100] This initiative is based on creating a Battery Interface Genome (BIG), a database of detailed cell data encapsulating various ion transport and interfacial phenomena, coupled with a Materials Acceleration Platform (MAP) that combines automated synthesis, characterization, simulations, data analysis, data mining, AI, and ML (Figure 3.4).

Some of the biggest challenges of integrating cell data with AI/ML platforms involve the standardization of cell data protocols and the careful selection of source datasets to ensure valuable and reliable data output. Battery 2030+ aims to address these challenges via a consortium initiative and a chemistry-neutral approach; however, most currently used anodes, cathodes, and electrolytes exhibit chemistry- and design-specific cell performance which may obstruct or hinder this platform's full potential for accelerated battery materials discovery. Efforts to standardize cell performance predictions across various battery chemistries may experience significant challenges, since measured cell data derives from non-linear, sometimes non-measured, system-level properties coming from the individual cell components.

To fully leverage these chemistry-impartial AI/ML roadmaps, rapidly accelerate new materials discovery, and curb challenges in standardizing cell modeling across broad chemistries, it is highly desirable to concurrently develop, implement, and test chemistry-impartial cell materials: such chemistry-neutral cell materials can broaden the scope and efficacy of AI/ML

platforms towards rapid materials discovery. Currently, battery separators are the only cell component that demonstrate comparable behavior in diverse electrolyte and electrode environments, and even they are not fully cross-compatible between aqueous and organic chemistries; conventional lithium-ion separators, for example, are typically composed of polypropylene (PP) or polyethylene (PE) and are extremely hydrophobic, suffering from incompatibility with aqueous-based electrolytes, such as those used in zinc-ion batteries. Glass fiber separators, while offering amphiphilic solvent compatibility, are mechanically weak and result in accelerated dendrite growth, short cell life, and significant safety risk if swollen with flammable electrolytes without supplementation with a tough PP or PE layer. Gel Polymer Electrolytes (GPE's) arose as a class of quasi-solid materials to bypass the safety concerns of conventional flammable liquid electrolytes and address the poor interfacial contact and ionic conductivity concerns of solid-state electrolytes; however, current GPE's still suffer from fundamental limitations in their ionic conductivities, mechanical properties, and multi-chemistry compatibility.

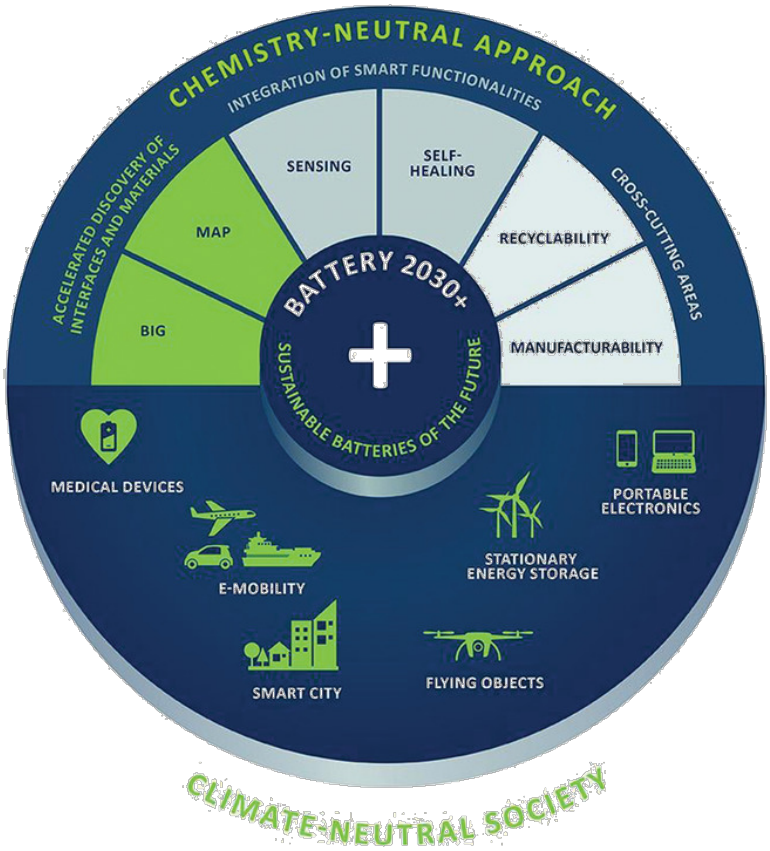

Figure 3.4 Overview of Battery 2030+ chemistry-neutral roadmap for accelerated battery materials discovery. Chemistry-neutral battery materials can highly benefit the Artificial Intelligence/Machine Learning-assisted Battery Interface Genome (BIG) and Materials Acceleration Platform (MAP).[100]

3.2 Cononsolvency Approach

3.2.1 Objective

Commercial separators experience many drawbacks such as high flammability, low cycle life, and mechanical instability. GPE's arose to improve the safety and mechanical stability but came at the compromise of low ionic conductivity which manifests in the form of low cell

performance during battery cycling. We aim to build upon this GPE framework to create a synthesis platform for generating ultra-strong, highly diffusive polymer networks that can be easily converted into GPE's compatible with both aqueous and organic electrolytes (Figure 3.5): this synthesis platform was able to produce GPE's that break the conventional ionic conductivity-mechanical strength trade-off in porous materials, outperforming commercial polypropylene (PP) separators, glass fiber separators, and state-of-the-art GPE's.

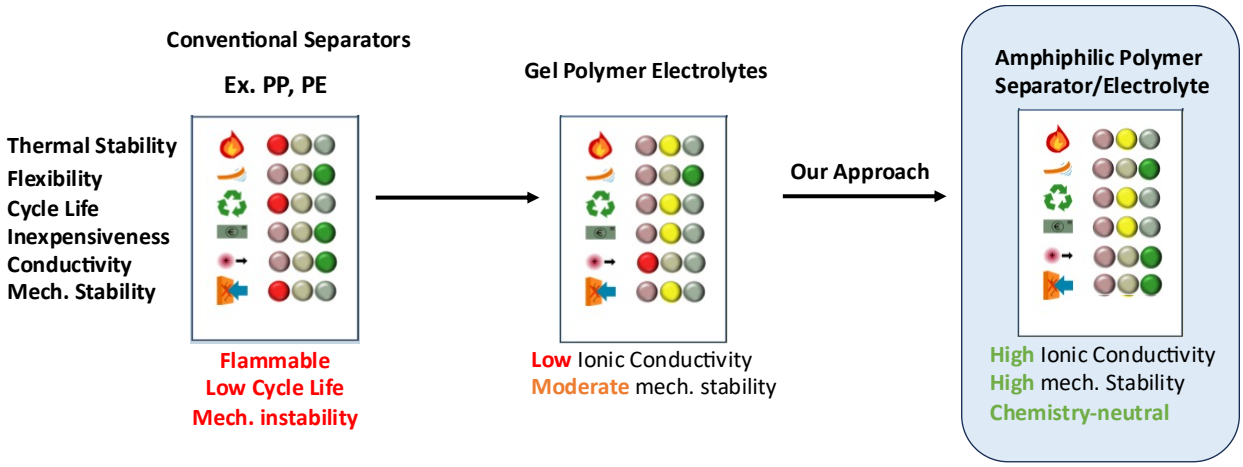

Figure 3.5 Schematic showcasing the relative thermal stability, flexibility, cycle life, inexpensiveness, conductivity, and mechanical stability of conventional battery separators compared to state-of-the-art gel polymer electrolytes and our approach's chemistry-impartial tough highly diffusive gel polymer electrolyte.

3.2.2 Design Principle

We utilize cononsolvency to tailor the cross-linked polymer structure, maximizing the pore wall densification and pore interconnectivity to simultaneously improve the mechanical properties

and diffusive properties of the networks (Figure 3.6). Subsequently, we swell these networks with the appropriate liquid electrolytes to enable functionality in Zn-ion, Li-ion, and Li-metal batteries.

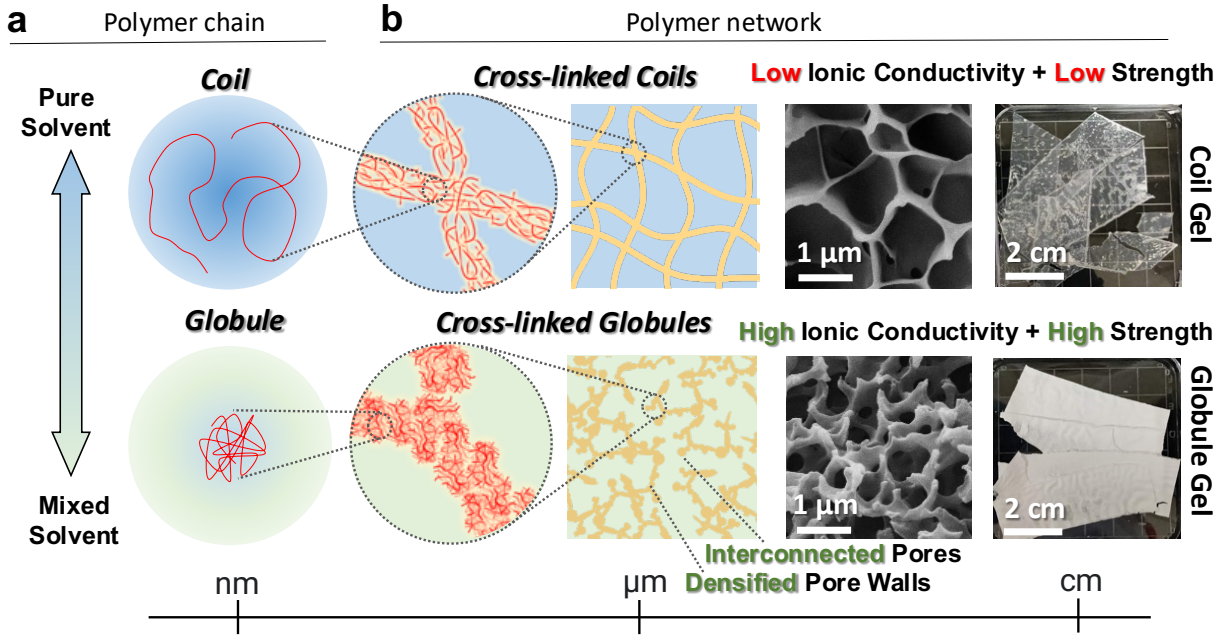

Figure 3.6 Overview of cononsolvency-induced pore structure control of covalently cross-linked amphiphilic PNIPAM networks. a) linear polymer chain taking an extended coil conformation in pure solvent (top) and cononsolvency-induced collapsed globule conformation in mixed solvent (bottom). b) cross-linked network of interconnected coils in pure solvent (top) and interconnected globules in mixed solvent (bottom) resulting in drastically different pore morphologies and material properties.

3.2.3 Formulation Optimization

Building upon the previous characterization of PNIPAM gels synthesized in the nine different aqueous mixed solvents, we also investigated the ion transport and mechanical properties

of the gels synthesized from the 20wt% precursors. The gels were swollen with 1M Li_2SO_4 electrolyte then characterized using electrical impedance spectroscopy (EIS) and dynamic mechanical analysis (DMA). Hydrogel samples produced using $x_{0.4}$ DMSO yielded the highest ionic conductivity, 17 mS cm-1, and the highest tensile strength, 79 kPa (Figure 3.7). Across all nine mixed solvents investigated, DMSO-water consistently fared the best in terms of maintaining open-network pore structure, high ionic conductivity, and high tensile strength, with minimal suppression of phase separation at higher precursor concentrations.

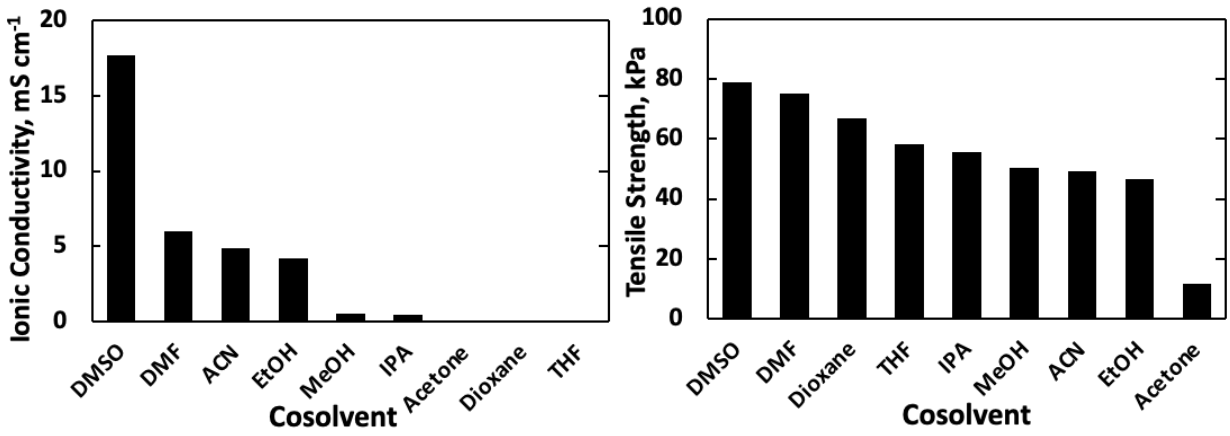

Figure 3.7 Ionic conductivity and tensile strength of PNIPAM porous polymers synthesized in different aqueous mixed solvents. DMSO-water ranks the highest in terms of performance, consistent with previous phase behavior results indicating that this mixed solvent system promotes phase separation the most.

While 20 wt% and 70 wt% precursors have demonstrated DMSO-water superiority in terms of promoting cononsolvency-driven phase separation and generating open-celled pores with simultaneously improved ionic conductivity and tensile strength, the mechanical properties of such

networks still do not meet the minimum requirements to be viable for implementation in battery cells; efforts to freeze-dry and integrate these porous polymers into any battery coin cells as GPE's, after swelling with liquid electrolyte, will be faced with disappointingly high rates of battery shorting at the crimping step when the cell components are compressed at 500-1000 psi. Following the selection of DMSO-water as the ideal solvent mixture to induce cononsolvency-driven phase separation in PNIPAM, it is essential to optimize the formulation towards improved mechanical strength while maintaining high ionic conductivity and pore interconnectivity.

An increase in the precursor monomer concentration, and hence polymer density, was pursued towards improved mechanical properties; however as noted before, monomer concentrations at 800 mg/mL using $x_{0.4}$ yielded closed-cell pores. Since cononsolvency has been shown to exhibit concentration dependence, we implemented a ladder study to simultaneously optimize the monomer concentrations and mixed solvent compositions by examining the highest concentrations of monomers allowed before running into solubility issues or reversion back to closed-cell pores. We discovered that for the PNIPAM system, $x_{0.15}$ DMSO can be used to increase the monomer concentration to 115wt% while still maintaining open-celled pore structure, macroscopically taking a white opaque appearance (Figure 3.8). Through subsequent studies, we confirmed indeed that the optimal open-celled pore structure shifts downwards from $x_{0.4}$ at 20 wt% precursor concentration to $x_{0.15}$ at 115 wt% precursor concentration.

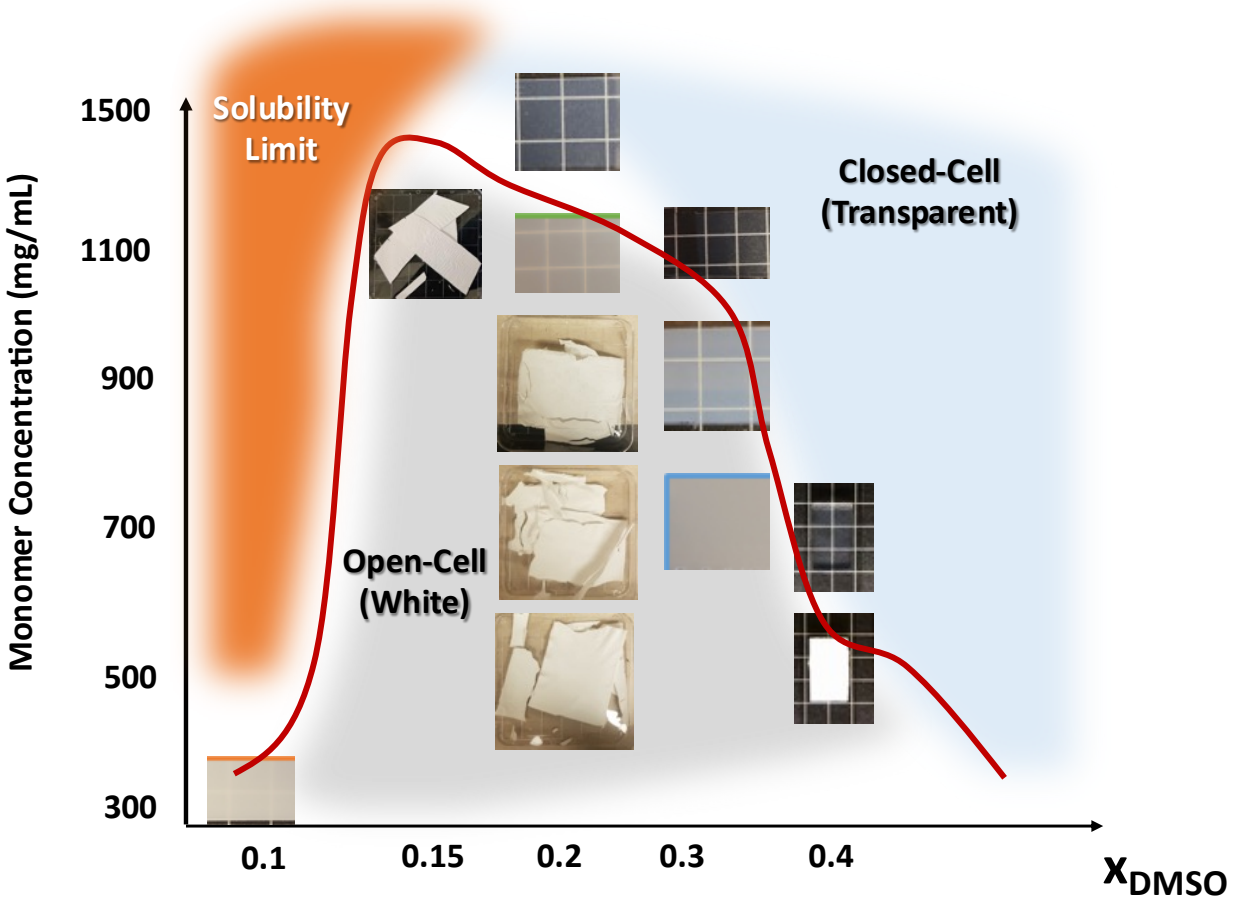

Figure 3.8 Schematic showing the various recipes probed while optimizing the gel polymer electrolytes towards maximum ionic conductivity/diffusivity and mechanical strength. Precursor monomer concentration and DMSO-water mole fraction were tuned to find the recipe enabling maximum polymer loading while still maintaining the open-celled pore structure, characterized by the sample's white appearance. At low DMSO mole fractions, the precursors experience low solubility with respect to NIPAM monomer, while at higher DMSO mole fractions, the cross-linked polymer networks revert to closed-cell morphology at lower polymer loadings.

3.3 Electrolyte Characterization

3.3.1 Commercial Benchmarking

Following the optimization of the recipe towards simultaneously improved pore structure and mechanical properties, the porous polymer samples were freeze-dried and tested in both the dry and electrolyte-swollen states. The sample was mechanically tested using a custom puncture test set-up with 2mm tip diameter, then compared to commercial glass fiber and PP separator control samples (Figure 3.9). Compared to the 200 grams-force (gf) benchmark set by the separator industry, this polymer was able to achieve a puncture strength of 886 gf, far exceeding those of commercial PP and glass fiber separators.

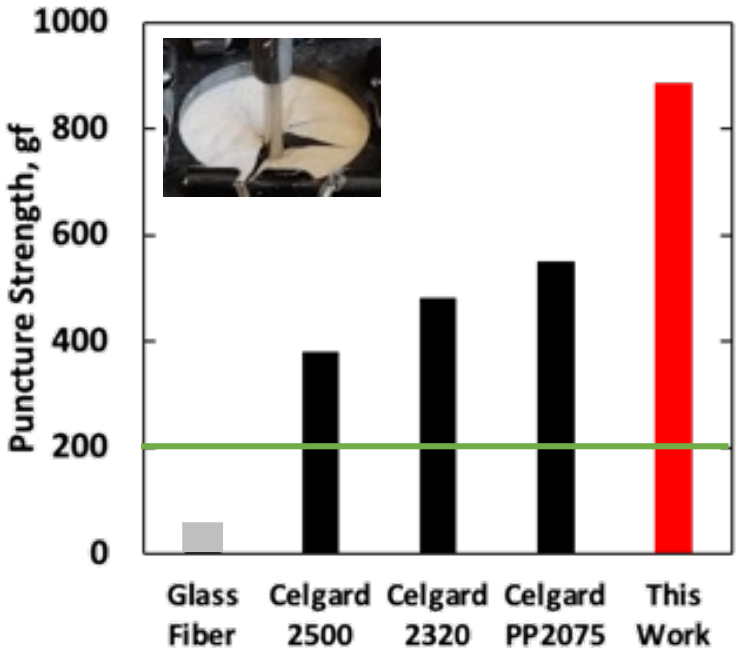

Figure 3.9 Puncture strength of our optimized porous polymer, commercial PP separators, and commercial glass fiber separator using 2 mm diameter tip. Inset image depicts the apparatus of a 3 cm x 3 cm polymer sample clamped within a holder with 2 cm diameter aperture.

Tensile tests were also conducted comparing our porous polymer to commercial PP and glass fiber (Figure 3.10); this work's porous polymer was able to achieve a tensile strength of 6 MPa, comparable to commercial PP separators, and a Young's modulus of 225 MPa, far exceeding those of both commercial PP and glass fiber separators (Figure 3.11).

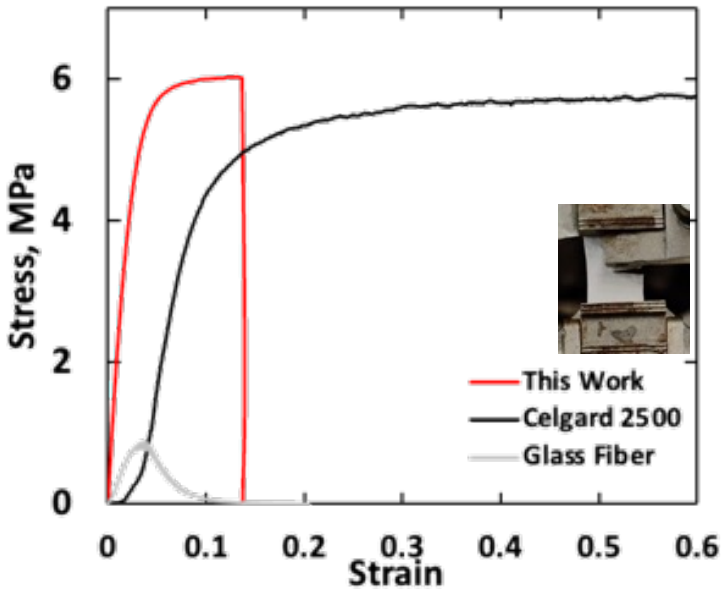

Figure 3.10 Tensile test of our optimized polymer, a commercial PP separator (along the transverse direction), and commercial glass fiber separator. Inset image depicts the gradual tensile failure of the PNIPAM polymer via slow propagation of a tear along the right side until complete failure.

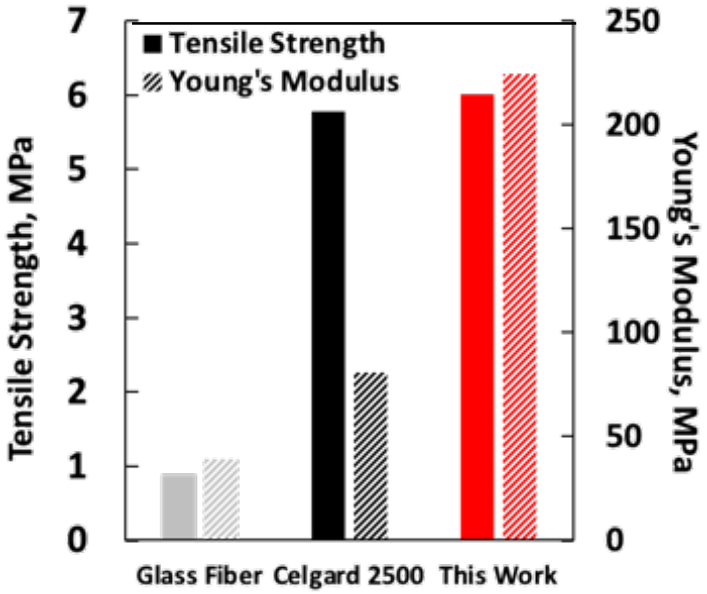

Figure 3.11 Compiled Tensile strength and Young's modulus values of our optimized polymer compared to commercial PP and glass fiber separators.

Electrochemical Impedance Spectroscopy was conducted to assess the ionic conductivities of commercial PP, commercial glass fiber, and our generated chemistry-impartial GPE in organic and aqueous electrolytes, benchmarked against the theoretical maximum liquid ionic conductivities (Figure 3.12)

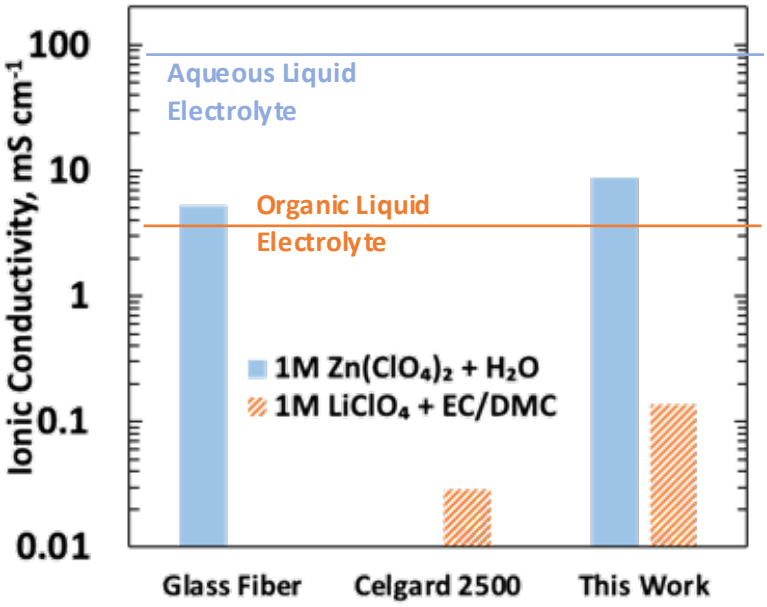

Figure 3.12 Ionic conductivity values calculated from electrical impedance spectroscopy results for our polymer and commercial PP and glass fiber separators, benchmarked against the pure organic and aqueous liquid electrolyte ionic conductivities.

3.3.2 Ionic Conductance

Electrochemical impedance spectroscopy (EIS) can non-destructively collect a large amout of valuable information describing the various interfacial phenomena occurring within the cells. Within a battery cell, various processes such as ion migration, charge transfer/de-solvation, and diffusion within the electrode are occurring simultaneously, each with their own corresponding characteristic frequency. EIS can probe each of those processes by inputting a voltage or current signal of specific frequency (Figure 3.13)

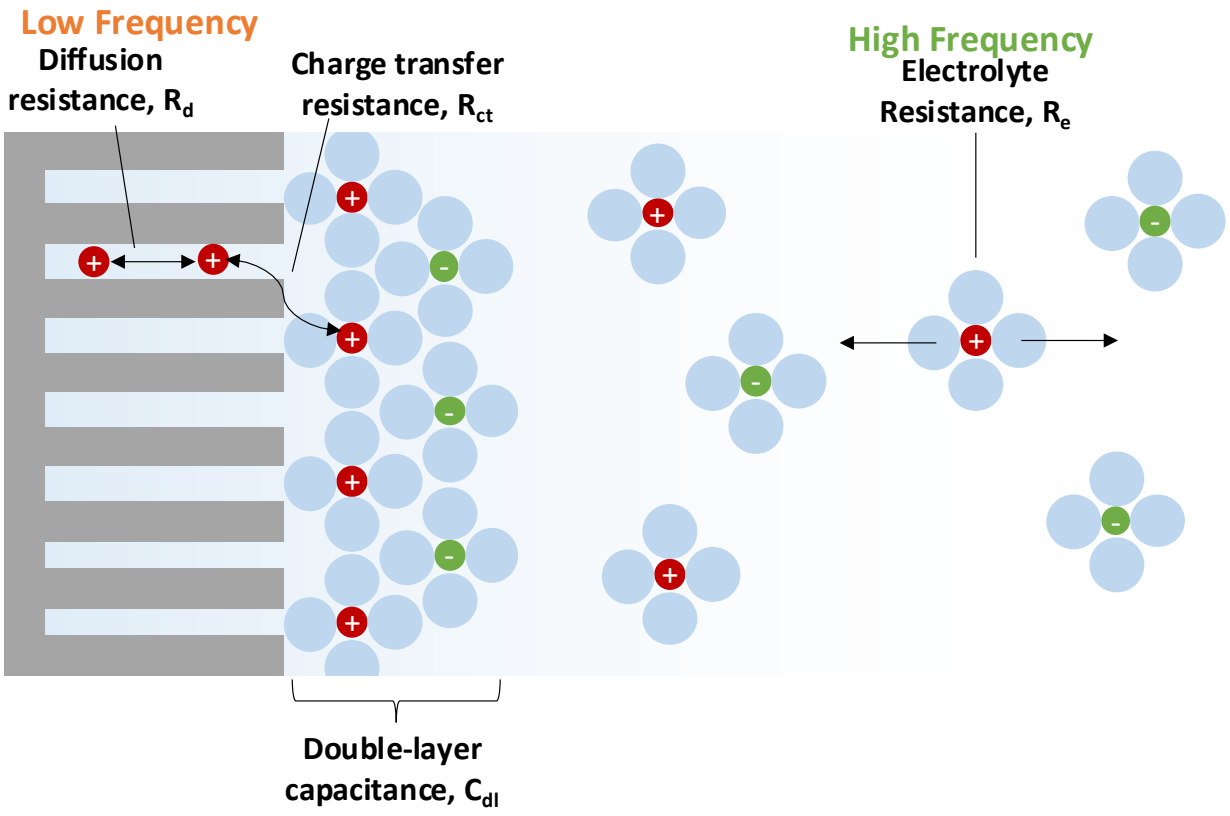

Figure 3.13 Overview of the various ion transport phenomena probed by electrochemical impedance spectroscopy, each corresponding to a different characteristic frequency.

The various ion interfacial phenomena can be modeled using equivalent circuits, the most common one being that depicted in Figure 3.14. Such a circuit can produce the general electrochemical impedance spectrum depicted in Figure 3.15, represented on a Nyquist plot where the x and y axes corresponding to the real and imaginary components of the impedance: the various internal resistances within the cell and their corresponding characteristic frequencies are outlined (Figure 3.15).

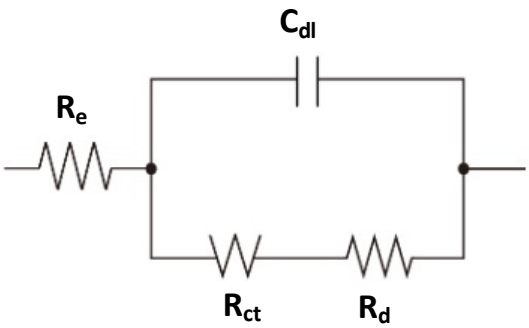

Figure 3.14 Equivalent circuit commonly used to represent each ion transport step from bulk electrolyte migration to interfacial and electrode interactions.

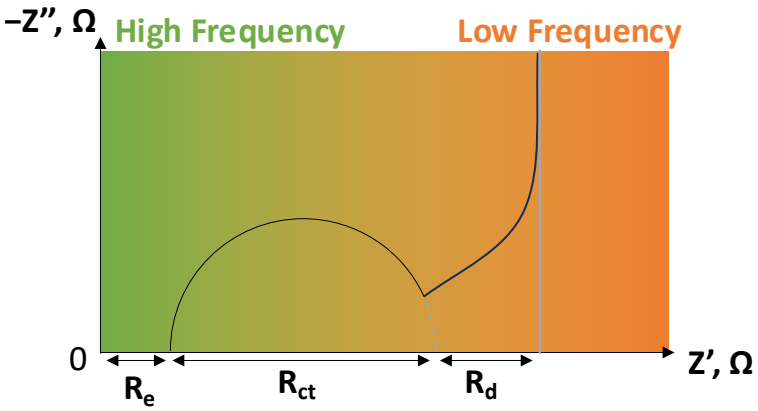

Figure 3.15 Generalized electrochemical impedance spectrum on a Nyquist plot, showing the individual resistances in a half-cell and their relative characteristic frequencies.

The ionic conductivity of the electrolyte can be obtained from such a technique, by measuring the electrolyte resistance, R_e, and inputting it into the following equation, where l is the sample thickness and A is the sample area:

$$\sigma = \frac{l}{R_e \times A}$$

Equation 17

The ionic conductivity is a geometry-independent material property describing the ease of ion transport throughout the material. Many groups have targeted increasing this property in novel GPE's in the hopes of achieving improving cell performance. While the ionic conductivity represents a valuable metric and a decent predictor of cell performance, it is incomplete. In a real cell, the ions must still travel across the cross-sectional thickness of the polymer electrolyte during charging and discharging. When this thickness is larger, it represents a larger total system resistance through which the ions must transport, corresponding to larger ohmic losses and worse cell performance. Not only does the increased resistance play a role, but the larger path length the ions must travel will also reduce the homogeneous ion transport. This is the reason why separator and electrolyte manufacturers are constantly targeting thinner form factors for high C-rate capabilities, but there lies a limit below which the risk of puncturing and shorting becomes too high.

Ionic conductivity does not paint a complete picture, we define the ionic conductance in Equation 18. The ionic conductance is also referred to as areal conductivity and is most utilized in the 2D materials field where material property of semi-conducting and conducting monolayers are investigated. In simple terms, the ionic conductance captures both the intrinsic ionic conductivity of the material as well as its thickness (Figure 3.16). This metric is more useful since, in addition to ionic conductivity, the thickness bears a direct effect on cell performance and not all synthesis techniques are compatible with generating the sub-20-μm thick samples that the industry demands for suitable cell performance.

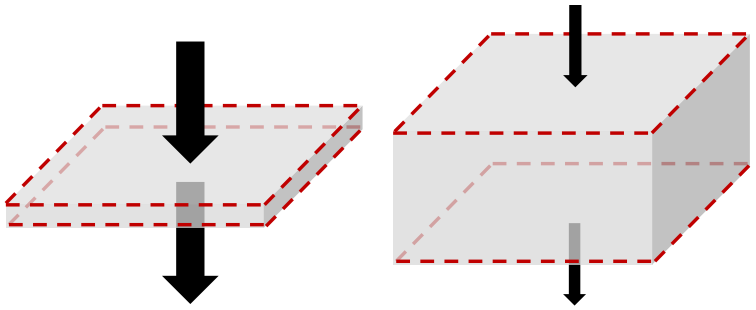

Figure 3.16 Schematic demonstrating the concept of ionic conductance, also referred to as areal conductance, for a specific material with differing thicknesses. While the more common ionic conductivity represents a geometry-independent material property describing the material's intrinsic ability to conduct ions, the ionic conductance represents the more relevant thickness-dependent ability to conduct ions through the material's thickness. It is generally not enough for electrolytes to carry a high ionic conductivity; they must also maintain a low cross-sectional thickness to reduce the total system resistance and decrease travel distance of the ions. Our GPE's areal conductance and tensile strength are benchmarked against other GPE systems in the literature **(**Figure 3.17).

$$\sigma_A[S\,m^{-2}] = \frac{\sigma}{l} = \frac{1}{A \times R}$$

Equation 18

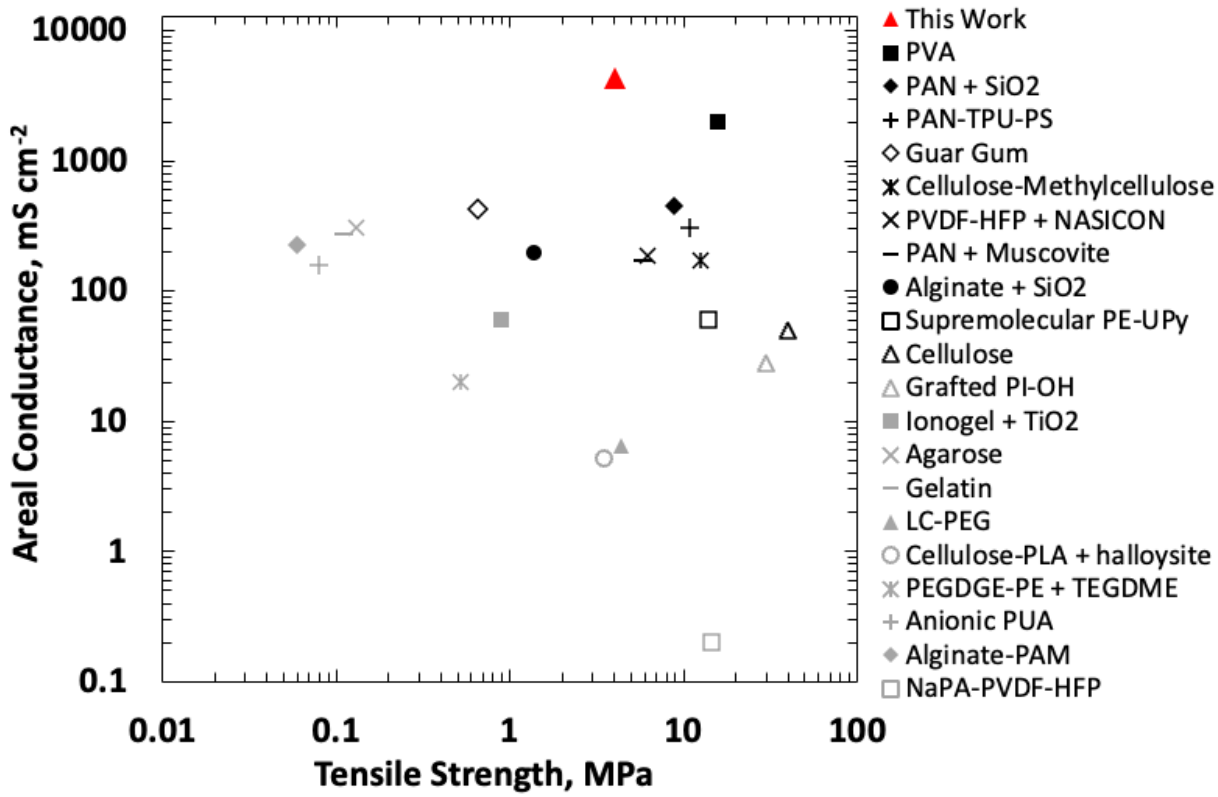

Figure 3.17 Ionic transport and mechanical performance of our optimized chemistry-impartial gel polymer electrolyte compared to state-of-the-art chemistry-specific gel polymer electrolytes.[77,101–119]

3.3.3 Electrochemical Performance and Rate Capabilities

Following the successful benchmarking of the mechanical and ionic conductivity properties against commercial separators and other state-of-the art GPE's, we generated two variant GPE's based on the same porous polymer scaffold: one swollen with aqueous electrolyte (1M $Zn(ClO_4)_2$) and the other swollen with organic EC/DMC-based electrolyte (1M $LiClO_4$). The aqueous variant was crimped into a Zinc-ion coin cell, composed of a Zn-metal anode and MnO_2 cathode. The organic variant was crimped into a Li-ion cell and Li-metal half-cell composed of LTO and Li anodes, respectively, and LFP cathodes. Rate capability tests were conducted on all three of these cells at C/10, C/5, C/2, 1C, 2C, 4C, and 6C charging and discharging (Figure 3.18). Our GPE was compared to glass fiber commercial separator in the Zn-ion cell and to Celgard 2500 PP separator in the Li-ion and Li-metal half cells. In the aqueous cells, our GPE performed comparably to glass fiber separators at high C rates and sustained much better capacity retention over 100 cycles (Figure 3.19). In the organic cells, our GPE outperformed commercial PP at all C rates. To confirm electrochemical stability, linear sweep voltammetry was performed showing that our GPE had comparable stability to PP (Figure 3.20).

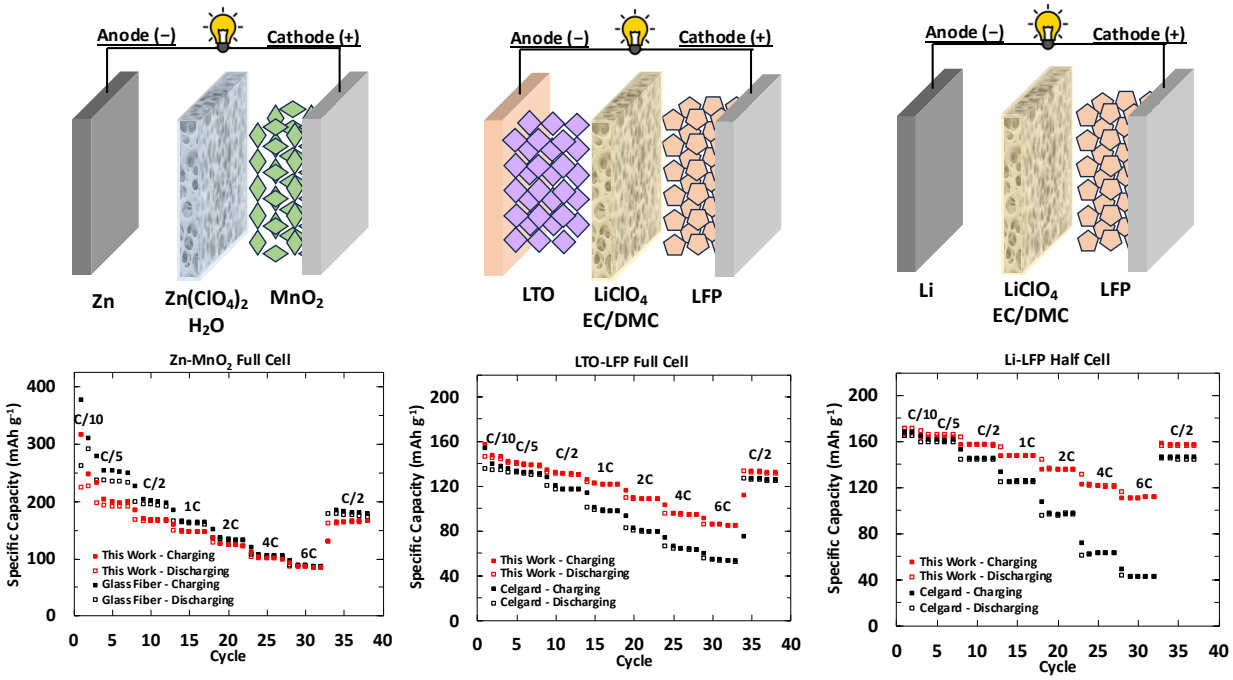

Figure 3.18 Schematic of our prepared Zn-ion, Li-ion, and Li-metal cells (top) and their corresponding rate performance tests benchmarked against commercial separators (bottom)

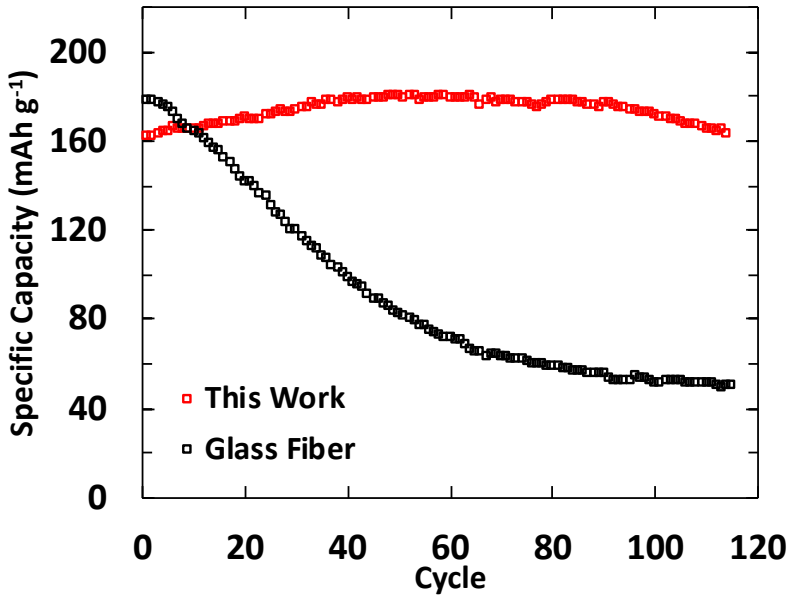

Figure 3.19 Cycle stability our optimized chemistry-neutral gel polymer electrolyte compared to that of commercial glass fiber separator. Both were swollen with 1M $Zn(ClO_4)_2$ aqueous solution and tested with a C-rate of C/2 in a Zn/MnO_2 cell.

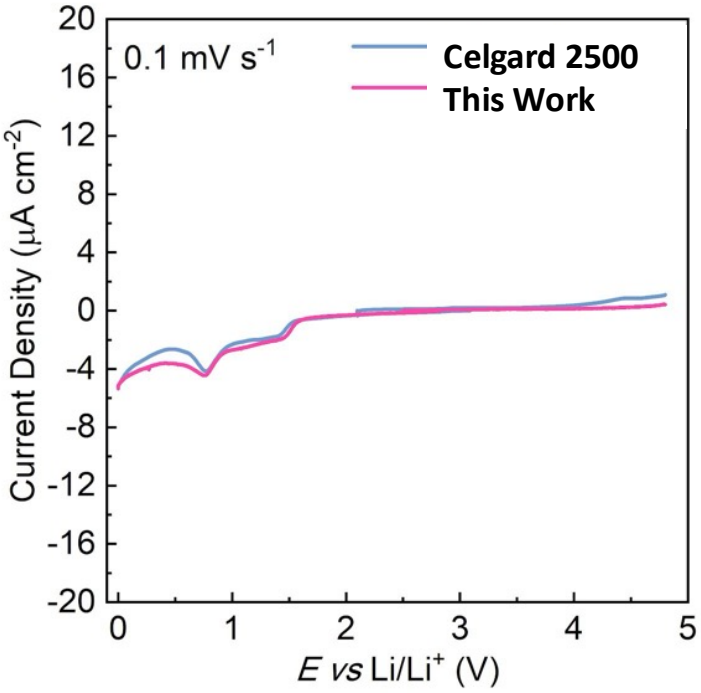

Figure 3.20 Linear sweep voltammetry test demonstrating the comparable electrochemical stability of our optimized gel polymer electrolyte and Celgard 2500 PP separator, both swollen with 1M LiClO4 EC/DMC electrolyte.

Chapter 4: Hydrogels for Soft Robot Voxel Assemblies with High Spatiotemporal Reconfigurability

4.1 Background

4.1.1 Soft Robotic Approaches

Practical soft robotic applications, ranging from basic bending and shortening primitives to complex reconfigurations, all require time-varying and local deformations of bulk hydrogels in order to approach the dexterity of soft organisms in performing tasks such as grasping and manipulation. [120,121] However, the responsive volume change of smart hydrogels is typically uniform. Two main approaches have been adopted by researchers to achieve nonuniform spatiotemporal deformation in hydrogels.[120] In the first approach, heterogeneous structures in the shape of sheets and rods are fabricated by patterning material domains using manufacturing techniques such as micro- and meso-patterning[122–127] and 3D printing.[128] Differing swelling properties of neighboring domains upon stimulation results in nonuniform strain fields in these structures, causing them to transform into a variety of complex shapes like coils and conical helices.[129,130] The range of compatible materials available for each domain, however, is often limited by practical fabrication constraints, such as ink viscosity for 3D printing.[128] Moreover, the geometry and material selected for each domain determine the shape transformations; these features cannot be changed after manufacturing, making on-demand reconfiguration infeasible.

The second approach toward achieving nonuniform spatiotemporal deformations uses an inhomogeneous or time-varying stimulus, such as patterns of structured light,[131] local irradiation by near-infrared light,[132] or localized electric fields.[133] In these methods, the hydrogel material itself is typically homogeneous, but the stimulus intensity varies across different regions, causing localized and time-varying deformations. These techniques, while suitable for on-demand shape reconfiguration, often require bulky external equipment, ultimately leading to challenges in mobile robot applications.

4.1.2 Nature's Strategy

Nature has adopted a hierarchical approach in addressing these challenges by using motor units as building blocks for heterogeneous muscle tissue demonstrating complex spatiotemporally reprogrammable deformations.[134,135] A motor unit consists of a motor neuron and the muscle fibers innervated by its axonal terminals.[136] It behaves as a stimuli-responsive building block, producing unidirectional deformation in response to electrical stimulus from the central nervous system (CNS). The variations in orientation[137] and response rate[138] of muscle fibers create the structural heterogeneity[139] required for nonuniform hard-coded deformations; the on-demand control over location and intensity of the electrical stimulus provides the spatiotemporal reprogrammability.[140–142]

4.2 Voxel Assembly

4.2.1 Design Principles

Inspired by nature's approach for achieving on-demand spatiotemporal deformations in muscle tissue, we introduce addressable and tunable building blocks that can be assembled to create heterogeneous hydrogel structures with “hard-coded” or “reprogrammable” shape change. These building blocks, herein referred to as soft voxel actuators (SVAs), are shown in Figure 4.1, left. The SVA units, consisting of a responsive hydrogel material and corresponding electrical connections, are inspired by the motor units of muscle tissue (Figure 4.1, right). The deformation of SVA units as a result of an electrical stimulus from a microcontroller unit (MCU) is analogous to the contraction of muscle fiber units in response to stimuli from the CNS. The selection of electrical stimuli as opposed to other types of stimuli is advantageous, since it enables addressing SVAs directly by small-footprint microcontrollers without the need for bulky equipment or human intervention.[143]

Two types of SVAs have been realized and are described herein: one without an embedded heater (referred to as SVA-I), and one with an embedded heater (referred to as SVA-II), as shown in Figure 4.2. Various combinations of SVA-I and SVA-II can be used for designing and fabricating heterogeneous assemblies. One possible combination uses SVA-I to create pre-programmed voxel assemblies. Based on the specific arrangement of SVA-I consisting of different swelling properties (mainly volume change ratio and rate), complex deformations can be demonstrated. These SVA assemblies deform in response to regular and repeated homogeneous temperature changes (such as the bulk heating and cooling of a water reservoir), generating motions without the need for an on-board energy source. It should be noted that hydrogels expand

and contract based on the diffusion of water into and out of their structure when the temperature is passed their critical transition temperature which is around 32 ºC in case of PNIPAM hydrogels. Therefore, all our experiments are performed in a water bath. Another combination of SVAs uses thick film surface mount (SMD) resistive elements with a resistance of 10 ohms as Joule heaters in SVA-II units to create time-varying and inhomogeneous temperature fields, resulting in on-demand dynamic deformations and real-time reconfigurability.

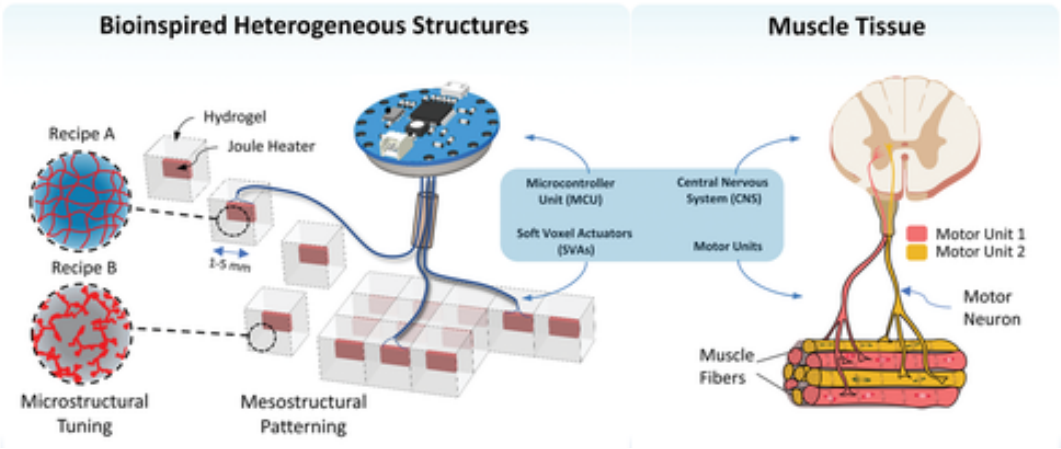

Figure 4.1 Illustration of bioinspired heterogeneous hydrogel structures composed of tunable and addressable voxels. A) soft voxel actuators (SVAs) are electrically addressable building blocks whose deformations can be controlled by a microcontroller unit (MCU). SVAs are analogous to motor units, consisting of a motor neuron and associated muscle fibers, which deform in response to electrical impulses from the CNS. The microstructure of the hydrogels used to make SVAs can be altered, resulting in tunable material properties.

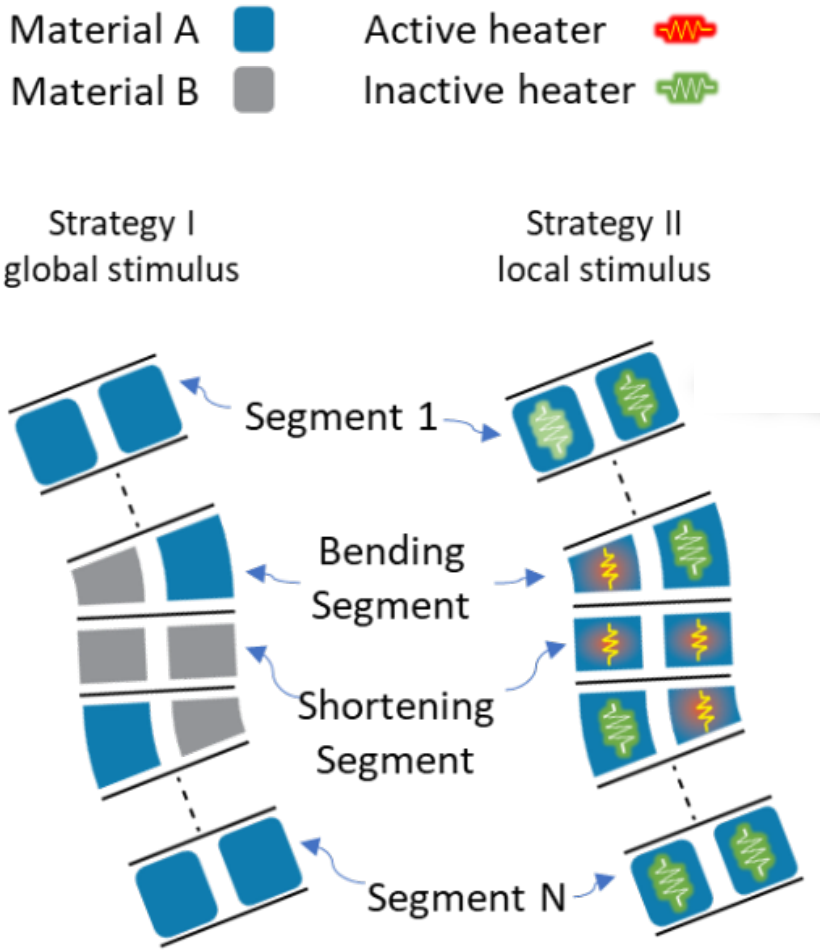

Figure 4.2 Pre-programmed and on-demand complex spatio-temporal actuation. SVAs without embedded Joule heaters (SVA-I) are used to create structures with hard-coded shape morphing that respond to a homogeneous temperature field acting globally on the entire structure through the surrounding water bath. ii) SVAs with embedded heaters (SVA-II) are used to create structures with on-demand shape morphing by forming an inhomogeneous temperature field throughout the structure.

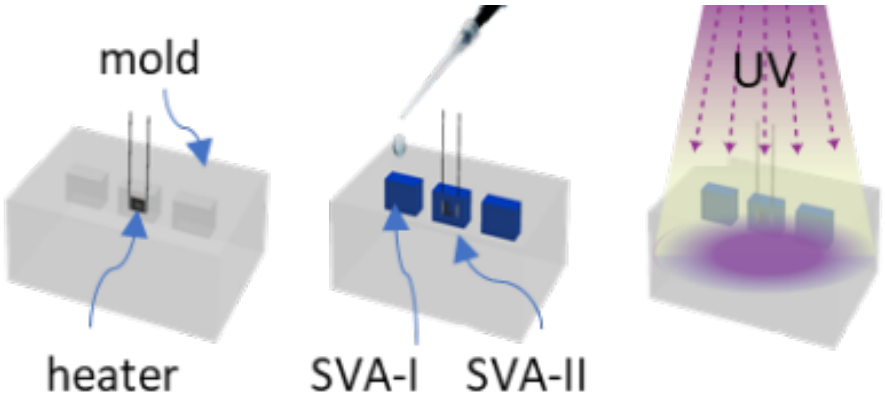

Figure 4.3 Fabrication method of stimuli-responsive voxels with embedded heaters. The Joule heaters are placed within a PDMS mold with fixed position and geometry. The molds are filled with the desired PNIPAM precursor solution, followed by UV curing for 15 seconds.

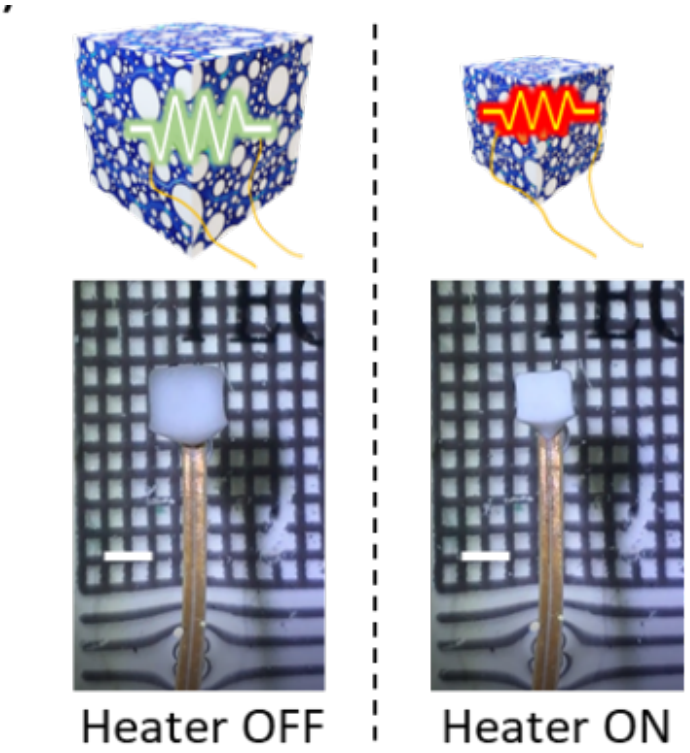

Figure 4.4 Schematic (top) and photographs (bottom) of individual heater-embedded voxels composed of temperature-responsive PNIPAM. When the heater is on, the voxel shrinks due to temperature elevation above the PNIPAM's LCST. Scale bar corresponds to 1 cm.

4.2.2 Hydrogel Stimuli-Responsive and Mechanical Tunability

The ability to select from a broad range of material properties for SVA fabrication can expand the design space of resulting heterogeneous structures. Therefore, a synthesis method that can tune the ratio and rate of hydrogel volume change is required. A variety of physical and chemical methods have been explored to alter the swelling properties of hydrogels.[20,144] These methods are limited by factors such as the narrow range of achievable swelling properties,[145,146] large trade-offs in mechanical properties,[147,148] long processing times,[122,149] and a need for careful control of synthesis conditions such as temperature[150] and precursor additives.[22]

We take advantage of PNIPAM's cononsolvency, a property of reduced solvation in a mixture of two solvents due to a delicate balance between polymer–solvent and solvent–solvent interactions.[58] Employing a water and dimethyl sulfoxide (DMSO) mixed solvent in the PNIPAM hydrogel precursor solution, followed by rapid photopolymerization to induce interconnected open pores, significantly enhanced the rate of water transport into and out of the hydrogel matrix and thus the actuation speed. The microstructure of the gel is altered by changing the water volume fraction (φ_w) in the mixed water/DMSO solvent. The SVA swelling rate and displacement, which are directly related to its hydrogel microstructure, are therefore tuned by merely adjusting φ_w. Polymerization solvent composition is known to affect the swelling properties of the synthesized PNIPAM hydrogels.[70,151–154]

The combination of the mixed solvent method with a fast 15 s photopolymerization step is critical for inducing and fixing local aggregations of polymer chains in place, resulting in PNIPAM hydrogels with open pore structures (Figure 4.5Ai). Such open pore structures exhibit significantly enhanced rates of thermoresponsive volume change in both heating and cooling phases, compared to conventional hours-long mixed solvent thermopolymerization methods (control experiment), in which the precursors are constantly diffusing toward a homogeneous molecular equilibrium throughout the duration of the reaction, leading to a less interconnected pore structure with thicker pore walls (Figure 4.5Aii). To ensure a valid comparison, the recipe for a representative thermopolymerized control hydrogel was carefully tuned using the initiator concentration while leaving all other components of the precursor solution unchanged, choosing a reaction time such that the conversion and water content match those of the photopolymerized hydrogel.

It is readily observed that with equivalent water content, reaction conversion, and reaction solvent composition, the thermopolymerized hydrogel de-swells as fast as the photopolymerized hydrogel (Figure 4.5Bi) and the two reach nearly identical shrunken volumes. However the reswelling speed of the thermopolymerized control sample is ≈25 times slower than the photopolymerized sample, which can be attributed to the lower observable tortuosity present in the photopolymerized sample (Figure 4.5Bii). The Young's Modulus of the thermopolymerized hydrogel is approximately ten times higher than that of the photopolymerized one.

The effect of varying φ_w on the hydrogel microstructure has been investigated by scanning electron microscopy (SEM), as shown in Figure 4.5C. Six hydrogels consisting of various $\varphi_w$were

synthesized; they are each represented by a character code ranging from HG00 (representing a hydrogel with $\varphi_w = 0.0$) to HG05 (representing a hydrogel with $\varphi_w = 0.5$). Distinct changes in the microstructure can be observed as a function of φ_w, which impacts a variety of other material properties. When φ_w is increased from 0.0 to 0.2, pore size decreases and the pore wall surface begins to change from smooth to rough. We define $\varphi_w = 0.2$ as a critical water volume fraction, at which the microstructure of the gel starts to change from a closed-pore to an open-pore structure. The changes in hydrogel microstructure play a role in the dynamic response of SVAs. The linear displacement generated by a SVA unit is measured using a vision-based test setup. Figure 4.5D plots the time evolution of the displacement (*D*) of SVA units with different values of φ_w as each SVA's embedded heater is turned on for 60 s and then turned off for 60 s. The displacement over time of the hydrogel made with $\varphi_w = 0.0$ is included as the basis for comparison across all tests. The negative displacement observed is because the SVAs initially expand instead of contract as the heater is turned on which might be due to water slightly expanding and vaporizing. Two performance criteria for the SVA units, deformation rate (*DR*) and maximum displacement (*MD*), are extracted from the data in Figure 4.5D and are shown in Figure 4.5E and Figure 4.5F respectively. During both heating and cooling, *DR* is small for $\varphi_w < 0.2$. At $\varphi_w = 0.2$, the *DR* during heating is more than 36 times the *DR* during cooling. As a result, fast and large deformations are observed during the 60 s of heating, and almost no deformation is observed during the 60 s of cooling. Highest *DR* (in both heating and cooling) occurs in gels with $\varphi_w = 0.3$, while *MD* peaks at $\varphi_w = 0.2$ and decrease thereafter. In addition to swelling properties, other mechanical properties such as Young's modulus and force produced by the SVAs can also be tuned by adjusting φ_w.

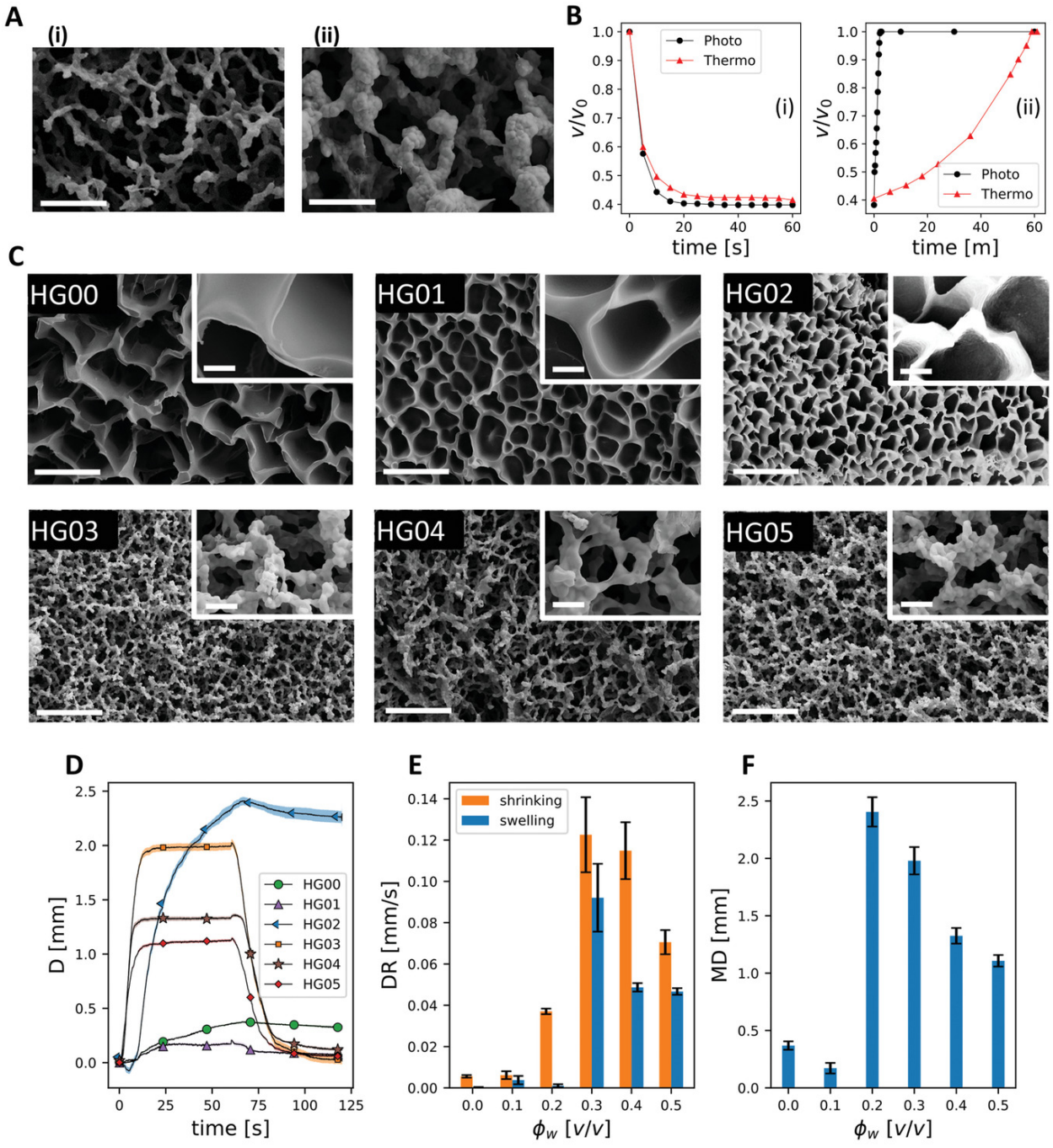

Figure 4.5 Tunable material properties using mixed solvent photopolymerization. a) SEM images of photopolymerized (i) and thermopolymerized (ii) hydrogels synthesized in water volume fraction $\varphi_w = 0.27$ (scale bar = 5 μm). B) Deswelling (i) and swelling (ii) rates of photopolymerized and thermopolymerized hydrogels synthesized in water volume fraction $\varphi_w = 0.27$. C) SEM

images showing the effect of φ_w on pore structure of the photopolymerized PNIPAM hydrogel (scale bars 10 and 1 μm for low and high magnification, respectively). D) Displacement (*D*) over time generated by SVA-II units with different values of φ_w under a 1 *gf* load, as measured by the setup) Displacement rate (*DR*) and maximum displacement (*MD*) of SVA-II units as a function of φ_w, (extracted from (B)).

4.3 Soft Robotic Actuation

4.3.1 Pre-programmed actuation with pre-arranged voxels

A variety of heterogeneous structures can be produced that transform into different configurations, depending on their hard-coded material domains, as shown in Figure 4.6. As a first example, a beam with only two material domains is fabricated from HG00 and HG02 hydrogels (Figure 4.6Ai). At 20 °C, the beam is in its equilibrium position. As the temperature increases to 45 °C, the HG02 hydrogel shrinks more than HG00 (from Figure 4.5E and Figure 4.5F, both *MD* and *DR* are higher for HG02), which results in a stress mismatch. To balance these stresses, the beam bends into a circular shape. We will henceforth refer to this structure as a "gripper". A second example uses HG00 and HG02 hydrogels again, but this time with 8 material domains, as shown in Figure 4.6Aii-iv. The beams in these figures consist of different arrangements of HG00 and HG02 voxels, and as a result exhibit different deformations when subjected to a homogeneous temperature change in the surrounding water from 20 to 45 °C.

Patterning material domains can be used to leverage the shape transformations into unique functions tied to structural heterogeneity. To demonstrate this structure–function relationship, two

different structures, Str-I and Str-II, are made with different combinations of HG00, HG02, and HG03, as shown in Figure Figure 4.6B. These structures represent a combination of the structures in Figure 4.6Ai-ii. In response to a global cyclic temperature change from 20 to 45 °C and back to 20 °C, these structures are observed to bend toward an object, grasp it (by wrapping around it), and transport it to another location (Figure 4.6B). The geometric configuration of material domains in both structures are the same. However, the "gripper" portion of Str-I is a combination of HG00/HG03 domains, whereas in Str-II it is a combination of HG00/HG02 domains. As a result of this minor material difference, the object grasped by Str-I and Str-II moves along different trajectories, as seen in Figure 4.6C, despite an identical set of initial conditions.

Due to the high *DR* of HG03 during the cooling phase (Figure 4.5E), the gripper in Str-I opens and the object is released in the early stages of the cooling phase. The gripper in Str-II, on the other hand, does not open at the same time as Str-I and continues to hold the object throughout its cooling phase; this can be attributed to the lower *DR* of the HG02 layer compared to HG03. To illustrate these differences, the *x* and *y* coordinates of the object over time are plotted in Figure 4.6D, and the time when the object is released by each structure is indicated. Achieving inhomogeneous deformations in response to a homogeneous global stimulus using structures with hard-coded deformations as described simplifies the system and eliminates the need for on-board power sources.

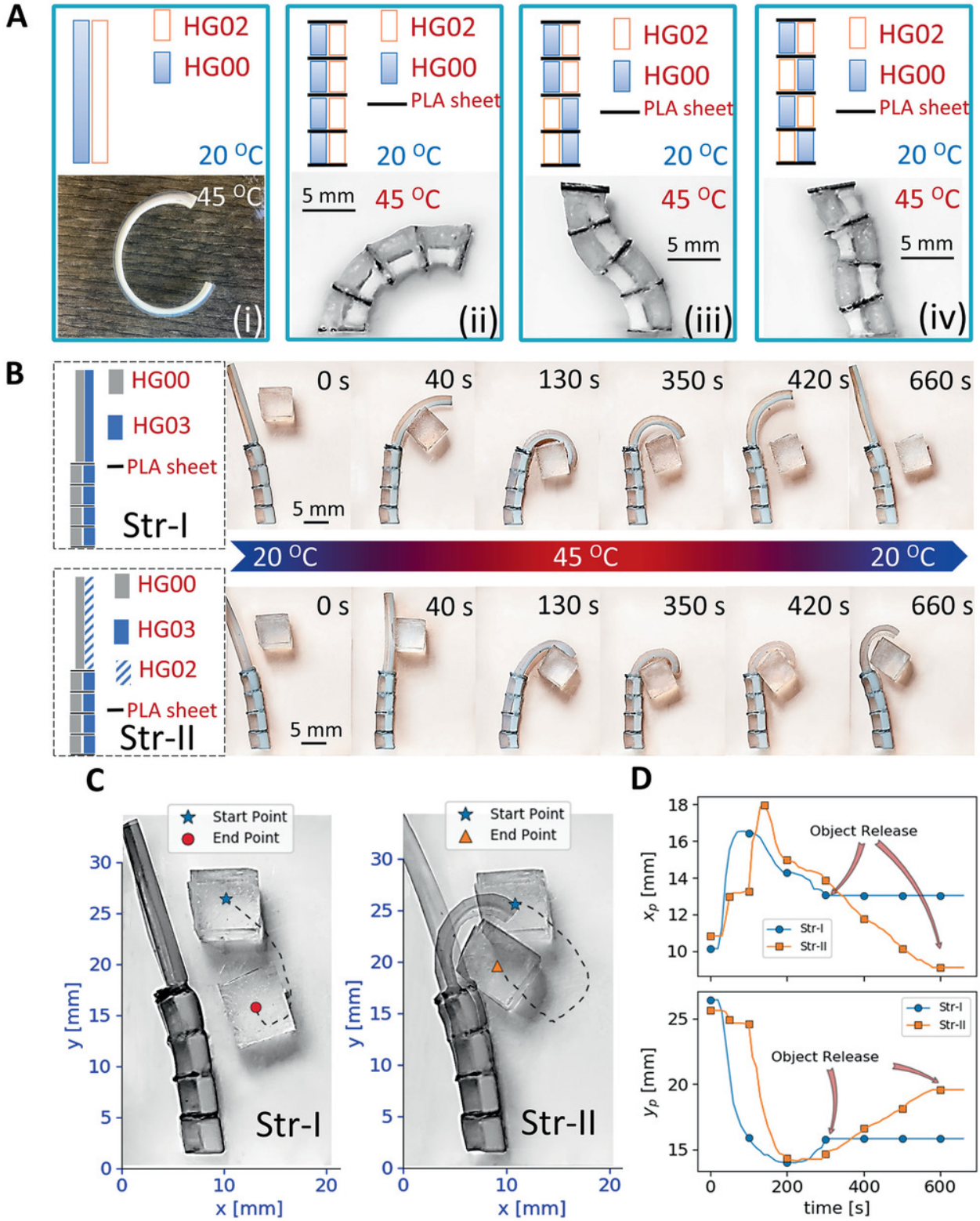
A
HG02
HG00
20 °C
45 °C
(i)
PLA sheet
5 mm
(ii)
(iii)
(iv)
B
HG03
Str-I
0 s
40 s
130 s
350 s
420 s
660 s
20 °C
45 °C
20 °C
HG02
Str-II
C
Start Point
End Point
y [mm]
x [mm]
D
Object Release
x_p [mm]
y_p [mm]
time [s]

Figure 4.6 Realization of structural inhomogeneity through patterning of hydrogels with different swelling properties. A) i) A two-material, two-region structure can almost bend into a circle when the surrounding water bath temperature is raised above the transition temperature of PNIPAM hydrogel (32 °C) ii–iv) Increasing the number of material domains in the structure enables it to achieve more diverse shapes. When the surrounding water bath temperature is increased, each structure reconfigures into a different shape, depending on its arrangement of SVA-I units. B) Hybrid structures comprised of substructures with the SVA arrangements in (A-i,ii) are capable of manipulating objects. The material distribution in two example structures, denoted by Str-I and Str-II, is shown in the schematic on the far left. The snapshots display the configurations of the two structures over time as the global water bath temperature is increased and then decreased. C) Image showing the start position, end position, and trajectory of the object manipulated by Str-I (left) and Str-II (right). D) Time evolution of the x and y coordinates of the manipulated object's center of mass. Str-I releases the object at $t = 300$ s, while Str-II releases it at $t = 600$ s, demonstrating the versatility of the voxel-based assembly approach to creating heterogeneous structures with diverse functions.

4.3.2 On-demand actuation with individually addressable voxels

For applications in dynamic, unstructured environments, such as underwater robotic exploration, it is less useful to pre-program complex trajectories into a structure since global stimulus control is not always feasible. To enable on-demand thermoresponsive shape morphing in these conditions, SVA-II units may be employed. The 40 × 11 × 5 mm structure shown in Figure 4.7 was assembled using 16 SVA-II units. These SVAs are made of HG03, which exhibits the highest *DR* observed across all recipes (Figure 4.5E). The first example of on-demand shape

morphing is illustrated in Figure 4.5Bi, in which the structure morphs into an “S” shape and a “reverse S” shape when particular SVAs are actuated via commands from a microcontroller. A second example of on-demand shape morphing is illustrated in Figure 4.5Bii; it highlights how the curvature of a structure may be varied as a function of the voltage supplied to the SVA-II units.

Moving from static to dynamic on-demand shape changes requires time-varying activation of SVAs. As demonstrated in Figure 4.7C, the choice of SVA actuation pattern can influence the end-effector trajectory of a structure. In this experiment, SVAs 1 thorough 8 are activated according to patterns denoted by P1 and P2. Each SVA is activated with maximum voltage (3.7 V) for 15 s before the next SVA is activated, as shown in Figure 4.7C.

While complex motion of SVA-II-based structures may be achieved using simple on (3.7 V) and off (0 V) activation signals, as discussed, intermediate voltages may also be applied to further enhance the complexity of shape change in soft heterogeneous structures. To demonstrate this, phase-shifted sinusoidal voltages were used as activation signals to generate longitudinal traveling waves in the structure. A pair of SVAs (comprising a SVA on the left and its adjacent SVA on the right) are activated using the same sinusoidal signal; SVAs 4 and 12 were not activated, to serve as a geometric reference point. The sinusoidal voltages applied to every SVA pair were out of phase with the voltages applied to its nearest active SVA pair. As an example, sinusoidal signals for four SVA pairs are shown in Figure 4.7D. A contraction wave was formed as a result of this input signal pattern and traveled along the length of the structure, as illustrated

in Figure 4.7E. Every point on the structure oscillates in a sinusoidal manner as the wave passes through it. The midpoint of the inactive SVA pair, which is highlighted by a yellow square in Figure 4.7E, is shown as a reference point on the structure. Additionally, by sending the sinusoidal signals to SVAs located on only one side of the structure, for example SVAs 1 through 8, transverse traveling waves were generated in the structure. The ability to control the trajectory of the structure's end-effector, as shown in Figure 4.7C, is essential to successful functioning of the device in unstructured environments, in which working conditions may change during operation. As depicted in Figure 4.7F, time-sequenced switching of selected SVA-II units within the structure makes it possible to accomplish various robotic tasks such as collision avoidance (top row) and object transport (bottom row). The trajectory of the end point p and the angle θ of the end plate over time (p and θ are defined in Figure 4.7A) during each of these two tasks is displayed in Figure 4.7G. The on-demand control of reorientation and translation of the end-effector made it possible to complete these two tasks, indicating that highly redundant time-varying deformations in heterogeneous structures are achievable using individually addressable SVA-II units.

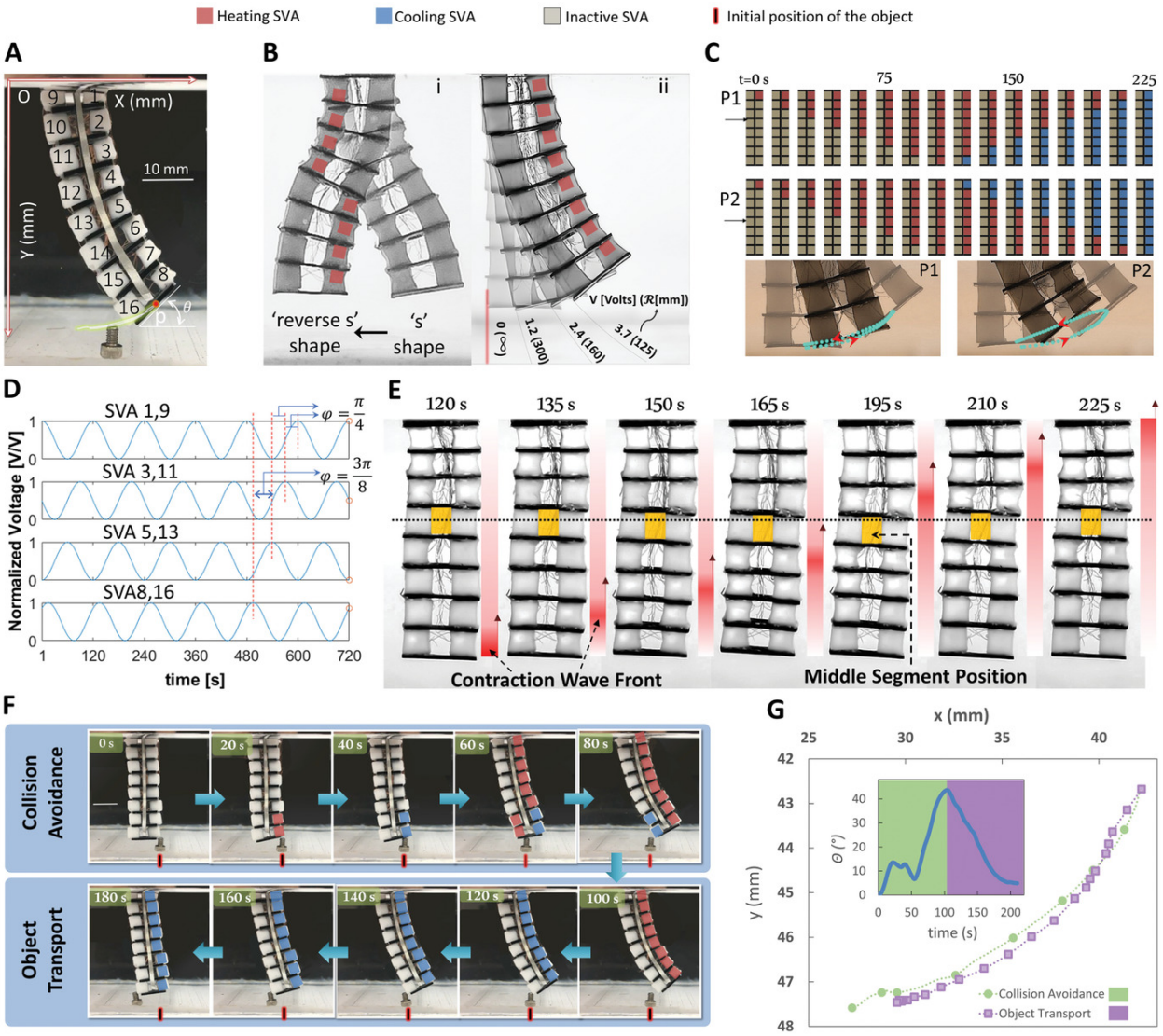

Figure 4.7 A miniature heterogeneous structure consisting of 16 addressable SVA-II units. A) SVA numbering scheme and the coordinate system used to measure the position of the point *p* and the angle θ of the end plate. B) On-demand shape morphing of the structure. i) The structure morphs from an "S" shape to a "reverse S" shape when particular SVAs are activated. ii) The structure's radius of curvature (***R***) depends on the activation voltage (*V*) applied to SVAs 1–8. C) Dynamic shape changes are implemented by sequentially activating SVAs. In this case, SVAs 1 through 8 are activated according to the patterns labeled P1 and P2. The trajectory followed by the tip of the structure (shown at the bottom) can thus be adjusted on-demand. Normalized sinusoidal

voltages used to create longitudinal traveling waves in the structure. The voltages applied to 8 of the 16 SVAs are shown here. The SVAs are activated in pairs, and the voltage applied to each SVA pair is out of phase with respect to the voltage applied to the next active pair. E) The longitudinal traveling wave as it propagates through the structure. One SVA pair, indicated by the yellow square, is kept inactive to serve as a reference point. F) Example usage of heterogeneous structures with on-demand control of deformation. The structure can avoid collisions with objects or transport them, depending on the sequence of voltage commands from the microcontroller unit. G) Trajectory of the point *p* on the tip of the structure as it first avoids and then transports the object. The inset shows the angle θ of the end plate as a function of time.

Chapter 5: Artificial Phototropism Towards Resolving Oblique Incidence Energy Loss

5.1 Background

5.1.1 Natural Systems and Phototropism

Many living organisms present the unique capability of directionally moving towards sources of certain environmental stimuli. For example, cells and bacteria can migrate towards sources of chemical gradients, known as chemotaxis, for food (for example, glucose), fertilization (for example, sperm moving towards the egg) or immune functions.[155] Plants can self-orient to face light sources perpendicularly, known as phototropism, for energy harvesting and reproduction. All their direction of locomotion is strictly determined by the direction of an environmental stimulus, namely, tropistic movement, in contrast to nastic movement, which is a non-directional response to stimuli and simply determined by organism anatomy.[156] In tropistic movement, organisms not only sense and respond to the stimuli positions, but also spontaneously and constantly adjust their movements to tightly follow the signal directions. This presents the intelligence of self-regulation via the feedback control inherent in the dynamic interactions between their bodies and the stimulus.

Nature has already found a solution to OEL: phototropism, the self-regulated mechanism of self-orientation towards sunlight, is developed by many plants as a strategy to recover the oblique-incidence energy-density loss (OEL), the input power density reduction when emissive energy projects on a surface obliquely. The mechanism is driven by the migration of the growth

hormone, auxin, to the non-illuminated side of the plant stem, promoting local cell elongation and growth. The local cell growth results in the plant stem towards sunlight, enabling perpendicular illumination of sunlight on the adjacent leaves. Figure 5.1 demonstrates this mechanism visually.

The energy harvesting loss from OEL can be enormous when the incident angle is large (for example, 75% loss at 75° incidence). By maintaining normal incidence, sunflowers raise the temperature of floral discs to attract more pollinators with warmth and show an effective recovery of the input loss caused by oblique illumination if no phototropism was present.[157]

It should be noted that natural phototropism is not reversible because cell growth and elongation are permanent. Adult plants therefore lose the ability to track sunlight at a certain age due to genetic limits. **It is therefore highly desirable to engineer a stimuli-responsive smart material that that mimics the sunflower's phototropism with the added benefit of reversibility for energy harvesting applications.**

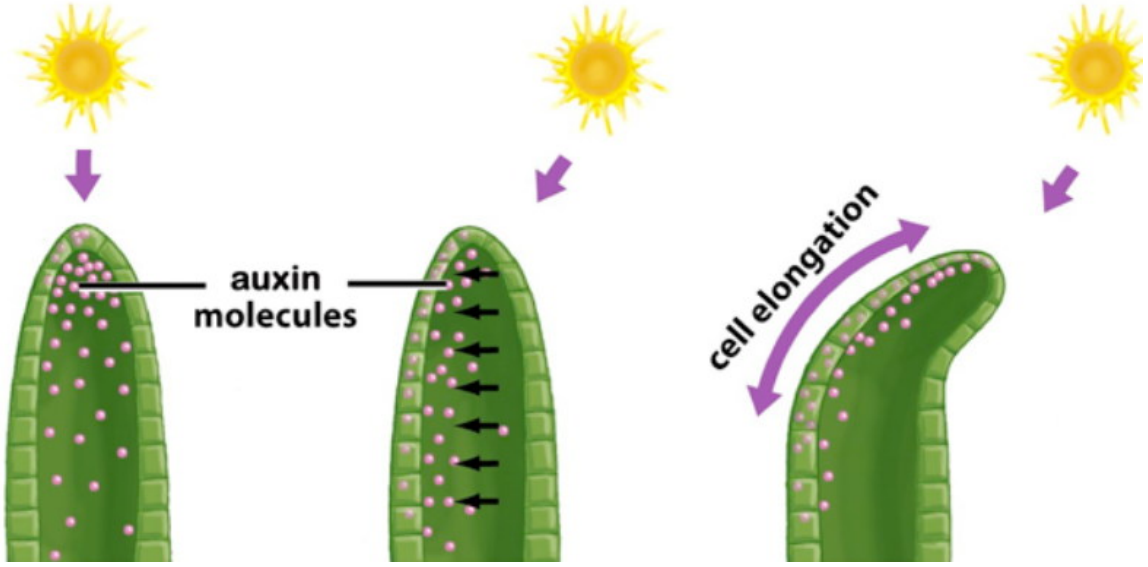

Figure 5.1 Schematic of natural photototropism in plan stems. The mechanism is governed by the migration of the growth hormone, auxin, towards the non-illuminated side and promoting accelerated cell growth locally.

5.1.2 Previous Approaches

Given the immense benefits of tracking, significant efforts have gone into programming and designing effective controls systems that can help orient solar harvesters towards normal incidence;[158] however, there has **yet to be a demonstrated case of a homogeneous smart material which can intrinsically and autonomously self-orient towards sunlight**. In other words, **all tracking schemes have been exclusively through electronic controls systems** and not through smart materials design. Such a smart materials system can significantly cut down on costs of manufacturing of controls systems and save physical space that servo motors and actuators typically occupy. Current state-of-the-art photoactuations remain primarily nastic,[159–163] unable to sense, track and harvest the emissive energy from varying incident directions self-adaptively.

5.2 Artificial Phototropism Our Approach: Smart material feedback loop

5.2.1 Design Principle

The objective is to address the oblique-incidence energy loss issue, potentially recovering more than 50% of lost power at highly oblique incident angles, by extending the concept of phototropism to synthetic stimuli-responsive material systems. In doing so, we also aim to control the material microstructure to enable the high diffusivity required by those applications.

Artificial phototropism, if realized, may provide an efficient solution to overcome this universal OEL issue faced by almost all existing optical and electromagnetic devices.[164–167] As a bioinspired concept illustrated in Figure 5.2, when a surface is covered with sunflower-like pillars that can bend towards the light source and maintain normal incidence, the original maximum power density ($P_{max} = P_0$) can be restored. The capability to harness tropistic behavior autonomously, without external instruction and power supply (for example, via electromechanically programmed systems), would enable highly efficient energy-harvesting platforms that can adapt autonomously to complex ambient environments.

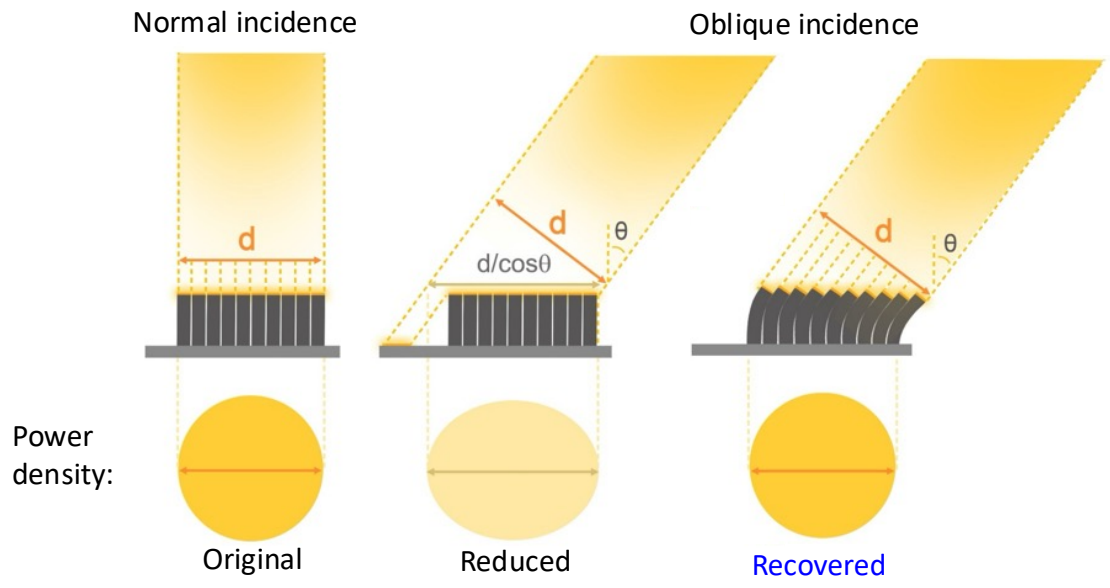

Figure 5.2 The concept of OEL recovery by phototropism. The OEL from P_{max} under the normal incidence (left) to $P_\theta = P_{max}\cos\theta$ under an oblique incidence at a θ_{zenith} angle ($P_{max} = P_\theta$ ($\theta = 0°$)) suffered by a conventional non-phototropic surface (middle) can be fully recovered by a surface covered with a phototropic array (right).

To mimic natural phototropism, an artificial system must be capable of the following three key functions: omnidirectional bending, active sensing, and autonomous self-correction. Omnidirectional bending allows for the artificial phototropic system to track the light source regardless of the time of day, season, or geographic location. It is therefore necessary to design a system which can bend in both zenith and azimuth angles (Figure 5.3). The cylindrical shape of the proposed artificial phototropic system is inspired by the natural 0plant stem. To achieve active sensing, we embedded a broadband photothermal absorber in the thermo-responsive hydrogel to create a photothermally-responsive material with volumetric shrinking on the illuminated faces (Figure 5.4). For self-correction, the system must have an embedded feedback loop. This can be

achieved with a cylindrical shape with fast photothermal volumetric change. Overshooting and undershooting scenarios can always be corrected with the built-in feedback loop caused by the directional lighting (Figure 5.5). At the equilibrium state, the tip of the pillar faces the light source. Additionally, there is the practical requirement that the photothermally responsive material must respond fast enough to track the sun as it moves across the sky.

Plants track light through photoreceptors in their stems that detect the incident light and lead to cell elongation on the shaded side, due to a distribution gradient of a growth factor (for example, auxin) between the illuminated and the shaded side.[157] To mimic the biological asymmetric growth, we leverage the capabilities of reversibly photothermoresponsive soft materials that shrink on illumination and adopt the symmetric stem-like cylindrical pillar shape for the device design. The design implements a thermoresponsive hydrogel, poly(*N*-isopropylacrylamide) (PNIPAM) with homogeneously distributed reduced graphene oxide (rGO), which simultaneously act as photoreceptors and photothermal converters. Like a stem, these pillars bend towards stimuli omnidirectionally (Figure 5.3 and Figure 5.4) due to the asymmetric deformation between the illuminated high-temperature region and the shaded low-temperature region. This design presents a versatile platform that can be constructed using almost any reversibly photoresponsive soft materials, for example, hydrogels,[159,168–172] liquid crystal elastomers (LCEs),[173–175] and azobenzene/spiropyran-based polymers.[161,176]

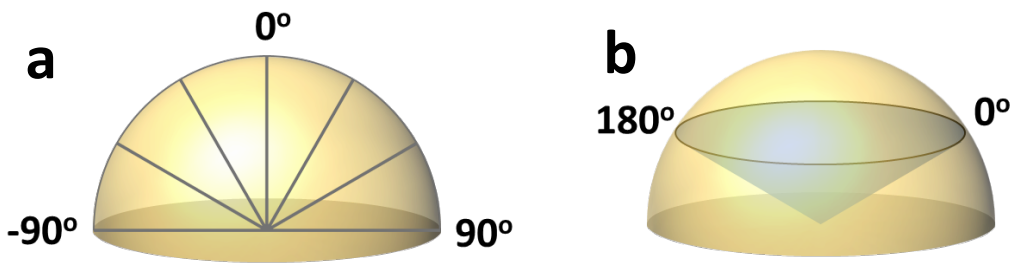

Figure 5.3 (a) Zenith and (b) azimuthal angle directions.

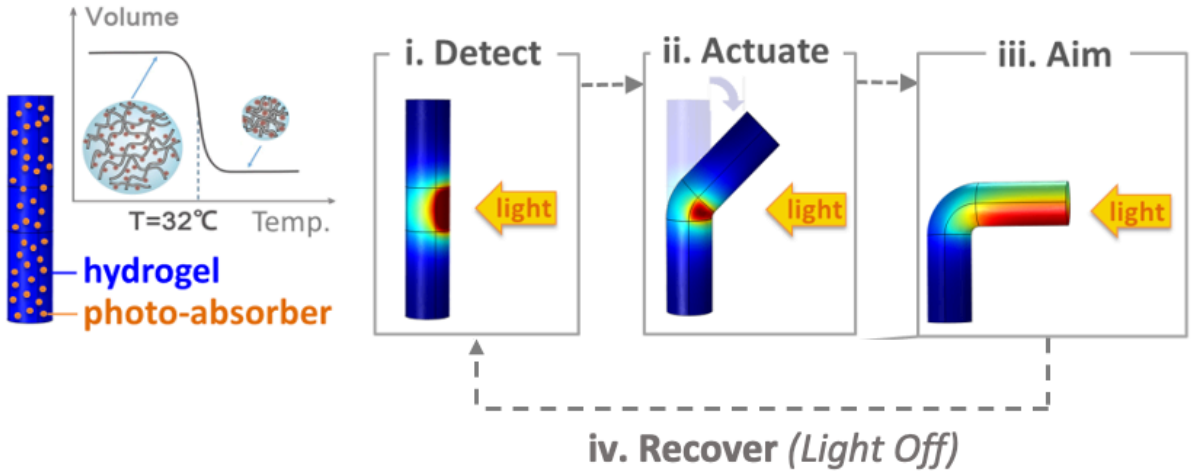

Figure 5.4 Mechanism for active sensing of light direction from a PNIPAM pillar with homogeneously dispersed photoabsorber.

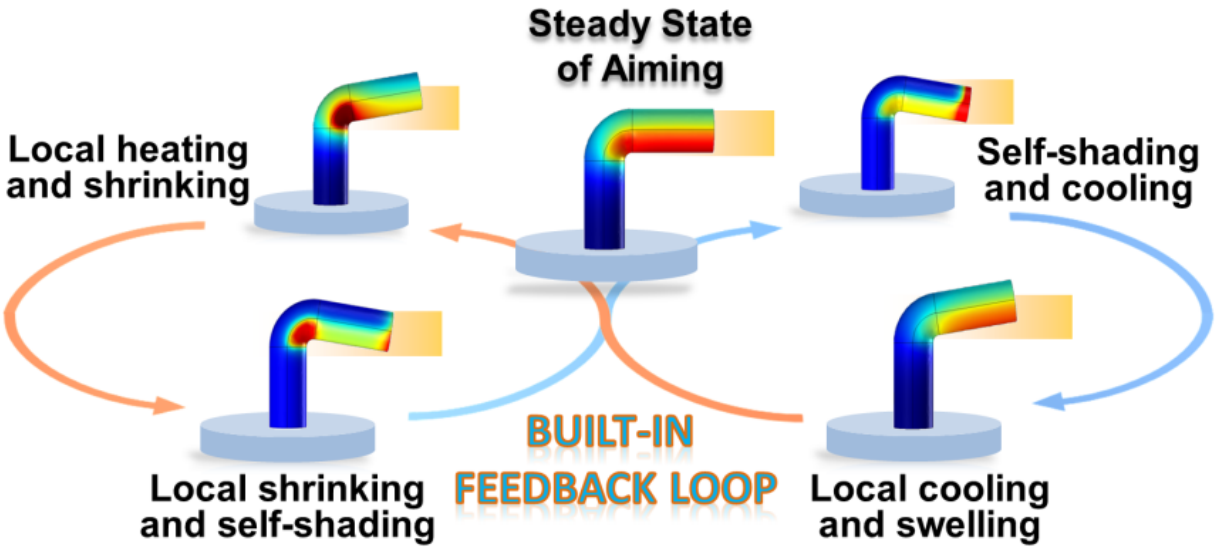

Figure 5.5 The equilibrium state of aiming is regulated by a built-in negative feedback loop with self-blocking capability.

5.2.2 Fabrication Method

As depicted in Figure 5.6, 0.3 wt% GO was added to the PNIPAM precursor solution in DMSO. The mixture solution was then poured into the polydimethylsiloxane mold and covered with a 3-(trimethoxysilyl)propyl methacrylate-treated glass slide, followed by ultraviolet curing for 60 s; cycling in vacuum was implemented prior to UV curing to remove any trapped air bubbles inside the mold. The cured gel structure was carefully pulled out from the mold to yield the pillar array, and then immersed into deionized water to remove the DMSO. The gel structure was soaked in a 0.33 M hydrazine aqueous solution to reduce the graphene oxide to rGO. Each fully hydrated pillar in the arrays had a diameter of 0.5 mm at room temperature.

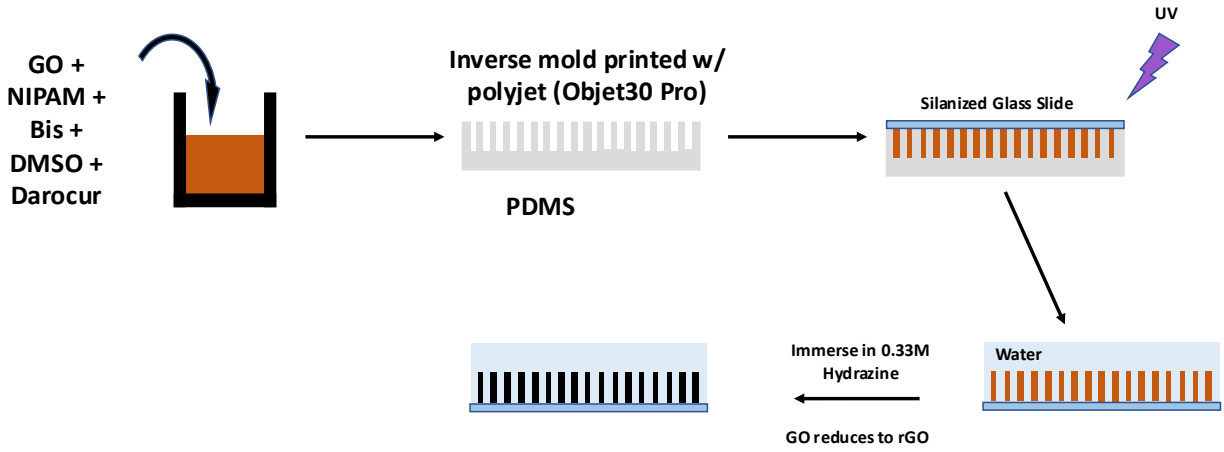

Figure 5.6 Fabrication method of phototropic pillar arrays.

5.2.3 Power Density Enhancement

Ultimately, we demonstrated the efficacy of phototropic micropillar array (each pillar with 500 µm diameter a pitch of 1 mm) in solving practical OEL problems) in solar energy harvesting. The phototropic micropillar array incorporates rGO as a broadband photoabsorber and can successfully track white-light incidence from the entire hemispheric space. Owing to the phototropism, the tips of the micropillar arrays always received the maximum photonic power density (Figure 5.7) and thus compensated for the OEL. Comparing with a non-tropistic textured surface as the control sample, we evaluated the benefits of the tropistic oblique-loss compensation (OLC) enabled by the micropillar array (Figure 5.8).

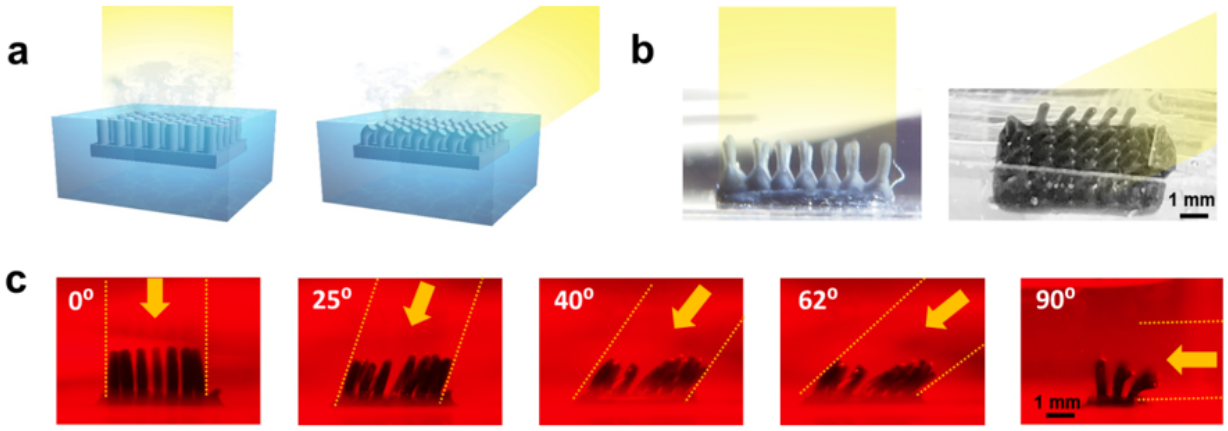

Figure 5.7 Schematic (a) and photos (b) of OLC in SVG, with a phototropic micropillar array that maximizes the incoming white-light power density. (c) Side-view photos of the micropillar array tracking various angles of incident light (0–90°).

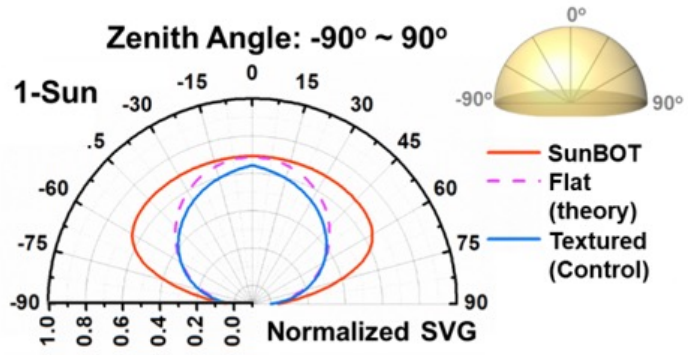

Figure 5.8 The measured normalized solar apor generation of the phototropic micropillar arrays under 1 Sun illumination at various zenith angles from −90 to 90°, in comparison to control samples of a flat surface (in theory) and a non-tropistic textured surface.

5.2.4 Broad Multi-Temperature Application

With this photothermal absorber concentration, we fabricated single pillars to demonstrate white light tracking at wide temperature ranges (Figure 5.9). By incorporating acrylamide monomer (more hydrophilic than NIPAM) into the prepolymer blend, we can increase the LCST of the hydrogel such that it can operate at temperatures above 32°C.

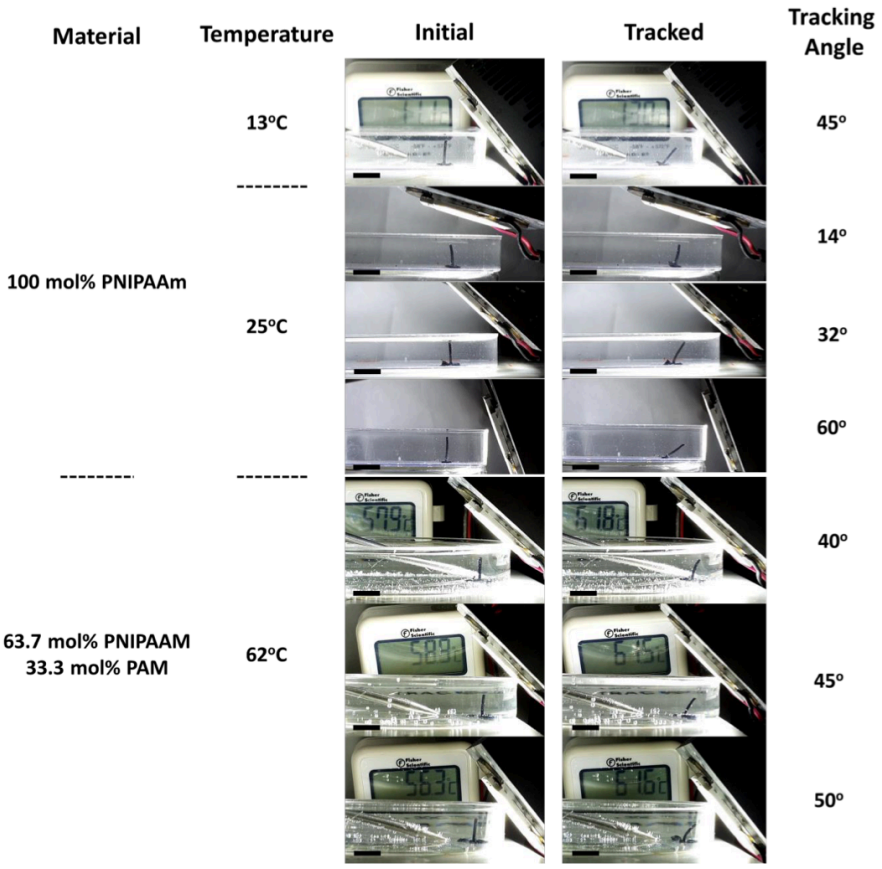

Figure 5.9 The successful tracking of light (white LED) incident from a series of arbitrary incident angles (as labelled) at a broad range of bath temperatures spanning from 13 °C to 62 °C. The hydrogel used for tracking at T>32 °C is PPy-coated PAM-co-PNIPAM, where polypyrrole serves

as the photo-absorber and acrylamide (AM) increases the LCST of PNIPAM as a hydrophilic co-monomer.

5.2.5 Solar Vapor Generation

For phototropism-enhanced solar vapor generation (SVG), we demonstrated an array of PNIPAM-rGO pillars which can all autonomously self-orient towards sunlight and therefore enhance the surface's ability to overcome water's enthalpy of evaporation. In covering the surface with a pillar array, the spacing between the pillars must not be too large to counteract the phototropism benefit. A simple calculation can demonstrate what fill factor is necessary to outperform a flat surface at each angle (Figure 5.10). Based on this calculation, we aim for a filling ratio of 80%. This phototropic pillar array was able to outperform a textured control sample at high (60°) oblique incidence angles in terms of SVG, despite exhibiting the same footprint area (Figure 5.11).

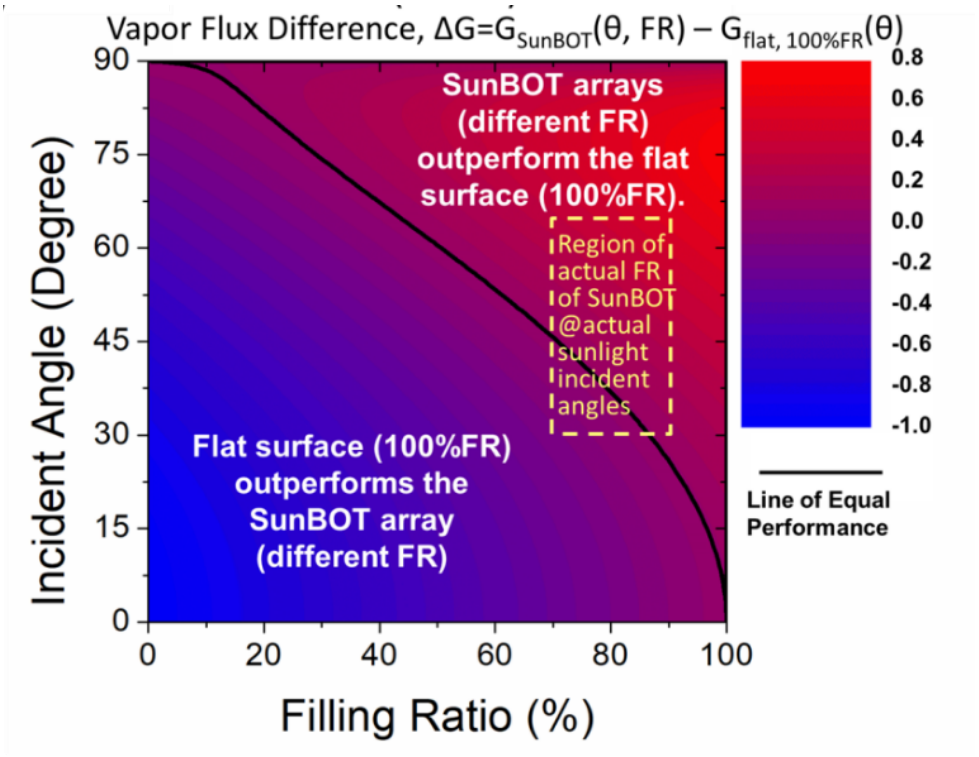

Figure 5.10 Vapor flux difference between phototropic surface and flat surface. Red region indicates when a phototropic surface outperforms a flat surface.

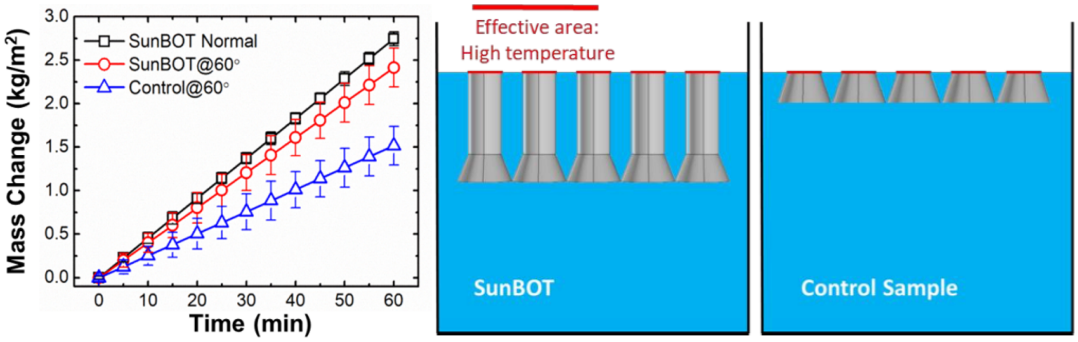

Figure 5.11 Time-dependent SVG mass change per unit area. The phototropic pillar array under a 60° (zenith) illumination is comparable to that under normal incidence, whereas the control

sample exhibits a 45% reduction in SVG. Plots are centered on the mean and the bars indicate the standard deviation.

To demonstrate the potential application of the phototropic pillar arrays in practical water purification, we conducted the outdoor experiment (Figure 5.12). Typically, the sample was floating on the water in a petri dish as shown in Figure 5.12c. The petri dish was placed in a desiccator as the water collecting container in a close system. The evaporated water was condensed on a transparent lid of desiccator and flowed down to the bottom. The experiment was conducted from 6:00 (sunrise time) to 20:00 (sunset time) under natural sunlight with the temperature of 17-23 °C, located in Los Angeles, the United States. We prepared four petri dishes, each of which contained, respectively, the phototropic pillar array, a textured non-tropistic control sample, a flat non-tropistic control sample, and a blank water-only control sample (for measuring the background water loss). All the three samples were made of the same hydrogel with a foorprint of 10 cm x10 cm. The mass of the petri dish with water was weighed before and after the testing. Based on the day-long tests, the measured average evaporation rate of phototropic pillar array sample was 0.98 kg h m^{-2}, whereas that of non-tropistic textured surface, non-tropistic flat surface, and pure water were 0.67, 0.65, and 0.18 kg h m^{-2}, respectively (Figure 5.13).

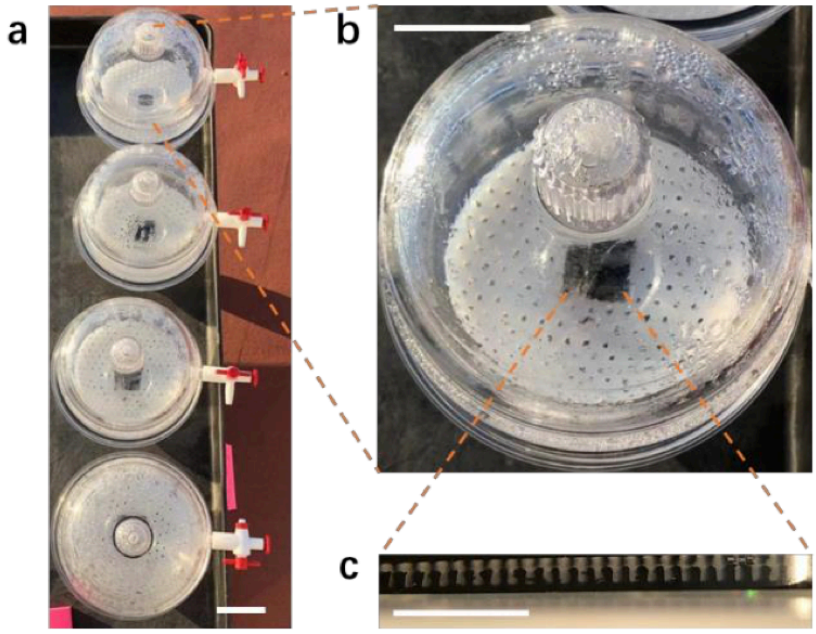

Figure 5.12 Daily solar vapor generation under outdoor sunlight. (a,b) photograghs of water collection systems. c) side-view photograph of phototropic pillar array sample floating on water surface.

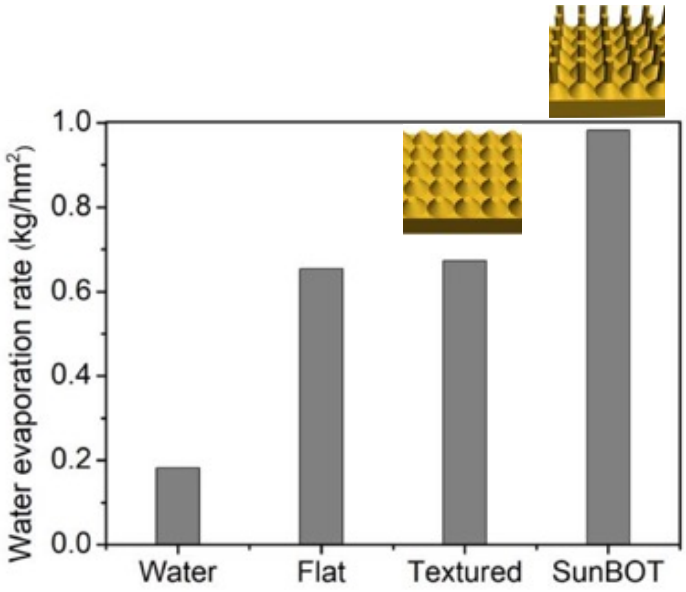

Figure 5.13 Water evaporation rate of pure water, flat surface (control sample I), textured surface (control sample II), and photootropic pillar array (phototropic sample).

Chapter 6: Conclusion and Future Outlook

In summary, we have developed two material platforms which endowed upon porous polymer systems unprecedented properties: cononsolvency-modulated pore structure control and artificial phototropism. Specifically, we developed a series of systematic studies to confirm the ideal mixed solvent that promotes phase separation in PNIPAM, generated a ranked mixed solvent series analogous to the Hofmeister series for ions, and optimized the formulation to create chemistry-impartial tough gel polymer electrolytes with record-high ionic conductance. These gel polymer electrolytes were benchmarked against commercial glass fiber and polypropylene separators on a materials level and at the cell level, achieving superior cell capacities at 6C charging and discharging rates. In addition, we used these polymer structures to design highly-responsive soft

robot actuators with complex spatiotemporal motions. Towards enabling artificial phototropism, we drew inspiration from nature to imitate the plant stem self-orientation towards sunlight. This was achieved via a symmetric cylindrical design of temperature-responsive polymer embedded with photo-absorbers, creating a built-in feedback loop that maintains an equilibrium state while tracking an incoming light source. By fabricating a surface of these light-tracking pillars, we were able to achieve an enhancement of harvesting sunlight at oblique incident angles, which we leveraged to increase the rate of solar steam generation. We are optimistic that these material platforms will yield additional demonstrations in the future and that the foundation that has been laid will decrease the barrier for tackling some of the most pressing contemporary energy and water issues plaguing our society (Figure 6.1).

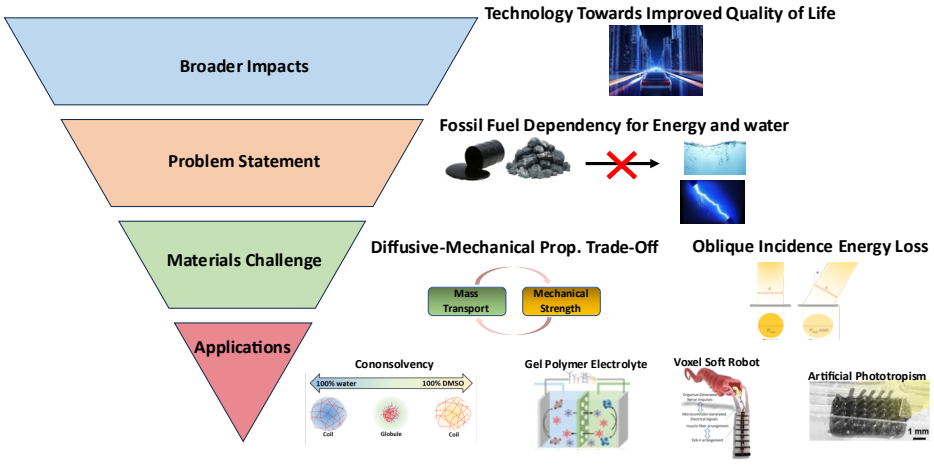

Figure 6.1 The materials challenges and their corresponding research projects within the context of larger high-value problem statements and broader impacts.

References

1. Mekonnen, M. M. & Hoekstra, A. Y. Sustainability: Four billion people facing severe water scarcity. *Sci Adv* **2,** (2016).

2. Darrow, K., Tidball, R., Wang, J. & Hampson, A. in *US Environmental Protection Agency Combined Heat and Power Partnership* (2015).

3. Davenport, D. M., Deshmukh, A., Werber, J. R. & Elimelech, M. High-Pressure Reverse Osmosis for Energy-Efficient Hypersaline Brine Desalination: Current Status, Design Considerations, and Research Needs. *Environ Sci Technol Lett* **5,** 467–475 (2018).

4. Rozyyev, V., Thirion, D., Ullah, R., Lee, J., Jung, M., Oh, H., Atilhan, M. & Yavuz, C. T. High-capacity methane storage in flexible alkane-linked porous aromatic network polymers. *Nat Energy* **4,** 604–611 (2019).

5. Cao, C.-X., Yuan, J., Cheng, J.-P. & Han, B.-H. Synthesis of porous polymer/tissue paper hybrid membranes for switchable oil/water separation. *Sci Rep* **7,** 3101 (2017).

6. Li, J. & Mooney, D. J. Designing hydrogels for controlled drug delivery. *Nat Rev Mater* **1,** (2016).

7. Sun, Q., Dai, Z., Meng, X. & Xiao, F.-S. Porous polymer catalysts with hierarchical structures. *Chem. Soc. Rev* **44,** 6018 (2015).

8. Liu, X., Xu, Y. & Jiang, D. Conjugated microporous polymers as molecular sensing devices: Microporous architecture enables rapid response and enhances sensitivity in fluorescence-on and fluorescence-off sensing. *J Am Chem Soc* **134,** 8738–8741 (2012).

9. Xu, F., Wu, D., Fu, R. & Wei, B. Design and preparation of porous carbons from conjugated polymer precursors. *Materials Today* **20,** 629–656 (2017).

10. Liu, X. & Ma, P. X. Polymeric Scaffolds for Bone Tissue Engineering. *Ann Biomed Eng* **32,** 477–486 (2004).

11. Stephan, A. M. Review on gel polymer electrolytes for lithium batteries. *Eur Polym J* **42,** 21–42 (2006).

12. Yuan, D., Lu, W., Zhao, D. & Zhou, H. C. Highly Stable Porous Polymer Networks with Exceptionally High Gas-Uptake Capacities. *Advanced Materials* **23,** 3723–3725 (2011).

13. Wu, D., Xu, F., Sun, B., Fu, R., He, H. & Matyjaszewski, K. Design and Preparation of Porous Polymers. *Chem Rev* **112,** 3959–4015 (2012).

14. Koponen, A., Kataja, M. & Timonen, J. Tortuous flow in porous media. *Phys Rev E Stat Phys Plasmas Fluids Relat Interdiscip Topics* **54,** 406–410 (1996).

15. Agarwal, A., McAnulty, J. F., Schurr, M. J., Murphy, C. J. & Abbott, N. L. in *Advanced Wound Repair Therapies* 186–208 (Elsevier, 2011). doi:10.1533/9780857093301.2.186

16. Karimi, A. & Navidbakhsh, M. Material properties in unconfined compression of gelatin hydrogel for skin tissue engineering applications. *Biomedical Engineering / Biomedizinische Technik* **59,** (2014).

17. Ahearne, M., Yang, Y. & Liu, K.-K. in *Topics in Tissue Engineering* (2008).

18. Qiu, Y. & Park, K. Environment-sensitive hydrogels for drug delivery. *Adv Drug Deliv Rev* **53,** 321–339 (2001).

19. Liu, Z., Faraj, Y., Ju, X. J., Wang, W., Xie, R. & Chu, L. Y. Nanocomposite smart hydrogels with improved responsiveness and mechanical properties: A mini review. *J Polym Sci B Polym Phys* **56,** 1306–1313 (2018).

20. Imran, A. Bin, Seki, T. & Takeoka, Y. Recent advances in hydrogels in terms of fast stimuli responsiveness and superior mechanical performance. *Polym J* **42,** 839–851 (2010).

21. Tanaka, T. & Fillmore, D. J. Kinetics of swelling of gels. *J Chem Phys* **70,** 1214–1218 (1979).

22. Bodenberger, N., Kubiczek, D., Abrosimova, I., Scharm, A., Kipper, F., Walther, P. & Rosenau, F. Evaluation of methods for pore generation and their influence on physio-chemical properties of a protein based hydrogel. *Biotechnology Reports* **12,** 6–12 (2016).

23. Thein-Han, W. W. & Misra, R. D. K. Biomimetic chitosan-nanohydroxyapatite composite scaffolds for bone tissue engineering. *Acta Biomater* **5,** 1182–1197 (2009).

24. Serizawa, T., Wakita, K. & Akashi, M. Rapid Deswelling of Porous Poly. *Macromolecules* **35,** 10–12 (2002).

25. Xue, S., Wu, Y., Wang, J., Guo, M., Liu, D. & Lei, W. Boron nitride nanosheets/PNIPAM hydrogels with improved thermo-responsive performance. *Materials* **11,** 1–9 (2018).

26. Lee, E., Kim, D., Kim, H. & Yoon, J. Photothermally driven fast responding photo-actuators fabricated with comb-type hydrogels and magnetite nanoparticles. *Sci Rep* **5,** 1–8 (2015).

27. Gancheva, T. & Virgilio, N. Enhancing and Tuning the Response of Environmentally Sensitive Hydrogels with Embedded and Interconnected Pore Networks. *Macromolecules* **49,** 5866–5876 (2016).

28. Chirila, T. V, Constable, I. J., Crawford, G. J., Vijayasekaran, S., Thompson, D. E., Chen, Y., Fletcher, W. A. & Griffin, B. J. Sponges As Implant Materials :/ N Vivo and / N V / Tro Evaluation of Cellular Invasion. 26–38 (1993).

29. Chang, S., Kim, M., Oh, S., Min, J. H., Kang, D., Han, C., Ahn, T., Koh, W. G. & Lee, H. Multi-scale characterization of surface-crosslinked superabsorbent polymer hydrogel spheres. *Polymer (Guildf)* **145,** 174–183 (2018).

30. Ji, C., Khademhosseini, A. & Dehghani, F. Enhancing cell penetration and proliferation in chitosan hydrogels for tissue engineering applications. *Biomaterials* **32,** 9719–9729 (2011).

31. Gemeinhart, R. A., Park, H. & Park, K. Pore structure of superporous hydrogels. *Polym Adv Technol* **11,** 617–625 (2000).

32. Anseth, K. S., Bowman, C. N. & Brannon-Peppas, L. Mechanical properties of hydrogels and their experimental determination. *Biomaterials* **17,** 1647–1657 (1996).

33. Ebner, M., Chung, D. W., García, R. E. & Wood, V. Tortuosity anisotropy in lithium-ion battery electrodes. *Adv Energy Mater* **4,** 1–6 (2014).

34. Forney, B. S., Baguenard, C. & Allan Guymon, C. Improved stimuli-response and mechanical properties of nanostructured poly(N-isopropylacrylamide-co-dimethylsiloxane) hydrogels generated through photopolymerization in lyotropic liquid crystal templates. *Soft Matter* **9,** 7458–7467 (2013).

35. Deville, S. *Ice-Templating: Processing Routes, Architectures, and Microstructures*. (2017). doi:10.1007/978-3-319-50515-2_4

36. Sornkamnerd, S., Okajima, M. K. & Kaneko, T. Tough and Porous Hydrogels Prepared by Simple Lyophilization of LC Gels. *ACS Omega* **2,** 5304–5314 (2017).

37. Zhang, Z., He, L., Zhu, C., Qian, Y., Wen, L. & Jiang, L. Improved osmotic energy conversion in heterogeneous membrane boosted by three-dimensional hydrogel interface. *Nat Commun* **11,** (2020).

38. Gemeinhart, R. A. & Guo, C. *Reflexive Polymers and Hydrogels*. (CRC Press, 2004). doi:10.1201/9780203485354

39. Lanasa, S. M., Hoffecker, I. T. & Bryant, S. J. Presence of pores and hydrogel composition influence tensile properties of scaffolds fabricated from well-defined sphere templates. *J Biomed Mater Res B Appl Biomater* **96B,** 294–302 (2011).

40. Kováčik, J. Correlation between Young's modulus and porosity in porous materials. *J Mater Sci Lett* **18,** 1007–1010 (1999).

41. Sun, J.-Y., Zhao, X., Illeperuma, W. R. K., Chaudhuri, O., Oh, K. H., Mooney, D. J., Vlassak, J. J. & Suo, Z. Highly stretchable and tough hydrogels. *Nature* **489,** 133–136 (2012).

42. Yuk, H., Zhang, T., Parada, G. A., Liu, X. & Zhao, X. Skin-inspired hydrogel–elastomer hybrids with robust interfaces and functional microstructures. *Nat Commun* **7,** 12028 (2016).

43. Zhao, F., Zhou, X., Shi, Y., Qian, X., Alexander, M., Zhao, X., Mendez, S., Yang, R., Qu, L. & Yu, G. Highly efficient solar vapour generation via hierarchically nanostructured gels. *Nat Nanotechnol* **13,** 489–495 (2018).

44. Wu, S., Alsaid, Y., Yao, B., Yan, Y., Zhao, Y., Hua, M., Wu, D., Zhu, X. & He, X. Rapid and scalable fabrication of ultra-stretchable, anti-freezing conductive gels by cononsolvency effect. *EcoMat* **3,** e12085 (2021).

45. Alsaid, Y., Wu, S., Wu, D., Du, Y., Shi, L., Khodambashi, R., Rico, R., Hua, M., Yan, Y., Zhao, Y., Aukes, D. & He, X. Tunable Sponge-Like Hierarchically Porous Hydrogels with Simultaneously Enhanced Diffusivity and Mechanical Properties. *Advanced Materials* **33,** 2008235 (2021).

46. Liu, Y., Zhang, J., Yan, Y., Yang, C., Pan, J., Zhang, X. & Wei, Z. Mixed Solvent as a Critical Factor in Optimizing Phase Separation of All Small Molecule Organic Solar Cells. *ACS Appl Energy Mater* **4,** 11769–11776 (2021).

47. Kozin, V. G. & Mukhamadiev, A. A. Extraction of Aromatic Hydrocarbons with a Mixed Solvent. Phase Equilibria and a Mathematical Description of the Process. *Chemistry and Technology of Fuels and Oils* **38,** 100–106 (2002).

48. Jandera, P. LIQUID CHROMATOGRAPHY | Normal Phase. *Encyclopedia of Analytical Science: Second Edition* 142–152 (2005). doi:10.1016/B0-12-369397-7/00324-1

49. Pirrung, M. C. Purification of Products. *Handbook of Synthetic Organic Chemistry* 151–164 (2017). doi:10.1016/B978-0-12-809504-1.00014-5

50. Jouyban, A. Review of the cosolvency models for predicting solubility of drugs in water-cosolvent mixtures. *Journal of Pharmacy & Pharmaceutical Sciences* **11,** 32 (2008).

51. van Franeker, J. J., Turbiez, M., Li, W., Wienk, M. M. & Janssen, R. A. J. A real-time study of the benefits of co-solvents in polymer solar cell processing. *Nat Commun* **6,** 6229 (2015).

52. Mardles, E. W. J. Study of the solvents of some cellulose esters. *Journal of the Society of Chemical Industry* **42,** 127T-136T (1923).

53. Winnik, F. M., Ringsdorf, H. & Venzmer, J. Methanol-Water as a Co-Nonsolvent System for Poly(N-Isopropylacrylamide). *Macromolecules* **23,** 2415–2416 (1990).

54. Schild, H. G., Muthukumar, M. & Tirrell, D. A. Cononsolvency in Mixed Aqueous Solutions of Poly(N- isopropylacrylamide). *Macromolecules* **24,** 948–952 (1991).

55. Mukae, K., Sakurai, M., Sawamura, S., Makino, K., Kim, S. W., Ueda, I. & Shirahama, K. Swelling of poly(N-isopropylacrylamide) gels in water-alcohol (C1-C4) mixed solvents. *Journal of Physical Chemistry* **97,** 737–741 (1993).

56. Kojima, H. & Tanaka, F. Cooperative hydration induces discontinuous volume phase transition of cross-linked poly(N -isopropylacrylamide) gels in water. *Macromolecules* **43,** 5103–5113 (2010).

57. Tanaka, F., Koga, T., Kojima, H., Xue, N. & Winnik, F. M. Preferential adsorption and Co-nonsolvency of thermoresponsive polymers in mixed solvents of water/methanol. *Macromolecules* **44,** 2978–2989 (2011).

58. Pica, A. & Graziano, G. An alternative explanation of the cononsolvency of poly(N-isopropylacrylamide) in water-methanol solutions. *Physical Chemistry Chemical Physics* **18,** 25601–25608 (2016).

59. Hao, J., Cheng, H., Butler, P., Zhang, L. & Han, C. C. Origin of cononsolvency, based on the structure of tetrahydrofuran-water mixture. *Journal of Chemical Physics* **132,** (2010).

60. Mukherji, D., Marques, C. M. & Kremer, K. Polymer collapse in miscible good solvents is a generic phenomenon driven by preferential adsorption. *Nat Commun* **5,** 1–6 (2014).

61. Magda, J. J., Fredrickson, G. H., Larson, R. G. & Helfand, E. Dimensions of a Polymer Chain in a Mixed Solvent. *J. Phys. Rev. B: Condens. Matter* **21,** 4640 (1988).

62. Bharadwaj, S. & Van Der Vegt, N. F. A. Does Preferential Adsorption Drive Cononsolvency? *Macromolecules* **52,** 4131–4138 (2019).

63. Kojima, H., Tanaka, F., Scherzinger, C. & Richtering, W. Temperature dependent phase behavior of PNIPAM microgels in mixed water/methanol solvents. *J Polym Sci B Polym Phys* **51,** 1100–1111 (2013).

64. Yamauchi, H. & Maeda, Y. LCST and UCST behavior of poly(N-isopropylacrylamide) in DMSO/water mixed solvents studied by IR and micro-raman spectroscopy. *Journal of Physical Chemistry B* **111,** 12964–12968 (2007).

65. Zhang, X., Zong, J. & Meng, D. A unified understanding of the cononsolvency of polymers in binary solvent mixtures. *Soft Matter* **16,** 7789–7796 (2020).

66. Yamauchi, H. & Maeda, Y. LCST and UCST behavior of poly(N-isopropylacrylamide) in DMSO/water mixed solvents studied by IR and micro-raman spectroscopy. *Journal of Physical Chemistry B* **111,** 12964–12968 (2007).

67. Costa, R. O. R. & Freitas, R. F. S. Phase behavior of poly (N-isopropylacrylamide) in binary aqueous solutions. *Polymer (Guildf)* **43,** 5879–5885 (2002).

68. Maccarrone, S., Scherzinger, C., Holderer, O., Lindner, P., Sharp, M., Richtering, W. & Richter, D. Cononsolvency effects on the structure and dynamics of microgels. *Macromolecules* **47,** 5982–5988 (2014).

69. Amiya, T., Hirokawa, Y., Hirose, Y., Li, Y. & Tanaka, T. Reentrant phase transition of N - isopropylacrylamide gels in mixed solvents. *J Chem Phys* **86,** 2375–2379 (1987).

70. Tokuyama, H., Ishihara, N. & Sakohara, S. Porous poly(N-isopropylacrylamide) gels polymerized in mixed solvents of water and N,N-dimethylformamide. *Polymer Bulletin* **61,** 399–405 (2008).

71. Wang, Q., Biswas, C. S., Galluzzi, M., Wu, Y., Du, B. & Stadler, F. J. Random copolymer gels of N-isopropylacrylamide and N-ethylacrylamide: effect of synthesis solvent compositions on their properties. *RSC Adv* **7,** 9381–9392 (2017).

72. Xu, Y., Li, Y., Cao, X., Chen, Q. & An, Z. Versatile RAFT dispersion polymerization in cononsolvents for the synthesis of thermoresponsive nanogels with controlled composition, functionality and architecture. *Polym Chem* **5,** 6244–6255 (2014).

73. Mukherji, D., Watson, M. D., Morsbach, S., Schmutz, M., Wagner, M., Marques, C. M. & Kremer, K. Soft and Smart: Co-nonsolvency-Based Design of Multiresponsive Copolymers. *Macromolecules* **52,** 3471–3478 (2019).

74. Mukherji, D., Marques, C. M. & Kremer, K. Smart Responsive Polymers: Fundamentals and Design Principles. *Annu. Rev. Condens. Matter Phys. 2020* **11,** 271–299 (2020).

75. Wicky, B. I. M., Shammas, S. L. & Clarke, J. Affinity of IDPs to their targets is modulated by ion-specific changes in kinetics and residual structure. *Proceedings of the National Academy of Sciences* **114,** 9882–9887 (2017).

76. Hua, M., Wu, S., Ma, Y., Zhao, Y., Chen, Z., Frenkel, I., Strzalka, J., Zhou, H., Zhu, X. & He, X. Strong tough hydrogels via the synergy of freeze-casting and salting-out. *Nature* **in press,** (2021).

77. Yan, Y., Duan, S., Liu, B., Wu, S., Alsaid, Y., Yao, B., Nandi, S., Du, Y., Wang, T. W., Li, Y. & He, X. Tough Hydrogel Electrolytes for Anti-Freezing Zinc-Ion Batteries. *Advanced Materials* **35,** 2211673 (2023).

78. Nakanishi, K. Macroporous Morphology Control by Phase Separation. *Handbook of Sol-Gel Science and Technology* 1–32 (2016). doi:10.1007/978-3-319-19454-7_25-1

79. Yamauchi, H. & Maeda, Y. LCST and UCST behavior of poly(N-isopropylacrylamide) in DMSO/water mixed solvents studied by IR and micro-raman spectroscopy. *Journal of Physical Chemistry B* **111,** 12964–12968 (2007).

80. Kyriakos, K., Philipp, M., Adelsberger, J., Jaksch, S., Berezkin, A. V., Lugo, D. M., Richtering, W., Grillo, I., Miasnikova, A., Laschewsky, A., Müller-Buschbaum, P. & Papadakis, C. M. Cononsolvency of Water/Methanol Mixtures for PNIPAM and PS- b -PNIPAM: Pathway of Aggregate Formation Investigated Using Time-Resolved SANS. *Macromolecules* **47,** 6867–6879 (2014).

81. Schild, H. G., Muthukumar, M. & Tirrell, D. A. Cononsolvency in Mixed Aqueous Solutions of Poly(N- isopropylacrylamide). *Macromolecules* **24,** 948–952 (1991).

82. Bischofberger, I., Calzolari, D. C. E., De Los Rios, P., Jelezarov, I. & Trappe, V. Hydrophobic hydration of poly-N-isopropyl acrylamide: a matter of the mean energetic state of water. *Scientific Reports* **4,** 4377 (2015).

83. Zhang, X. Z., Yang, Y. Y. & Chung, T. S. Effect of mixed solvents on characteristics of poly(N-isopropylacrylamide) gels. *Langmuir* **18,** 2538–2542 (2002).

84. Kabra, B. G. & Gehrke, S. H. Synthesis of fast response, temperature-sensitive poly(N-isopropylacrylamide) gel. *Polymer communications Guildford* **32,** 322–323 (1991).

85. Cheng, S. X., Zhang, J. T. & Zhuo, R. X. Macroporous poly(N-isopropylacrylamide) hydrogels with fast response rates and improved protein release properties. *Journal of Biomedical Materials Research - Part A* **67,** 96–103 (2003).

86. Zhang, X. Z. & Zhuo, R. X. Preparation of fast responsive, temperature-sensitive poly(N-isopropylacrylamide) hydrogel. *Macromolecular Chemistry and Physics* **200,** 2602–2605 (1999).

87. Xue, W., Hamley, I. W. & Huglin, M. B. Rapid swelling and deswelling of thermoreversible hydrophobically modified poly(N-isopropylacrylamide) hydrogels prepared by freezing polymerisation. *Polymer* **43,** 5181–5186 (2002).

88. Kaneko, Y., Sakai, K., Kikuchi, A., Yoshida, R., Sakurai, Y. & Okano, T. Influence of Freely Mobile Grafted Chain Length on Dynamic Properties of Comb-Type Grafted Poly(N-isopropylacrylamide) Hydrogels. *Macromolecules* **28,** 7717–7723 (1995).

89. Noguchi, Y., Okeyoshi, K. & Yoshida, R. Design of surfactant-grafted hydrogels with fast response to temperature. *Macromolecular Rapid Communications* **26,** 1913–1917 (2005).

90. Gil, E. S. & Hudson, S. M. Effect of silk fibroin interpenetrating networks on swelling/deswelling kinetics and rheological properties of poly(N-isopropylacrylamide) hydrogels. *Biomacromolecules* **8,** 258–264 (2007).

91. Mou, C., Ju, X., Zhang, L., Xie, R., Wang, W., Deng, N., Wei, J., Chen, Q. & Chu, L. Monodisperse and Fast-Responsive Poly(N - isopropylacrylamide) Microgels with Open-Celled Porous Structure. (2014). doi:10.1021/la4046379

92. Xia, L. W., Xie, R., Ju, X. J., Wang, W., Chen, Q. & Chu, L. Y. Nano-structured smart hydrogels with rapid response and high elasticity. *Nature Communications* **4,** 1–11 (2013).

93. Ma, X. M., Li, R., Ren, J., Lv, X. C., Zhao, X. H., Ji, Q. & Xia, Y. Z. Restorable, high-strength poly(: N -isopropylacrylamide) hydrogels constructed through chitosan-based dual macro-cross-linkers with rapid response to temperature jumps. *RSC Advances* **7,** 47767–47774 (2017).

94. Li, P., Hou, X., Qu, L., Dai, X. & Zhang, C. PNIPAM-MAPOSS hybrid hydrogels with excellent swelling behavior and enhanced mechanical performance: Preparation and drug release of 5-fluorouracil. *Polymers* **10,** (2018).

95. Zheng, W. J., An, N., Yang, J. H., Zhou, J. & Chen, Y. M. Tough Al-alginate/Poly(N -isopropylacrylamide) hydrogel with tunable LCST for soft robotics. *ACS Applied Materials and Interfaces* **7,** 1758–1764 (2015).

96. Liu, C., Yu, J., Jiang, G., Liu, X., Li, Z., Gao, G. & Liu, F. Thermosensitive poly (N-isopropylacrylamide) hydrophobic associated hydrogels: Optical, swelling/deswelling, and mechanical properties. *Journal of Materials Science* **48,** 774–784 (2013).

97. Flory, P. J. & Rehner, J. Statistical Mechanics of Cross-Linked Polymer Networks II. Swelling. *J Chem Phys* **11,** 521–526 (1943).

98. Nakamoto, C., Kitada, T. & Kato, E. Pressure dependence on the Flory-Huggins interaction parameter of poly(N-isopropylacrylamide) gels. *Polymer Gels and Networks* **4,** 17–31 (1996).

99. Alger, M. S. M. *Polymer Science Dictionary*. (Chapman & Hall, 1997).

100. Amici, J., Asinari, P., Ayerbe, E., Barboux, P., Bayle-Guillemaud, P., Behm, R. J., Berecibar, M., Berg, E., Bhowmik, A., Bodoardo, S., Castelli, I. E., Cekic-Laskovic, I., Christensen, R., Clark, S., Diehm, R., Dominko, R., Fichtner, M., Franco, A. A., Grimaud, A., Guillet, N., Hahlin, M., Hartmann, S., Heiries, V., Hermansson, K., Heuer, A., Jana, S., Jabbour, L., Kallo, J., Latz, A., Lorrmann, H., Løvvik, O. M., Lyonnard, S., Meeus, M., Paillard, E., Perraud, S., Placke, T., Punckt, C., Raccurt, O., Ruhland, J., Sheridan, E., Stein, H., Tarascon, J. M., Trapp, V., Vegge, T., Weil, M., Wenzel, W., Winter, M., Wolf, A. & Edström, K. A Roadmap for Transforming Research to Invent the Batteries of the Future Designed within the European Large Scale Research Initiative BATTERY 2030+. *Adv Energy Mater* **12,** 2102785 (2022).

101. Tian, P., Zhong, X., Gu, C., Wang, Z. & Shi, F. SiO2-Alginate-Based Gel Polymer Electrolytes for Zinc-Ion Batteries. *Batteries* **8,** 175 (2022).

102. Yi, Q., Zhang, W., Li, S., Li, X. & Sun, C. Durable Sodium Battery with a Flexible Na 3 Zr 2 Si 2 PO 12 -PVDF-HFP Composite Electrolyte and Sodium/Carbon Cloth Anode. *ACS Appl Mater Interfaces* **10,** 35039–35046 (2018).

103. Gabryelczyk, A., Swiderska-Mocek, A. & Czarnecka-Komorowska, D. Muscovite as an inert filler for highly conductive and durable gel polymer electrolyte in sodium-ion batteries. *J Power Sources* **552,** 232259 (2022).

104. Shin, W. K., Cho, J., Kannan, A. G., Lee, Y. S. & Kim, D. W. Cross-linked Composite Gel Polymer Electrolyte using Mesoporous Methacrylate-Functionalized SiO2 Nanoparticles for Lithium-Ion Polymer Batteries. *Scientific Reports 2016 6:1* **6,** 1–10 (2016).

105. Zhu, M., Lan, J., Tan, C., Sui, G. & Yang, X. Degradable cellulose acetate/poly-L-lactic acid/halloysite nanotube composite nanofiber membranes with outstanding performance for gel polymer electrolytes. *J Mater Chem A Mater* **4,** 12136–12143 (2016).

106. Pan, X., Hou, Q., Liu, L., Zhang, J., An, M. & Yang, P. Semiconductor TiO2 ceramic filler for safety-improved composite ionic liquid gel polymer electrolytes. *Ionics (Kiel)* **27,** 2045–2051 (2021).

107. Lehmann, M. L., Yang, G., Gilmer, D., Han, K. S., Self, E. C., Ruther, R. E., Ge, S., Li, B., Murugesan, V., Sokolov, A. P., Delnick, F. M., Nanda, J. & Saito, T. Tailored crosslinking of Poly(ethylene oxide) enables mechanical robustness and improved sodium-ion conductivity. *Energy Storage Mater* **21,** 85–96 (2019).

108. Liu, Z., Wang, D., Tang, Z., Liang, G., Yang, Q., Li, H., Ma, L., Mo, F. & Zhi, C. A mechanically durable and device-level tough Zn-MnO2 battery with high flexibility. *Energy Storage Mater* **23,** 636–645 (2019).

109. Sun, P., Liu, W., Yang, D., Zhang, Y., Xiong, W., Li, S., Chen, J., Tian, J. & Zhang, L. Stable Zn anodes enabled by high-modulus agarose gel electrolyte with confined water molecule mobility. *Electrochim Acta* **429,** 140985 (2022).

110. Mo, F., Liang, G., Meng, Q., Liu, Z., Li, H., Fan, J. & Zhi, C. A flexible rechargeable aqueous zinc manganese-dioxide battery working at −20 °C. *Energy Environ Sci* **12,** 706–715 (2019).

111. Huang, Y., Zhang, J., Liu, J., Li, Z., Jin, S., Li, Z., Zhang, S. & Zhou, H. Flexible and stable quasi-solid-state zinc ion battery with conductive guar gum electrolyte. *Mater Today Energy* **14,** 100349 (2019).

112. Han, Q., Chi, X., Zhang, S., Liu, Y., Zhou, B., Yang, J. & Liu, Y. Durable, flexible self-standing hydrogel electrolytes enabling high-safety rechargeable solid-state zinc metal batteries. *J Mater Chem A Mater* **6,** 23046–23054 (2018).

113. Yu, F., Zhang, H., Zhao, L., Sun, Z., Li, Y., Mo, Y. & Chen, Y. A flexible Cellulose/Methylcellulose gel polymer electrolyte endowing superior Li+ conducting property for lithium ion battery. *Carbohydr Polym* **246,** 116622 (2020).

114. Li, C., Ou, L., Liu, Y., Xu, L., Zhou, S., Guo, L., Liu, H., Zhang, Z., Cui, M., Chen, G., Huang, J. & Tao, J. A Cellulose/Polyethylene Oxide Gel Polymer Electrolyte with Enhanced Mechanical Strength and High Ionic Conductivity for Lithium-Ion Batteries. *Adv Mater Technol* **8,** 2202002 (2023).

115. Song, A., Huang, Y., Liu, B., Cao, H., Zhong, X., Lin, Y., Wang, M., Li, X. & Zhong, W. Gel polymer electrolyte based on polyethylene glycol composite lignocellulose matrix with higher comprehensive performances. *Electrochim Acta* **247,** 505–515 (2017).

116. Li, Z., Liu, Y., Liang, X., Yu, M., Liu, B., Sun, Z., Hu, W. & Zhu, G. A single-ion gel polymer electrolyte based on polyimide grafted with lithium 3-chloropropanesulfonyl (trifluoromethanesulfonyl) imide for high performance lithium ion batteries. *J Mater Chem A Mater* **11,** 1766–1773 (2023).

117. Tan, L., Deng, Y., Cao, Q., Jing, B., Wang, X. & Liu, Y. Gel electrolytes based on polyacrylonitrile/thermoplastic polyurethane/polystyrene for lithium-ion batteries. *Ionics (Kiel)* **25,** 3673–3682 (2019).

118. Mackanic, D. G., Yan, X., Zhang, Q., Matsuhisa, N., Yu, Z., Jiang, Y., Manika, T., Lopez, J., Yan, H., Liu, K., Chen, X., Cui, Y. & Bao, Z. Decoupling of mechanical properties and ionic conductivity in supramolecular lithium ion conductors. *Nature Communications 2019 10:1* **10,** 1–11 (2019).

119. Pan, Q., Li, Z., Zhang, W., Zeng, D., Sun, Y. & Cheng, H. Single ion conducting sodium ion batteries enabled by a sodium ion exchanged poly(bis(4-carbonyl benzene sulfonyl)imide-co-2,5-diamino benzesulfonic acid) polymer electrolyte. *Solid State Ion* **300,** 60–66 (2017).

120. Ionov, L. Hydrogel-based actuators: possibilities and limitations. *Materials Today* **17,** 494–503 (2014).

121. Erol, O., Pantula, A., Liu, W. & Gracias, D. H. Transformer Hydrogels: A Review. *Adv Mater Technol* **4,** (2019).

122. Zhou, X., Li, T., Wang, J., Chen, F., Zhou, D., Liu, Q., Li, B., Cheng, J., Zhou, X. & Zheng, B. Mechanochemical Regulated Origami with Tough Hydrogels by Ion Transfer Printing. *ACS Appl Mater Interfaces* **10,** 9077–9084 (2018).

123. Klein, Y., Efrati, E. & Sharon, E. Shaping of Elastic Sheets by Prescription of Non-Euclidean Metrics. *Science (1979)* **315,** 1116–1120 (2007).

124. Kim, J., Hanna, J. A., Byun, M., Santangelo, C. D. & Hayward, R. C. Designing Responsive Buckled Surfaces by Halftone Gel Lithography. *Science (1979)* **335,** 1201–1205 (2012).

125. Ma, C., Le, X., Tang, X., He, J., Xiao, P., Zheng, J., Xiao, H., Lu, W., Zhang, J., Huang, Y. & Chen, T. A Multiresponsive Anisotropic Hydrogel with Macroscopic 3D Complex Deformations. *Adv Funct Mater* **26,** 8670–8676 (2016).

126. Erb, R. M., Sander, J. S., Grisch, R. & Studart, A. R. Self-shaping composites with programmable bioinspired microstructures. *Nat Commun* **4,** 1712 (2013).

127. Huang, L., Jiang, R., Wu, J., Song, J., Bai, H., Li, B., Zhao, Q. & Xie, T. Ultrafast Digital Printing toward 4D Shape Changing Materials. *Advanced Materials* **29,** (2017).

128. Zheng, S. Y., Shen, Y., Zhu, F., Yin, J., Qian, J., Fu, J., Wu, Z. L. & Zheng, Q. Programmed Deformations of 3D-Printed Tough Physical Hydrogels with High Response Speed and Large Output Force. *Adv Funct Mater* **28,** (2018).

129. Wu, Z. L., Moshe, M., Greener, J., Therien-Aubin, H., Nie, Z., Sharon, E. & Kumacheva, E. Three-dimensional shape transformations of hydrogel sheets induced by small-scale modulation of internal stresses. *Nat Commun* **4,** 1586 (2013).

130. Liu, L., Jiang, S., Sun, Y. & Agarwal, S. Giving Direction to Motion and Surface with Ultra-Fast Speed Using Oriented Hydrogel Fibers. *Adv Funct Mater* **26,** 1021–1027 (2016).

131. Palagi, S., Mark, A. G., Reigh, S. Y., Melde, K., Qiu, T., Zeng, H., Parmeggiani, C., Martella, D., Sanchez-Castillo, A., Kapernaum, N., Giesselmann, F., Wiersma, D. S., Lauga, E. & Fischer, P. Structured light enables biomimetic swimming and versatile locomotion of photoresponsive soft microrobots. *Nat Mater* **15,** 647–653 (2016).

132. Mourran, A., Zhang, H., Vinokur, R. & Möller, M. Soft Microrobots Employing Nonequilibrium Actuation via Plasmonic Heating. *Advanced Materials* **29,** (2017).

133. Choi, M.-Y., Shin, Y., Lee, H. S., Kim, S. Y. & Na, J.-H. Multipolar spatial electric field modulation for freeform electroactive hydrogel actuation. *Sci Rep* **10,** 2482 (2020).

134. Frontera, W. R. & Ochala, J. Skeletal Muscle: A Brief Review of Structure and Function. *Calcif Tissue Int* **96,** 183–195 (2015).

135. Drost, M. R., Maenhout, M., Willems, P. J. B., Oomens, C. W. J., Baaijens, F. P. T. & Hesselink, M. K. C. Spatial and temporal heterogeneity of superficial muscle strain during in situ fixed-end contractions. *J Biomech* **36,** 1055–1063 (2003).

136. Buchthal, F. & Schmalbruch, H. Motor unit of mammalian muscle. *Physiol Rev* **60,** 90–142 (1980).

137. KIER, W. M. & SMITH, K. K. Tongues, tentacles and trunks: the biomechanics of movement in muscular-hydrostats. *Zool J Linn Soc* **83,** 307–324 (1985).

138. Kier, W. M. & Schachat, F. H. Biochemical Comparison of Fast- and Slow-Contracting Squid Muscle. *Journal of Experimental Biology* **168,** 41–56 (1992).

139. Liu, Z., Meyers, M. A., Zhang, Z. & Ritchie, R. O. Functional gradients and heterogeneities in biological materials: Design principles, functions, and bioinspired applications. *Prog Mater Sci* **88,** 467–498 (2017).

140. Hanassy, S., Botvinnik, A., Flash, T. & Hochner, B. Stereotypical reaching movements of the octopus involve both bend propagation and arm elongation. *Bioinspir Biomim* **10,** 035001 (2015).

141. Kazakidi, A., Tsakiris, D. P., Angelidis, D., Sotiropoulos, F. & Ekaterinaris, J. A. CFD study of aquatic thrust generation by an octopus-like arm under intense prescribed deformations. *Comput Fluids* **115,** 54–65 (2015).

142. Richter, J. N., Hochner, B. & Kuba, M. J. Octopus arm movements under constrained conditions: adaptation, modification and plasticity of motor primitives. *Journal of Experimental Biology* **218,** 1069–1076 (2015).

143. Yu, C., Duan, Z., Yuan, P., Li, Y., Su, Y., Zhang, X., Pan, Y., Dai, L. L., Nuzzo, R. G., Huang, Y., Jiang, H. & Rogers, J. A. Electronically Programmable, Reversible Shape Change in Two- and Three-Dimensional Hydrogel Structures. *Advanced Materials* **25,** 1541–1546 (2013).

144. Zhang, X.-Z., Xu, X.-D., Cheng, S.-X. & Zhuo, R.-X. Strategies to improve the response rate of thermosensitive PNIPAAm hydrogels. *Soft Matter* **4,** 385 (2008).

145. Kim, S., Lee, K. & Cha, C. Refined control of thermoresponsive swelling/deswelling and drug release properties of poly(N-isopropylacrylamide) hydrogels using hydrophilic polymer crosslinkers. *J Biomater Sci Polym Ed* **27,** 1698–1711 (2016).

146. Gan, D. & Lyon, L. A. Tunable Swelling Kinetics in Core−Shell Hydrogel Nanoparticles. *J Am Chem Soc* **123,** 7511–7517 (2001).

147. Li, P., Hou, X., Qu, L., Dai, X. & Zhang, C. PNIPAM-MAPOSS Hybrid Hydrogels with Excellent Swelling Behavior and Enhanced Mechanical Performance: Preparation and Drug Release of 5-Fluorouracil. *Polymers (Basel)* **10,** 137 (2018).

148. Depa, K., Strachota, A., Šlouf, M. & Hromádková, J. Fast temperature-responsive nanocomposite PNIPAM hydrogels with controlled pore wall thickness: Force and rate of T-response. *Eur Polym J* **48,** 1997–2007 (2012).

149. Ma, C., Li, T., Zhao, Q., Yang, X., Wu, J., Luo, Y. & Xie, T. Supramolecular Lego Assembly Towards Three-Dimensional Multi-Responsive Hydrogels. *Advanced Materials* **26,** 5665–5669 (2014).

150. Otsuka, E., Komiya, S., Sasaki, S., Xing, J., Bando, Y., Hirashima, Y., Sugiyama, M. & Suzuki, A. Effects of preparation temperature on swelling and mechanical properties of PVA cast gels. *Soft Matter* **8,** 8129 (2012).

151. Wang, Q., Biswas, C. S., Galluzzi, M., Wu, Y., Du, B. & Stadler, Florian. J. Random copolymer gels of N-isopropylacrylamide and N-ethylacrylamide: effect of synthesis solvent compositions on their properties. *RSC Adv* **7,** 9381–9392 (2017).

152. Lee, W. F. & Yen, S. H. Thermoreversible hydrogels. XII. Effect of the polymerization conditions on the swelling behavior of the N-isopropylacrylamide gel. *J Appl Polym Sci* **78,** 1604–1611 (2000).

153. Bian, Y., Du, Q., Tang, K., Shen, Y., Hao, L., Zhou, D., Wang, X., Xu, Z., Zhang, H., Zhao, L., Zhu, S., Ye, J., Lu, H., Yang, Y., Zhang, R., Zheng, Y. & Gu, S. Carbonized Bamboos as Excellent 3D Solar Vapor-Generation Devices. *Adv Mater Technol* **4,** 1–7 (2019).

154. Feng, Q., Du, L. Z., Yan, Q. Z. & Ge, C. C. Effects of synthesis-solvent on characteristics of poly(N-isopropylacrylamide) hydrogels synthesized by frontal polymerization. *Adv Mat Res* **295–297,** 1193–1197 (2011).

155. Delves, P. J. & Roitt, I. M. (Ivan M. *Encyclopedia of immunology*. (Academic Press, 1998).

156. Poppinga, S., Zollfrank, C., Prucker, O., Rühe, J., Menges, A., Cheng, T. & Speck, T. Toward a New Generation of Smart Biomimetic Actuators for Architecture. *Advanced Materials* 1703653 (2017). doi:10.1002/adma.201703653

157. Atamian, H. S., Creux, N. M., Brown, E. A., Garner, A. G., Blackman, B. K. & Harmer, S. L. Circadian regulation of sunflower heliotropism, floral orientation, and pollinator visits. *Science (1979)* **353,** 587–590 (2016).

158. Mohammad, N. & Karim, T. Design and implementation of hybrid automatic solar-tracking system. *Journal of Solar Energy Engineering, Transactions of the ASME* **135,** 1–6 (2013).

159. Wang, E., Desai, M. S. & Lee, S.-W. Light-Controlled Graphene-Elastin Composite Hydrogel Actuators. *Nano Lett* **13,** 2826–2830 (2013).

160. Ahir, S. V. & Terentjev, E. M. Photomechanical actuation in polymer–nanotube composites. *Nat Mater* **4,** 491–495 (2005).

161. Zhao, Y. L. & Fraser Stoddart, J. Azobenzene-based light-responsive hydrogel system. *Langmuir* **25,** 8442–8446 (2009).

162. Liu, X., Wei, R., Hoang, P. T., Wang, X., Liu, T. & Keller, P. Reversible and Rapid Laser Actuation of Liquid Crystalline Elastomer Micropillars with Inclusion of Gold Nanoparticles. *Adv Funct Mater* **25,** 3022–3032 (2015).

163. Camacho-Lopez, M., Finkelmann, H., Palffy-Muhoray, P. & Shelley, M. Fast liquid-crystal elastomer swims into the dark. *Nat Mater* **3,** 307–310 (2004).

164. Greffet, J.-J., Carminati, R., Joulain, K., Mulet, J.-P., Mainguy, S. & Chen, Y. Coherent emission of light by thermal sources. *Nature* **416,** 61–64 (2002).

165. Fink, Y., Winn, J. N., Fan, S., Chen, C., Michel, J., Joannopoulos, J. D. & Thomas, E. L. A Dielectric Omnidirectional Reflector. *Science (1979)* **282,** 1679–1682 (1998).

166. Teperik, T. V., García De Abajo, F. J., Borisov, A. G., Abdelsalam, M., Bartlett, P. N., Sugawara, Y. & Baumberg, J. J. Omnidirectional absorption in nanostructured metal surfaces. *Nat Photonics* **2,** 299–301 (2008).

167. Huang, J., Liu, C., Zhu, Y., Masala, S., Alarousu, E., Han, Y. & Fratalocchi, A. Harnessing structural darkness in the visible and infrared wavelengths for a new source of light. *Nat Nanotechnol* **11,** 60–66 (2015).

168. He, X., Aizenberg, M., Kuksenok, O., Zarzar, L. D., Shastri, A., Balazs, A. C. & Aizenberg, J. Synthetic homeostatic materials with chemo-mechano-chemical self-regulation. *Nature* **487,** 214–218 (2012).

169. Shastri, A., McGregor, L. M., Liu, Y., Harris, V., Nan, H., Mujica, M., Vasquez, Y., Bhattacharya, A., Ma, Y., Aizenberg, M., Kuksenok, O., Balazs, A. C., Aizenberg, J. & He, X. An aptamer-functionalized chemomechanically modulated biomolecule catch-and-release system. *Nat Chem* **7,** 447–454 (2015).

170. Qin, M., Sun, M., Bai, R., Mao, Y., Qian, X., Sikka, D., Zhao, Y., Qi, H. J., Suo, Z. & He, X. Bioinspired Hydrogel Interferometer for Adaptive Coloration and Chemical Sensing. *Advanced Materials* **30,** 1–7 (2018).

171. Sun, M., Bai, R., Yang, X., Song, J., Qin, M., Suo, Z. & He, X. Hydrogel Interferometry for Ultrasensitive and Highly Selective Chemical Detection. *Advanced Materials* **30,** 1–8 (2018).

172. Qin, M., Sun, M., Hua, M. & He, X. Bioinspired structural color sensors based on responsive soft materials. *Curr Opin Solid State Mater Sci* **23,** 13–27 (2019).

173. White, T. J. & Broer, D. J. Programmable and adaptive mechanics with liquid crystal polymer networks and elastomers. *Nat Mater* **14,** 1087–1098 (2015).

174. Gelebart, A. H., Jan Mulder, D., Varga, M., Konya, A., Vantomme, G., Meijer, E. W., Selinger, R. L. B. & Broer, D. J. Making waves in a photoactive polymer film. *Nature* **546,** 632–636 (2017).

175. Wani, O. M., Zeng, H. & Priimagi, A. A light-driven artificial flytrap. *Nat Commun* **8,** 15546 (2017).

176. Klajn, R. Spiropyran-based dynamic materials. *Chem. Soc. Rev.* **43,** 148–184 (2014).